

Aus dem Institut für Experimentelle Ophthalmologie
der Medizinische Fakultät
der Universität des Saarlandes, Homburg/Saar
Direktor: Prof. Dr. Dr. Achim Langenbacher

Prediction of ectatic corneal diseases from raw optical coherence tomography data by using convolutional neural networks

Dissertation zur Erlangung des Grades eines PhD
der Medizinischen Fakultät
der Universität des Saarlandes
2026

vorgelegt von: M.Sc. Maziar Mirsalehi
geb. am: 24. Januar 1992 in Maschhad

Tag der Promotion: 12.5.2026

Dekan: Univ.-Prof. Dr. med. dent. Matthias Hannig

Berichterstatter: Prof. Dr. Dr. Achim Langenbacher

Prof. Dr. Tobias Hartmann

Contents

1. Summary	1
2. Motivation.....	3
3. Background.....	4
3.1 Cornea	4
3.2 Artificial intelligence	4
3.3 Materials	5
3.3.1 Instrument	5
3.3.2 Data	7
3.4 Metrics and tools for interpreting results	10
3.4.1 Software	10
3.4.2 Convolutional neural network	10
3.4.2.1 DenseNets	17
3.4.2.2 EfficientNets	17
3.4.2.3 MobileNets	17
3.4.2.4 ResNets	18
3.4.3 Quality criteria	18
4. Publications	21
4.1 Article 1	21
4.2 Article 2	36
4.3 Article 3	55
5. Discussion.....	73
5.1 Limitations of the study.....	76
5.2 Conclusions and outlook	76
6. References.....	78
7. Publications.....	84
8. Abbreviations.....	85
9. Acknowledgment.....	86
10. Curriculum Vitae	87

1. Summary

Purpose

The purpose of this study is to use three-dimensional volumetric raw optical coherence tomography data to predict the ectasia screening index, a metric derived from the Casia2 anterior-segment optical coherence tomographer (Tomey, Nagoya, Japan) for detecting ectatic corneal diseases, and to classify the corneal condition through the application of convolutional neural networks.

Methods

The CNNs DenseNet121, EfficientNet-B0, and ResNet18 were modified for ESI prediction. Additionally, DenseNet121, EfficientNet-B0, MobileNetV3-Large, and ResNet18 were modified to classify the corneal condition into three categories: ‘normal’, indicating a healthy eye; ‘ectasia’, indicating corneal ectasia; and ‘other disease’, which comprised eyes with corneal dystrophies, penetrating keratoplasty, Salzmann's nodules, pterygium, subepithelial or stromal scarring. Moreover, EfficientNet-B0 was modified to mimic the ESI using a dataset of 4,898 training files, 620 validation files, and 623 test files, each containing 16 equiangular meridional images. Two-class and three-class classification models were evaluated: the two-class model distinguished no detectable ectasia from suspected ectasia or clinical ectasia, while the three-class model separated no detectable ectasia, suspected ectasia, and clinical ectasia. The performance of the CNN architectures was assessed using measures including accuracy, F1 score, positive predictive value, sensitivity, and specificity based on data from patients who were examined at the Department of Ophthalmology, Saarland University Medical Centre, Homburg, Germany.

Results

The adapted ResNet18, DenseNet121, and EfficientNet-B0 achieved accuracies of 94.80%, 95.27%, and 95.83%, respectively; F1 scores of 93.38%, 94.09%, and 94.72%, respectively; positive predictive values of 94.72%, 93.55%, and 95.28%, respectively; sensitivities of 92.07%, 94.64%, and 94.17%, respectively; and specificities of 96.61%, 95.69%, and 96.92%, respectively. For the classification of corneal condition, the modified DenseNet121, modified EfficientNet-B0, modified MobileNetV3-Large, and modified ResNet18 attained the overall accuracy of 91.27%, 91.27%, 92.86%, and 89.68%, respectively. The modified DenseNet121, modified EfficientNet-B0, modified MobileNetV3-Large, and modified ResNet18 achieved macro-averaged sensitivities of 91.27%, 91.27%, 92.86%, and 89.68%; macro-averaged specificities of 95.63%, 95.63%, 96.43%, and 94.84%; macro-averaged positive predictive values of 91.58%, 91.65%, 92.91%, and 90.24%; and macro-averaged F1 scores of 91.35%, 91.29%, 92.85%, and 89.81%, respectively. When evaluated on the 623 test files, each containing 16 equiangular meridional images, the modified EfficientNet-B0 recorded a mean absolute error of 6.65.

In the two-class classification task, the architecture attained an accuracy of 87.96%, an F1 score of 89.33%, a positive predictive value of 97.52%, a sensitivity of 82.41%, and a specificity of 96.69%. In the three-class classification task, it achieved an overall accuracy of 84.75%, a weighted-average F1 score of 84.95%, a weighted-average sensitivity of 0.8475, a weighted-average specificity of 0.9333, and a weighted-average positive predictive value of 0.8525.

Conclusion

The effective deployment of convolutional neural network architectures using raw optical coherence tomography data demonstrates the viability of raw optical coherence tomography data for diagnosing ectatic corneal diseases.

2. Motivation

Keratoconus is a condition in which the cornea of the eye becomes conical. This condition affects visual quality. Therefore, prompt treatment is essential. Understanding the condition of the cornea can help in diagnosing keratoconus and taking appropriate steps to treat it. Artificial intelligence can help ophthalmologists detect keratoconus. It is possible to use images from eye examinations as input for artificial neural networks to predict keratoconus. For this purpose, input data can be used for analysis in two forms: preprocessed or raw. Preprocessed data can undergo modifications by software and the modifications applied might remain undisclosed. Moreover, updates to the software might influence how data are handled, which can result in inconsistencies in outcomes. Raw data retain their integrity and original structure regardless of the instrument's software. Raw data usually do not change with new software tools or updates. Furthermore, the results of the analysis using raw data instead of preprocessed data are more natural, as this ensures that modifications, such as noise removal, are not applied. Therefore, using raw data instead of preprocessed data has advantages. The motivation for this study is to test raw data instead of preprocessed data for the detection of ectatic corneal diseases. Moreover, it aims to determine whether the use of raw data can outperform the performance of studies that used preprocessed data for ectatic corneal diseases detection.

3. Background

3.1 Cornea

The cornea forms the foremost section of the eye, positioned ahead of the iris and pupil. Corneal disorders often encompass vision defects like myopia, hyperopia, and astigmatism, along with conditions such as keratoconus. Keratoconus, a non-inflammatory disorder, is a condition affecting both eyes, characterised by gradual thinning and increased curvature of the cornea. It is a relatively common condition, affecting approximately 50 to 230 people per 100,000. Rubbing the eyes is considered a significant contributing factor in the onset of keratoconus. Keratoconus is usually identified during the second or third decade of life [1-5].

Early stages of keratoconus can be recognised through diagnostic approaches, such as handheld keratoscopes, slit-lamp biomicroscopy, ultrasonic pachymetry, tomography, and topography methods, for example Optical Coherence Tomography (OCT) and Scheimpflug imaging [6-12].

OCT uses low-coherence interferometry with near-infrared light to create detailed images of tissue architecture, such as profiles of corneal layer thickness. It determines the time delay of infrared light reflected from the anterior segment relative to a reference reflection. Fourier-domain and time-domain are two types of this imaging technique. Fourier-domain relies on a fixed mirror, whereas in time-domain the position of the reference mirror is varied [13,11].

3.2 Artificial intelligence

Artificial intelligence is a broad concept describing the application of computers to simulate intelligent behaviour with minimal human involvement. Artificial Intelligence has grown increasingly significant in ophthalmology, especially in the domain of image analysis. Its use in diagnosing eye conditions has expanded considerably since the 1970s. Machine learning, part of artificial intelligence, permits machines to learn and enhance their functioning over time. Machine learning algorithms can be categorised into three types: (i) unsupervised learning, which involves identifying patterns without prior labels; (ii) supervised learning, which uses classification and prediction methods based on previously labelled examples; and (iii) reinforcement learning, which develops strategies for operating within a specific problem space by utilising sequences of rewards and penalties. Deep learning, a specialised subdivision of machine learning, boosts the accuracy of motion detection, as well as image and speech recognition [14-16].

The studies reported medical artificial intelligence applications in fields such as oncology [17-26] cardiology, neurology [27-32], cancer diagnosis, pneumology, dentistry [33-40], obstetrics, and gynaecology [41-43]. Also, artificial intelligence research is well supported in ophthalmology, where digital tools such as colour fundus photography and OCT provide extensive datasets [44]. Artificial intelligence is applicable in the field of retinal research, particularly in cases of age-related macular

degeneration, diabetic retinopathy, and retinopathy of prematurity, as well as in cataracts, glaucoma, keratoconus, and other anterior segment diseases [45]. Keratoconus has been detected using a deep learning algorithm in several studies [46-55].

3.3 Materials

3.3.1 Instrument

The device used to acquire the raw data was the cornea/anterior segment OCT Casia2 (Tomey Corporation, Nagoya, Japan) [56]. Figures 1 and 2 show this device, which functions as a diagnostic tool for OCT imaging. It captures images of the anterior section of the eye. This instrument applies OCT with a 1310 nm wavelength for measuring the thickness of the cornea, the distance from the anterior corneal surface to the anterior surface of the crystalline lens, and the distance from the posterior corneal surface to the anterior surface of the crystalline lens. The cornea/anterior segment OCT Casia2 is a Swept-Source Optical Coherence Tomography (SS-OCT)-based instrument. In comparison with spectral-domain OCT, which uses a broadband near-infrared superluminescent diode as a light source with a wavelength of around 840 nm, SS-OCT operates at a longer wavelength, enabling better signal detection from underlying layers [13].

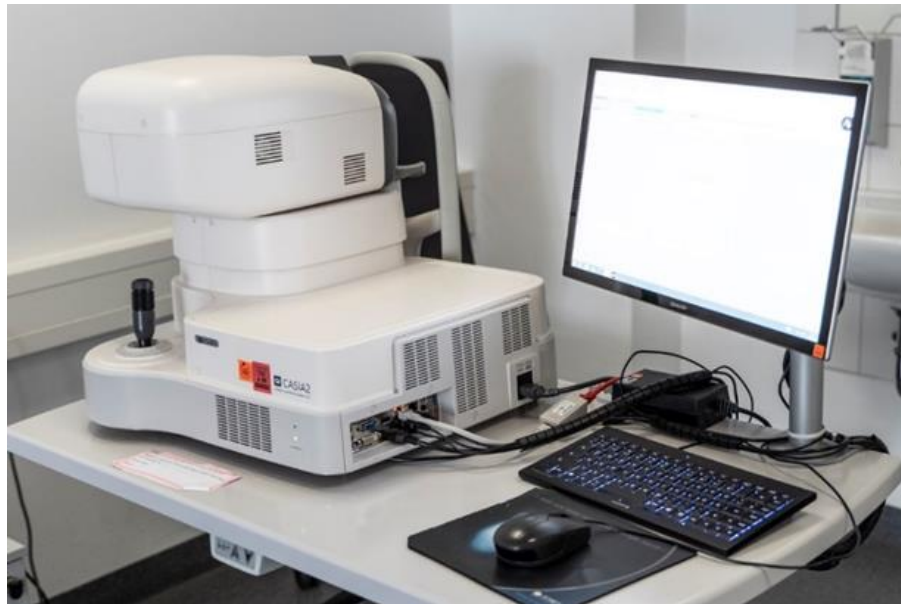


Figure 1. Cornea/anterior segment OCT Casia2



Figure 2. Patient's side of the cornea/anterior segment OCT Casia2

The scan measures thirteen mm in depth and sixteen mm in diameter. The 'Anterior Segment' mode of the instrument allows highly sensitive assessments of the cornea and intraocular lens, while imaging of the posterior lens is not possible. On the other hand, the 'Lens' mode of the instrument provides a view from the cornea to the posterior lens. Within this study, imaging of the posterior lens is unnecessary for diagnosing ectatic corneal diseases; therefore, the 'Anterior Segment' mode was selected. Figure 3 shows the right-eye view of a patient in the Casia2 software.



Figure 3. Measurement screen of the Casia2 software

3.3.2 Data

Data were collected from patients who went through examination at the the Department of Ophthalmology, Saarland University Medical Centre, Homburg, Germany over the period from 1 February 2021 to 1 September 2023.

The Casia2 generates three-dimensional raw data (3dv), with each 3dv file associated with the corneal map having a size of 36.6 MB. Each 3dv file has the data of 16 equiangular meridional images saved in 16-bit unsigned integer format, with pixel values from 0 to 65,535. Figure 4 illustrates a portion of the pixel values from sixteen equiangular meridional images of a single 3dv file.

[[14614 18936 22861 ... 23652 19429 22299] [19470 18490 22978 ... 23809 19317 23730] [21248 16277 23462 ... 23628 17958 21571] ... [21328 21885 22035 ... 13426 17584 17465] [20494 16342 21173 ... 20799 13727 21522] [18750 19428 20001 ... 21231 15274 18829]]	[[18357 18818 22263 ... 22442 17097 21204] [19459 21872 21874 ... 21380 19912 17946] [21699 21951 22883 ... 23173 16926 16237] ... [20488 20361 19826 ... 17220 18253 21432] [19484 22053 17461 ... 17323 21880 18716] [21739 21010 20106 ... 19892 22411 17983]]	[[23470 13306 22826 ... 22987 21595 21563] [22827 19395 19112 ... 22393 23256 23303] [22120 16110 19116 ... 21501 22125 23149] ... [19774 21236 19902 ... 20009 19423 14492] [21075 19565 21145 ... 19275 21399 20770] [20494 17129 20524 ... 15120 15525 11330]]	[[20715 22580 23826 ... 21297 21311 21810] [20602 21598 22025 ... 22051 16979 23378] [19607 19736 17913 ... 22034 22894 23709] ... [20329 20841 17115 ... 18343 20524 18724] [21715 20909 21552 ... 18698 20424 19434] [19876 20398 19475 ... 18857 19170 16193]]
[[19228 20333 21332 ... 21944 22079 19896] [18530 18959 21802 ... 20092 19613 15114] [23412 19219 22535 ... 17848 18671 18489] ... [20404 16777 16058 ... 22287 20044 18251] [20258 15814 17002 ... 22515 21995 18714] [17748 16951 19764 ... 20944 23025 17932]]	[[17045 21751 24142 ... 22781 21422 22091] [20321 21515 21920 ... 20217 18613 21611] [23012 20366 18536 ... 22876 20972 19512] ... [21830 18217 12577 ... 19032 20721 19529] [19414 21615 15385 ... 15006 20918 18178] [20615 12351 20840 ... 20228 20519 20958]]	[[27064 21580 22785 ... 20298 15424 22867] [24799 23579 22969 ... 19408 16686 22648] [28720 24325 23190 ... 20919 19968 21822] ... [27015 22174 20091 ... 20844 20304 11280] [24670 23787 20122 ... 21051 19508 21045] [23915 20582 22961 ... 18062 12792 21893]]	[[23432 20505 15377 ... 18260 22128 23380] [22259 19943 19537 ... 20610 5064 21391] [20799 16293 22616 ... 21107 21522 20239] ... [23861 21445 21423 ... 23219 22227 17591] [24468 23069 19906 ... 23982 21989 20905] [23994 19808 21912 ... 23671 22547 19125]]
[[17282 22590 19420 ... 21671 21732 20153] [18402 21962 22403 ... 22429 23017 14165] [19241 18701 23958 ... 22356 20289 19820] ... [20723 18666 16253 ... 21259 20854 21395] [19965 19446 17595 ... 21369 19319 21664] [18131 20538 21933 ... 21947 20898 18470]]	[[21109 22437 23412 ... 22255 21193 21406] [22955 22223 22276 ... 20127 21648 20770] [21861 21833 22337 ... 20337 18295 18750] ... [22132 20308 20145 ... 20376 19563 22126] [22290 22488 19341 ... 21848 20113 23458] [19439 22737 19764 ... 22143 20951 23634]]	[[19664 23677 21098 ... 20386 18648 19302] [18476 22603 19924 ... 21543 22281 22227] [20025 20319 19016 ... 18460 24147 21928] ... [19977 21997 15724 ... 21270 20757 21938] [17804 21744 19031 ... 22265 19980 21595] [19821 21324 20561 ... 19340 13323 15483]]	[[12584 22167 21156 ... 17659 17629 20774] [20669 21453 21900 ... 20341 21164 16388] [22179 19763 19770 ... 22389 22766 21498] ... [21374 20734 13133 ... 17758 10875 15894] [19548 17501 17933 ... 19874 19202 21650] [19234 18693 19289 ... 18336 21267 19873]]
[[22723 19105 19354 ... 21881 16952 20560] [21874 19955 22712 ... 19296 20495 15355] [22261 19043 21987 ... 20908 21282 14213] ... [21959 17230 13373 ... 20260 19540 22295] [20018 19052 18901 ... 19828 19124 20345] [21450 15221 17873 ... 18420 19526 19110]]	[[19612 19952 21751 ... 21642 23441 24713] [20342 21067 22991 ... 22603 21939 23057] [21400 18590 23781 ... 23378 21963 18235] ... [19680 20039 20899 ... 19953 22340 19172] [21330 21506 19756 ... 16838 23387 16981] [17001 22807 16612 ... 18958 23624 19455]]	[[21605 18485 22628 ... 22764 19985 21992] [21632 16799 21236 ... 23514 19680 23066] [23048 18497 15536 ... 20975 20036 22500] ... [19135 19396 20883 ... 17600 20136 20567] [19360 18064 18110 ... 18417 20934 20402] [19338 16694 19137 ... 20195 17845 12711]]	[[20868 14840 22436 ... 20163 21182 23661] [18057 18926 21710 ... 20406 23533 22422] [20543 21354 16166 ... 16561 22339 22896] ... [18690 18386 21031 ... 20540 19503 17708] [18502 22102 19864 ... 19539 12295 21165] [18873 23062 17803 ... 18669 19386 19013]]

Figure 4. A portion of the pixel values from a single 3dv file

Every 3dv file is accompanied by a corresponding xpf file, which includes information regarding the examination, such as whether the left or the right eye was examined, the date, the time, and the protocol name. Figure 5 consists the data of an xpf file.

```

614711-26709-1 - Notepad
File Edit Format View Help
[System]
MachineName=CASIA2
SystemVersion=50.5A.03
SerialNo.=614711

[Measurement]
PatientID=nw12121998
Eye=Left
Date=2022/10/04
Time=13:33:47
ExamProtocolName=Anterior Segment
ExamProtocolType=2
ExamProtocolNo=26709
ExamIndex=1
ScanTypeName=Corneal Map(A)
ScanMode=3D
ScanMethod=Radial
ScanType=20
ScanAngle=0
SliceRepeat=1
Averaged3dv=0
ZeroPoint=Negative
VoxelBits=16
AB-Scan=800
BC-Scan=16
Depth=1464
AB-Range=16
BC-Range=16
MmPerPixZ=0.00751
FixationType=0
FixationLightPosition=3
Comment=
Autoshot=false
AutoAlignment=false
Use_PreOpe=false
EyeTracking=false
VIS_Capture=0
VIS_Live=0
TempVisPower=100
AlignmentZOffset=0

[AdditionalMeasurement]
Count=1
ScanMode=2D
ScanMethod=Cross
ScanAngle=0
AB-Scan=800
BC-Scan=2
AB-Range=16
BC-Range=16
SliceRepeat=8
Averaged3dv=true
FileName=614711-26709-1_1.3dv
Ln 54, Col 1 100% Windows (CRLF) UTF-8

```

Figure 5. Data of an xpf file

Identifying ectatic corneal diseases through the Ectasia Screening Index (ESI) involves independently assessing the anterior and posterior corneal shapes, with the final determination considering both evaluations.

The anterior cornea score is calculated as follows:

$$\text{Anterior cornea score} = 0.18\text{Sph} + \text{Asy} - 0.1\text{Reg} - 8.88 - 0.28 \quad (1)$$

where Sph is the spherical component of Fourier analysis within a 6 mm range, Asy is the asymmetry component of Fourier analysis within a 6 mm range, and Reg is the regular astigmatism component of Fourier analysis within a 6 mm range. Higher values of Sph and Asy indicate that keratoconus is progressing, whereas a relatively high Reg value suggests regular astigmatism rather than keratoconus.

The posterior cornea score is calculated as follows:

$$\text{Posterior cornea score} = -0.42\text{Steepest} + \text{Asy} - 0.78\text{Reg} - 0.2\text{Hio} + 2.38 \quad (2)$$

where Steepest is the minimum value of instantaneous power within a 6 mm range, Asy and Reg are as defined in formula (1), and Hio is the higher-order irregular astigmatism component of Fourier analysis within a 6 mm range. A relatively high Hio value indicates a normal eye rather than keratoconus.

Of the values derived from the anterior cornea score and posterior cornea score, the higher value is taken as the determinant. The ESI scale spans from 0 to 95. A result from 0 to 4 represents no ectasia pattern, an ESI value from 5 to 29 represents suspected ectasia, and a result from 30 to 95 represents clinical ectasia. The ESI of each measurement is recorded in a csv file, which is exportable via the Casia2 software. Figure 6 presents a segment of a csv file displaying ESI values.

	DW	DX	DY	DZ	EA	EB	EC	ED	EE	EF	EG
1	[Fourier Cylinder]				[Ectasia Screening]						
2	FKCyl	FKCyl Axis	FPCyl	FPCyl Axis	FRCyl	FRCyl Axis	ESI	ESI Status	Sph.[Keratometric]	Reg.[Keratometric]	Asy.[Keratometric]
3	[D]	[degree]	[D]	[degree]	[D]	[degree]	[%]	[-]	[D]	[D]	[D]
4	-0.39	92	-0.345	73	-0.712	81	10	Suspect	43.61	0.33	0.28
5	-1.573	46	-0.318	75	-1.94	50	31	Abnormal	43.06	0.9	0.79
6	-6.449	166	-0.161	92	-7.089	165	62	Abnormal	46.45	2.57	3.79
7	-3.309	154	-0.527	78	-3.431	151	93	Abnormal	40.04	2.43	7.73
8	-6.007	1	-1.103	160	-7.541	179	50	Abnormal	43.41	2.43	0.85
9	-1.176	164	-0.089	27	-1.325	166	0	Normal	44.03	0.45	0.26
10	-2.446	3	-0.108	82	-2.641	3	41	Abnormal	43.02	0.78	0.7
11	-1.092	162	-0.597	58	-0.761	173	36	Abnormal	43.51	0.64	0.66
12	-1.019	172	-0.109	32	-1.162	175	6	Suspect	44.07	0.43	0.21
13	-7.805	34	-1.731	92	-8.169	41	93	Abnormal	45.54	2.73	6.83
14	-5.702	23	-0.689	94	-6.014	24	92	Abnormal	75.26	2.86	1.3
15	-7.914	17	-0.508	98	-8.456	17	95	Abnormal	74.64	3.39	3.16
16	-2.546	161	-0.864	59	-2.116	167	64	Abnormal	50.24	1.31	2.13
17	-11.41	13	-1.728	112	-11.18	12	68	Abnormal	48.31	3.95	2.31
18	-0.974	17	-0.27	108	-0.825	17	8	Suspect	43.39	0.44	0.23
19	-1.59	164	-0.153	62	-1.642	165	6	Suspect	43.31	0.5	0.16
20	-1.583	150	-0.222	69	-1.567	149	0	Normal	45.19	0.67	0.7
21	-12.133	14	-1.108	101	-12.59	14	32	Abnormal	42.73	4.94	3.08

Figure 6. A segment of a csv file

Figure 7 shows 16 equiangular meridional images acquired from the 3dv file illustrated in Figure 4.

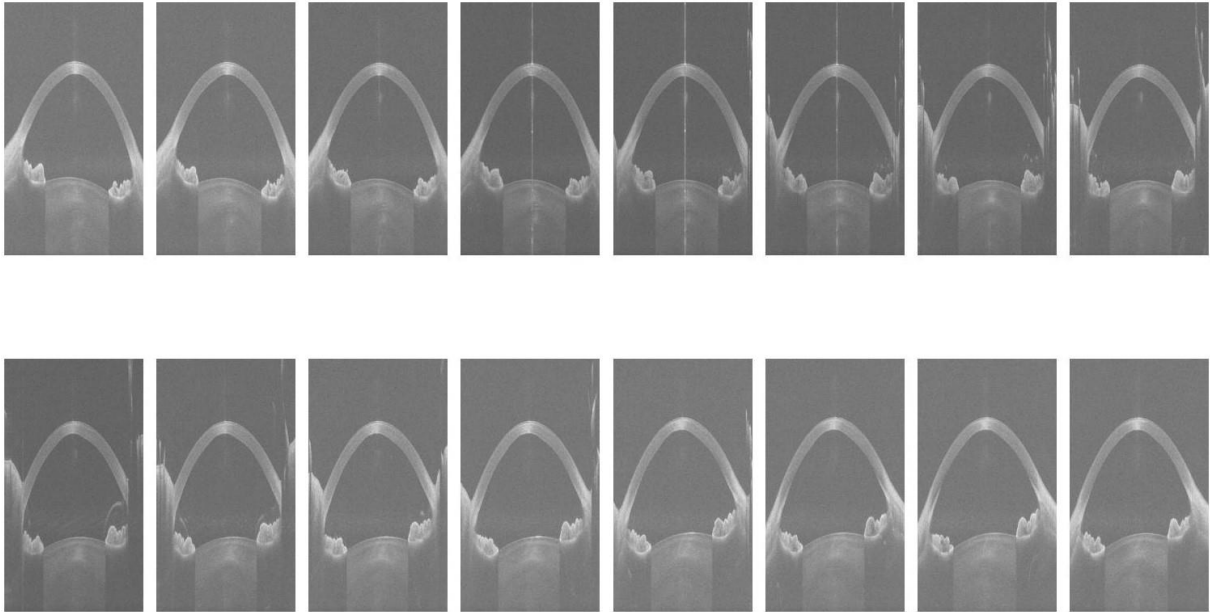


Figure 7. Equiangular meridional images acquired from a 3dv file

3.4 Metrics and tools for interpreting results

This section provides an overview of the tools and metrics used in the three articles.

3.4.1 Software

In this study, Python was used as the software for extracting sixteen images from each 3dv file and for training the models. Python holds advantages over other programming languages, such as its extensive range of libraries, like Pandas, which provides diverse data structures and tools required for data analysis in fields such as statistics and engineering. NumPy serves as the fundamental library for scientific computing in Python, while Matplotlib enables the creation of two-dimensional plotted graphs [57].

The PyTorch library was employed for training the models. It provides a Pythonic coding style that treats code as a model and facilitates code correction. This approach aligns with other well-known computational libraries, ensuring efficiency and compatibility with hardware accelerators like graphics processing units [58].

3.4.2 Convolutional neural network

Convolutional Neural Networks (CNNs) are artificial intelligence models that can find, recognise, and group objects, in addition to detecting them in images. CNNs are a specialised type of artificial neural network [59]. Artificial neural networks simulate the processes of the brain by using nodes and their interconnections. Each node contains an input, which obtains signals from other nodes, and an output, which conveys information to other nodes [60].

The convolutional layer is a component of the CNN architecture. It consists of a series of kernels applied to the input data. Each kernel, defined by its width, height, and weights, serves to extract features from

the data. The feature map results from applying these kernels to the input image. Figure 8 shows a three-by-three image matrix and a two-by-two kernel matrix as an example.

	Image	Kernel	Feature map																	
Step 1	<table border="1"> <tr><td>1</td><td>12</td><td>3</td></tr> <tr><td>15</td><td>57</td><td>13</td></tr> <tr><td>4</td><td>12</td><td>2</td></tr> </table>	1	12	3	15	57	13	4	12	2	<table border="1"> <tr><td>0</td><td>1</td></tr> <tr><td>1</td><td>0</td></tr> </table>	0	1	1	0	<table border="1"> <tr><td>27</td><td></td></tr> <tr><td></td><td></td></tr> </table>	27			
1	12	3																		
15	57	13																		
4	12	2																		
0	1																			
1	0																			
27																				
Step 2	<table border="1"> <tr><td>1</td><td>12</td><td>3</td></tr> <tr><td>15</td><td>57</td><td>13</td></tr> <tr><td>4</td><td>12</td><td>2</td></tr> </table>	1	12	3	15	57	13	4	12	2	<table border="1"> <tr><td>0</td><td>1</td></tr> <tr><td>1</td><td>0</td></tr> </table>	0	1	1	0	<table border="1"> <tr><td>27</td><td>60</td></tr> <tr><td></td><td></td></tr> </table>	27	60		
1	12	3																		
15	57	13																		
4	12	2																		
0	1																			
1	0																			
27	60																			
Step 3	<table border="1"> <tr><td>1</td><td>12</td><td>3</td></tr> <tr><td>15</td><td>57</td><td>13</td></tr> <tr><td>4</td><td>12</td><td>2</td></tr> </table>	1	12	3	15	57	13	4	12	2	<table border="1"> <tr><td>0</td><td>1</td></tr> <tr><td>1</td><td>0</td></tr> </table>	0	1	1	0	<table border="1"> <tr><td>27</td><td>60</td></tr> <tr><td>61</td><td></td></tr> </table>	27	60	61	
1	12	3																		
15	57	13																		
4	12	2																		
0	1																			
1	0																			
27	60																			
61																				
Step 4	<table border="1"> <tr><td>1</td><td>12</td><td>3</td></tr> <tr><td>15</td><td>57</td><td>13</td></tr> <tr><td>4</td><td>12</td><td>2</td></tr> </table>	1	12	3	15	57	13	4	12	2	<table border="1"> <tr><td>0</td><td>1</td></tr> <tr><td>1</td><td>0</td></tr> </table>	0	1	1	0	<table border="1"> <tr><td>27</td><td>60</td></tr> <tr><td>61</td><td>25</td></tr> </table>	27	60	61	25
1	12	3																		
15	57	13																		
4	12	2																		
0	1																			
1	0																			
27	60																			
61	25																			

Figure 8. The use of a kernel to produce a feature map

According to Figure 8, a kernel is applied to an image. In Step 1, the selected four elements of the image are multiplied individually by the elements of the kernel and the results of these four multiplications are then added together. The sum, which is 27, fills one cell of the output. The kernel then moves one cell horizontally across the image and the multiplication process is repeated. The result for Step 2 is 60. When there is no space left for the kernel to move horizontally, it shifts one cell vertically from the left side of the image and the process is repeated. The result of Step 3 is 61. Finally, the kernel moves one cell horizontally again, and the multiplication and addition process continues. In Step 4, the outcome is 25. By applying the kernel to the image, the feature map becomes a two-by-two matrix. Formula (3) represents the size of the feature map [59].

$$FM = I - K + 1 \quad (3)$$

According to formula (3), the Feature Map (FM) size is obtained by subtracting the Kernel matrix (K) size from the Image matrix (I) size and then adding one. For example, in Figure 8, the size of the feature map is $3 - 2 + 1$, which equals 2. In Figure 8, the stride for the kernel's movement is one. This means the kernel moves across the image with a step size of one cell, both horizontally and vertically. Depending on the size of the image and the kernel, the stride value for the kernel's movement can be adjusted. For instance, with a five-by-five image and a two-by-two kernel, the stride can be set to 2.

Increasing the stride has the advantage of reducing the size of the feature map. If the stride is not equal to one, formula (3) is modified to formula (4), as shown below [59].

$$FM = \frac{I-K}{S} + 1 \quad (4)$$

For example, if the stride is set to two, the size of the feature map, based on formula (4), is calculated as $\frac{5-2}{2} + 1$, which rounds down to two. In this case, the kernel can only be applied once horizontally and vertically, covering just four cells of the image in two dimensions. Consequently, two edges of the image would be missed. To solve this problem, zero padding can be applied to the input image. Zero padding involves adding zeros around the edges of the image. For instance, applying one unit of zero padding would transform the input image into a five-by-five matrix, as shown in image (a) in Figure 9.

0	0	0	0	0
0	1	12	3	0
0	15	57	13	0
0	4	12	2	0
0	0	0	0	0

(a)

0	0	0	0	0
0	1	12	3	0
0	15	57	13	0
0	4	12	2	0
0	0	0	0	0

(b)

0	0	0	0	0
0	1	12	3	0
0	15	57	13	0
0	4	12	2	0
0	0	0	0	0

(c)

0	0	0	0	0
0	1	12	3	0
0	15	57	13	0
0	4	12	2	0
0	0	0	0	0

(d)

0	0	0	0	0
0	1	12	3	0
0	15	57	13	0
0	4	12	2	0
0	0	0	0	0

(e)

Figure 9. (a) Adding one zero padding and (b-e) applying a filter to the image

Now, with a stride of two, the kernel can cover all the original image elements. Although the two edges of the padded image are missed, they contain no data from the original image. When zero padding is applied to the image, formula (4) is modified as follows:

$$FM = \frac{I+2P-K}{S} + 1 \quad (5)$$

In formula (5), P represents the amount of zero padding applied to the image. For example, in Figure 9, P is one, and the size of the feature map, based on formula (5), is calculated as $\frac{3+2-2}{2} + 1$, which rounds down to 2.

The pooling layer reduces feature map dimensionality and preserves the most important data. Different pooling methods exist, like average pooling, maximum pooling, and minimum pooling. A feature map is divided into regions and pooling is applied to them. For example, Figure 10 shows a four-by-four feature map, to which max pooling is applied over four regions. According to Figure 10, in every region of the feature map, the maximum value is selected as the result [59].

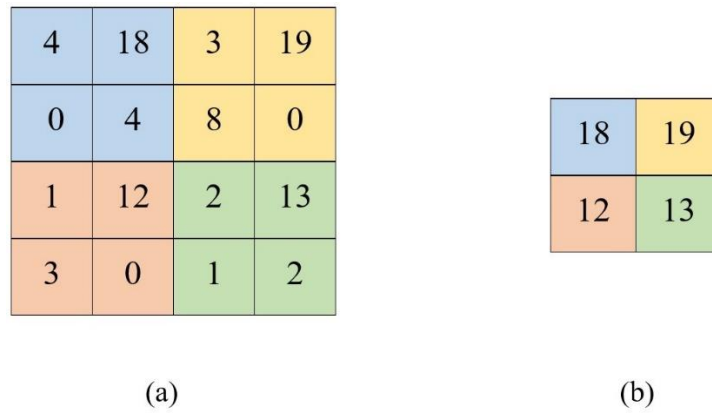


Figure 10. (a) A feature map (b) The result of applying max pooling to the feature map

The nonlinearity layer comes after the convolution [59]. Activation functions introduce nonlinearity to the network [61]. If a network does not include activation functions, its output will always be a linear combination of the input, no matter how many layers it has. Consequently, the intermediate layers have no effect on the final result [62].

The hyperbolic tangent can be used as an activation function. The output of the hyperbolic tangent lies between -1 and 1 [35]. Formula (6) represents this function [35]. In formula (6), x is the input to the function.

$$f(x) = \frac{e^x - e^{-x}}{e^x + e^{-x}} \quad (6)$$

Using the hyperbolic tangent as an activation function in deep neural networks causes the problem of vanishing gradient [61].

The sigmoid function can also be used as an activation function. The sigmoid function transforms input values into outputs ranging between 0 and 1, as described by formula (7) [61]. In formula (7), x is the input to the function.

$$f(x) = \frac{1}{1+e^{-x}} \quad (7)$$

Like the hyperbolic tangent, using the Sigmoid function as an activation function in deep neural networks causes the problem of vanishing gradient [61].

The softmax function is employed in the CNNs' output layer to perform multi-class classification tasks. It transforms the final layer's output into a probability distribution across classes [61]. In formula (8), the calculation of softmax function is presented [63]. In formula (8), $x_1, x_2, x_3, \dots, x_N$ are the inputs to the function [63].

$$f(x_i) = \frac{e^{x_i}}{\sum_{j=1}^N e^{x_j}} \quad i = 1, 2, 3, \dots, N \quad (8)$$

The rectified linear unit (ReLU) function is another option for an activation function. It has the ability to mitigate the vanishing-gradient problem during the training process [61]. In the hyperbolic tangent and sigmoid functions, when the input value is too small or too big, the gradient of the function becomes small, which leads to slow convergence [62]. However, the ReLU function has two constant derivative values, 0 and 1; therefore, there is no problem with converging slowly [62]. If the input to this function is negative, the output is zero; if the input is zero or positive, the output is equal to the input [61]. Formula (9) defines the ReLU function. In formula (9), x is the input to the function.

$$f(x) = \begin{cases} 0 & x < 0 \\ x & x \geq 0 \end{cases} \quad (9)$$

In a fully connected layer, every neuron of the previous layer links to all neurons of the current layer. This layer is usually positioned at the network's end to produce the final output [60].

Figure 11 shows a typical CNN architecture for three-class classification, where $P_1, P_2,$ and P_3 represent the probabilities of Class 1, Class 2, and Class 3, respectively.

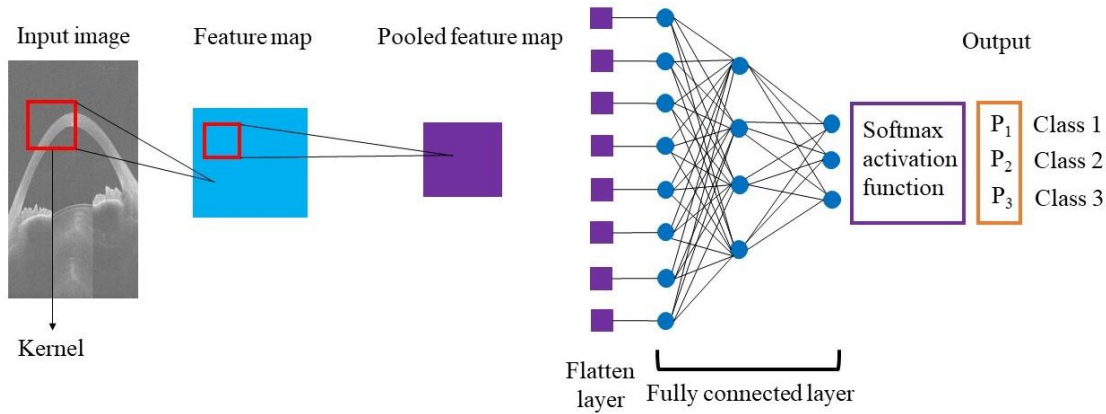


Figure 11. CNN architecture

The loss function measures the discrepancy between the predicted output and the actual target. In CNNs, the loss function is applied to both regression tasks, where the outputs are continuous rather than discrete values such as 0 and 1, and classification tasks, where the outputs are discrete, with the aim of minimising the loss. Mean Squared Error (MSE) can be used as the loss function with regression problems [62].

MSE is expressed in formula (10)

$$\text{MSE} = \frac{1}{N} \sum_{i=1}^N |y_i - \hat{y}_i|^2 \quad (10)$$

where N denotes the total number of actual targets, which equals the number of predicted outputs; y_i denotes the actual target at position i , and \hat{y}_i is the corresponding predicted output [64].

Cross entropy loss can be used as the loss function with classification tasks [62].

In an N -class problem, where there are N possible categories, a neural network maps an input x to a score vector of $[s_1, s_2, \dots, s_N]^T$. The softmax function, as described in formula (11), converts these scores into probabilities:

$$p_i = \frac{e^{s_i}}{\sum_{l=1}^N e^{s_l}} \quad (11)$$

where p_i denotes the predicted probability of class i .

The cross-entropy loss is given by formula (12)

$$\text{CEL} = -\log(p_L) = -\log \frac{e^{s_L}}{\sum_{l=1}^N e^{s_l}} \quad (12)$$

where L denotes the true class label [65].

Optimisers are used during training to minimise the loss function [62].

Overfitting is a major issue in deep neural networks that have a large number of parameters [66]. In this scenario, the model performs excellently on the training data but does not generalise well to the validation data. An overfitted model often memorises the training data rather than capturing the essential structure and patterns of the information. As shown in Figure 12, with an increase in the number of epochs, where an epoch refers to one complete pass of the training data through the neural network, the training error, which assesses how well the model performs on the training data, continuously decreases, whereas the validation error exhibits a different pattern. It decreases initially but starts to rise after reaching a certain point. Stopping the learning process, the iterative procedure by which the neural network adjusts its parameters to minimise error, before this point results in underfitting, while stopping it after the point leads to overfitting. Therefore, the optimal approach is to stop the learning process when the validation error is at its minimum [67].

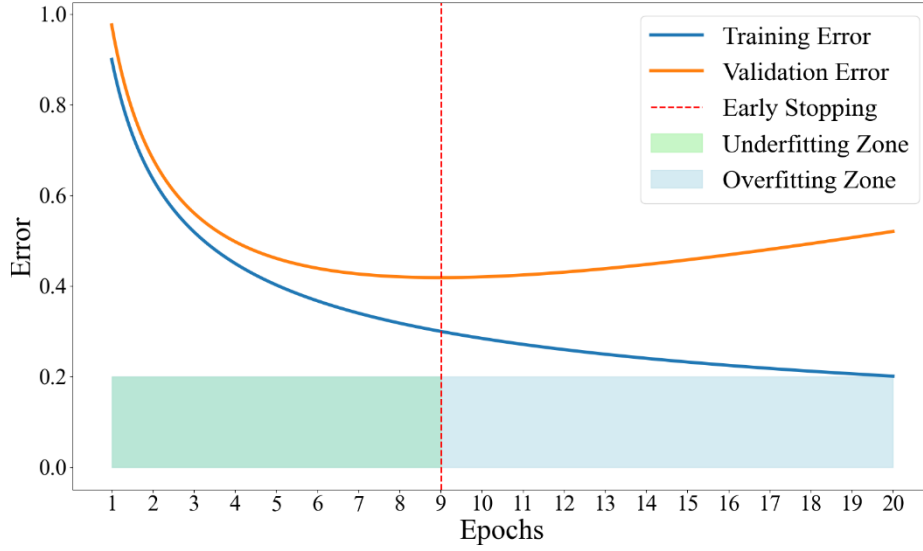


Figure 12. Training and validation errors over epochs

To mitigate overfitting, three main techniques are outlined below: dropout, L1 regularisation, and L2 regularisation.

Dropout is a method that randomly disables units and their associated connections in the neural network during training to reduce overfitting. Dropout ensures that units are active in the neural network with a probability of p during training, but during testing, all units are retained, with their weights scaled by p [68].

Regularisation techniques are employed to avoid overfitting, where the model excels on the training data but underperforms on the validation data, by incorporating a term into the loss function, which promotes simpler or smaller weights for the model. Among the most widely used regularisation techniques are L1 and L2 [61].

L1 regularisation incorporates a component to the loss function that depends on the absolute values of the weights, encouraging sparsity in the model's parameters. Formula (13) illustrates the regularised loss function for L1 regularisation. In this equation, $L(w)$ represents the original loss function, w_i refers to the i th weight, n indicates the total number of weights, and λ is the regularisation strength.

$$\tilde{L}(w) = L(w) + \lambda \sum_{i=1}^n |w_i| \quad (13)$$

L2 regularisation incorporates a component to the loss function that depends on the squared values of the weights, which encourages the model to maintain smaller weights. Formula (14) defines the regularised loss function for L2 regularisation. In formula (14), $L(w)$, w_i , n , and λ carry the same meanings as in formula (13).

$$\tilde{L}(w) = L(w) + \frac{\lambda}{2} \sum_{i=1}^n w_i^2 \quad (14)$$

Below is an introduction to some CNN models that were used for predicting the ESI and corneal condition.

3.4.2.1 DenseNets

A single input image x_0 is processed by a convolutional neural network consisting of L layers. Each layer applies a non-linear transformation $H_l(\cdot)$, with l representing the layer index. The transformation $H_l(\cdot)$ may comprise a sequence of processes, including batch normalisation, which normalises the feature maps produced following convolution, rectified linear unit (ReLU), pooling, or convolution [69].

The output of the l -th layer is denoted as x_l . Dense connectivity is employed such that each layer is directly connected to every following layers. Consequently, the input to the l -th layer consists of the concatenated feature maps generated by every previous layer, $[x_0, x_1, \dots, x_{l-1}]$, and is expressed as

$$x_l = H_l([x_0, x_1, \dots, x_{l-1}]) \quad (15)$$

In formula (15), $[x_0, x_1, \dots, x_{l-1}]$ denotes the combined feature maps from layers 0 through $l-1$. This dense pattern of inter-layer connections defines the architecture known as the Dense Convolutional Network (DenseNet) [69].

DenseNet architectures are available in various models, such as DenseNet-121, DenseNet-169, DenseNet-201, and DenseNet-264, where the numerical designation denotes the total layer count in each model [69].

3.4.2.2 EfficientNets

Scaling up CNNs is a widely adopted approach to improve accuracy. DenseNet, for example, can be scaled from DenseNet-121 to DenseNet-264 by increasing the number of layers. The most common methods for scaling CNNs involve increasing depth, or width, or scaling by input image resolution [70]. In contrast to common approaches that adjust these dimensions arbitrarily, this method adjusts network depth, width, and resolution by using constant coefficients. For example, using 2^N times more computational resources corresponds to increasing network depth by α^N , width by β^N , and size of image by γ^N , with α , β , and γ identified through a grid exploration on the original baseline network. Applying this strategy enables the development of a new baseline network, which can then be scaled to form a family of models known as EfficientNets. These architectures include EfficientNet-B0, EfficientNet-B1, EfficientNet-B2, EfficientNet-B3, EfficientNet-B4, EfficientNet-B5, EfficientNet-B6, and EfficientNet-B7 [70].

3.4.2.3 MobileNets

The MobileNet architecture is built upon depthwise separable convolutions, a type of convolution that splits a convolution to a depthwise convolution and a 1×1 convolution, referred to as a pointwise convolution. The depthwise convolution uses one filter to every input channel, while the pointwise convolution uses a 1×1 convolution to merge the depthwise convolution's outputs. By contrast, through

a standard convolution, inputs are filtered and combined into new outputs in a single stage. The depthwise separable convolution separates these operations into two layers: one performs filtering, and the other performs combination. This factorisation substantially decreases both computational expense and the size of the network, causing it to be appropriate for mobile and embedded vision systems [71].

3.4.2.4 ResNets

Adding more layers to a deep network causes the accuracy to degrade. This degradation problem was solved by introducing a deep residual learning framework. Residual learning is employed in every few stacked layers [72].

The output of a building block follows formula (16) [72].

$$y = F(x, \{W_i\}) + x \quad (16)$$

In formula (16), x is the input to the stacked layers and y is the output of the stacked layers, while $F(x, \{W_i\})$ denotes the residual mapping. The operation $F + x$ is implemented via a shortcut connection. The residual function $F(x, \{W_i\})$ may consist of more than two layers and can represent multiple convolutional layers [72].

ResNet architectures consist of ResNet-18, ResNet-34, ResNet-50, ResNet-101, and ResNet-152, where the numerical designations represent the layer count [72].

3.4.3 Quality criteria

Mean Absolute Error (MAE) can be applied to assess the predictive ability of a network. MAE calculates the average of the absolute differences between the actual and predicted values [62]. Formula (17) demonstrates the calculation of MAE

$$MAE = \frac{1}{N} \sum_{i=1}^N |y_i - \hat{y}_i| \quad (17)$$

where N , y_i , and \hat{y}_i hold the same definitions as provided in formula (10).

The primary metrics used to evaluate a binary classifier are calculated from the four components of the confusion matrix, which summarises the numbers of correct and incorrect predictions made by a model. They are fundamental for measuring the performance of the classifier. True Positive (TP) indicates the count of positive instances accurately identified by the network. True Negative (TN) indicates the count of negative instances accurately identified by the network. False Positive (FP) represents the count of negative instances wrongly identified as positive. False Negative (FN) represents the count of positive instances wrongly identified as negative. Figure 30 displays the confusion matrix.

Actual class	Negative	TN	FP
	Positive	FN	TP
		Negative	Positive
		Predicted class	

Figure 13. Confusion matrix

The following metrics are applied to evaluate how accurately a network categorises the data into two classes [73].

Accuracy indicates the percentage of accurately predicted instances in relation to all instances in the test dataset.

$$\text{Accuracy} = \frac{TP+TN}{TP+FP+TN+FN} \quad (18)$$

Sensitivity calculates the proportion of correctly identified positive instances among all the true positive cases.

$$\text{Sensitivity} = \frac{TP}{TP+FN} \quad (19)$$

Specificity indicates the proportion of correctly classified negative instances among all the actual negative samples.

$$\text{Specificity} = \frac{TN}{TN+FP} \quad (20)$$

Positive Predictive Value (PPV) is the proportion of accurately recognised positive samples among all samples predicted as positive.

$$\text{PPV} = \frac{TP}{TP+FP} \quad (21)$$

In cases of unbalanced datasets, in which one class occurs significantly more often in comparison with the other, the F1 score provides a more reliable measure. Accuracy, sensitivity, and specificity may fail to properly assess model performance, but the F1 score ensures a more balanced evaluation.

$$\text{F1} = 2 \cdot \frac{\text{PPV} \times \text{Sensitivity}}{\text{PPV} + \text{Sensitivity}} \quad (22)$$

When regression outputs are used for binary decision-making, an appropriate decision threshold must first be selected. Once this threshold has been determined, the continuous predictions are converted into two classes so that confusion matrix values can be calculated. Predictions that meet or exceed the

threshold are assigned to the positive class, while those below it are assigned to the negative class. In this threshold-based classification setting, it is necessary to balance sensitivity and specificity, as increasing one can reduce the other. To identify a suitable trade-off, the Receiver Operating Characteristic (ROC) curve can be analysed. A common approach is to select the threshold that maximises the disparity between sensitivity (true positive rate) and $1 - \text{specificity}$ (false positive rate), a method known as Youden's J statistic.

4. Publications

4.1 Article 1

This article focuses on predicting the ESI from raw OCT data obtained from the cornea/anterior segment OCT Casia2 by using adapted DenseNet121, EfficientNet-B0, and ResNet18 as CNN models. The dataset was classified according to an ESI of 30, as defined by the Casia2. ESI values of 30 and above denoted the *Keratoconus* class, reflecting the presence of clinical ectasia, whereas ESI values of less than 30 were classified as *Not Keratoconus*, reflecting either a suspicion of ectasia or the absence of any ectatic pattern [74]. A correction has been published for this article regarding the correct uploading of the dataset and codes to a repository [75].

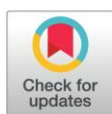
RESEARCH ARTICLE

Prediction of the ectasia screening index from raw Casia2 volume data for keratoconus identification by using convolutional neural networks

Maziar Mirsalehi^{1*}, Benjamin Fassbind¹, Andreas Streich², Achim Langenbucher¹

1 Department of Experimental Ophthalmology, Saarland University, Homburg, Germany, **2** Department of Computer Science, Eidgenössische Technische Hochschule, Zürich, Switzerland

* mami00016@stud.uni-saarland.de(MM)



OPEN ACCESS

Citation: Mirsalehi M, Fassbind B, Streich A, Langenbucher A (2025) Prediction of the ectasia screening index from raw Casia2 volume data for keratoconus identification by using convolutional neural networks. *PLoS One* 20(9): e0311036.
<https://doi.org/10.1371/journal.pone.0311036>

Editor: Georgios Labiris, Democritus University of Thrace, GREECE

Received: September 11, 2024

Accepted: August 7, 2025

Published: September 2, 2025

Copyright: © 2025 Mirsalehi et al. This is an open access article distributed under the terms of the [Creative Commons Attribution License](https://creativecommons.org/licenses/by/4.0/), which permits unrestricted use, distribution, and reproduction in any medium, provided the original author and source are credited.

Data availability statement: The dataset and codes have been uploaded to a repository. The DOI is: <https://doi.org/10.5281/zenodo.16846551>.

Funding: M M was supported in part by the Rolf M. Schwiete Stiftung under project nr. 2020-024 (<https://schwiete-stiftung.com/>). The funders had no role in study design, data

Abstract

Purpose Prediction of the ectasia screening index, an estimator provided by the Casia2 instrument for identifying keratoconus, from raw optical coherence tomography data using convolutional neural networks.

Methods Three convolutional neural networks models (ResNet18, DenseNet121 and EfficientNetB0) were employed to predict the ectasia screening index. Mean absolute error was used as the performance metric for predicting the ectasia screening index by the adapted convolutional neural network models on the test set. Scans with an ectasia screening index value higher than a certain threshold were classified as *Keratoconus*, while the remaining scans were classified as *Not Keratoconus*. The architectures' performance was evaluated using metrics such as accuracy, sensitivity, specificity, positive predictive value and F1 score on data collected from patients examined at the eye clinic of the Homburg University Hospital. The raw data from the Casia2 instrument, in 3dv format, was converted into 16 images per examination of one eye. For the training, validation and testing phases, 3689, 1050 and 1078 scans (3dv files) were selected, respectively.

Results In the prediction of the ectasia screening index, the mean absolute error values for the adapted ResNet18, the adapted DenseNet121 and the adapted EfficientNetB0, rounded to two decimal places, were 7.15, 6.64 and 5.86, respectively. In the classification task, the three networks yielded an accuracy of 94.80%, 95.27% and 95.83%, respectively; a sensitivity of 92.07%, 94.64% and 94.17%, respectively; a specificity of 96.61%, 95.69% and 96.92%, respectively; a positive predictive value of 94.72%, 93.55% and 95.28%, respectively; and a F1 score of 93.38%, 94.09% and 94.72%, respectively.

Conclusions Our results show that the prediction of keratoconus based on the ectasia screening index values estimated from raw data outperforms previous approaches using processed data. adapted EfficientNetB0 outperformed both the other adapted models and those in state-of-the-art studies, with the highest accuracy and F1 score.

collection and analysis, decision to publish, or preparation of the manuscript.

Competing interests: The authors have declared that no competing interests exist.

Introduction

Keratoconus describes a disorder of the eye characterised by a cone-shaped cornea with thinning and steepening, which typically affects both eyes of a patient with varying degrees of severity and occurs in both males and females [1]. Keratoconus affects about 1 in every 2000 individuals in the general population [2].

There are two main types of corneal imaging: corneal topography and corneal tomography. In corneal topography, the shape of the anterior part of the cornea is shown but in corneal tomography a three-dimensional image of the whole cornea is shown. Optical Coherence Tomography (OCT) is a corneal tomography technique that assesses the delay of reflected infrared light from the anterior segment by comparing it to a reference reflection. This tomography technique is classified into two types: Fourier domain, which uses a stationary mirror and time domain, which adjusts the position of a reference mirror. Another corneal tomography technique is Scheimpflug imaging where a rotating camera is used to produce cross-sectional images [3].

Artificial Intelligence (AI) enables machines to perform tasks associated with human cognition like writing, speaking and seeing. AI can be used in medical specialties dealing with image analysis like ophthalmology. Machine learning is a subset of AI that enables the machine to learn in order to develop its performance. Deep learning, a specialised branch of machine learning, improves the effectiveness of motion recognition, image and speech [4].

In this study, the neural networks were used to predict the Ectasia Screening Index (ESI) of a given scan automatically. This approach is a regression task since the output of the networks is a numerical value. Also, the scans were classified into two classes, *Keratoconus* and *Not Keratoconus*. The *Keratoconus* class represents ectasia and the *Not Keratoconus* class indicates suspicion of ectasia or no ectasia pattern. This approach has an advantage over other approaches where the output is discrete and belongs to a class. With this approach, if two scans are in the *Keratoconus* class, the severity of ectasia can be compared between them by comparing the predicted ESI provided by the architecture.

The ESI values, which are computed by the instrument's software, are used as labels for training the Convolutional Neural Networks (CNNs). The objective of this study is to estimate the ESI values directly from the raw data produced by the Casia2 instrument. By using raw data, we ensure that the underlying physical information remains consistent, even if the software version changes in the future. In general, data can be utilised as preprocessed data or as raw data. Preprocessed data are altered by software and the details of these modifications may not always be transparent. Moreover, changes in software versions can lead to variations in how data are preprocessed and affect the consistency of results. In contrast, raw data remain unaltered by external software. Therefore, raw data retain their original form across different software versions. This stability in raw data can offer a more consistent and reliable foundation for analysis and model training. This approach differs from training CNNs on the OCT images produced by the software, as those images have already undergone post-processing steps such as noise reduction and filtering. Therefore, training on the raw data is not a redundant task; it allows us to develop a model that learns directly from unaltered input, making the estimation process more robust and independent of software-specific image modifications.

The ESI values provide an indication of whether the eye is clinically healthy, affected by keratoconus, or shows signs suggestive of keratoconus. They assist clinicians in diagnosing the severity of corneal ectasia and in determining the appropriate timing for intervention. Accurate estimation of the ESI is therefore clinically significant, as it supports early detection and management of keratoconus, potentially preventing disease progression and preserving visual function.

To the best of our knowledge, this is the first time that raw OCT data have been used for a regression task to predict the ESI for the purpose of keratoconus diagnosis. Below we briefly review the current neural network-based approaches to automatically identify keratoconus.

State of the art

Zhang et al. [5] explored keratoconus diagnosis by employing the CorNet model. The model was trained and evaluated with a dataset of 1786 raw data from the Corvis ST (Oculus, Wetzlar, Germany). Corvis ST is a non-contact device that measures corneal biomechanics by recording dynamic deformation following a rapid air-puff excitation. Keratoconus was diagnosed by using clinical signs such as stromal thinning, Fleischer's ring and a central K-value greater than 47 dioptres, in addition to other indicators. The CorNet model achieved an accuracy of 92.13%, sensitivity of 92.49%, specificity of 91.54%, Positive Predictive Value (PPV) of 94.77% and an F1 score of 93.62% on the validation set.

Ruiwei Feng et al. [6] introduced a deep learning method named KerNet for identifying keratoconus and sub-clinical keratoconus using raw data from the Pentacam HR system (Oculus, GmbH, Wetzlar, Germany). This system includes a rotating Scheimpflug camera, which gathers three-dimensional data of the cornea and a software which is designed to analyse and display the data. The corneal data, exported from the Pentacam HR system, comprised five numerical matrices for each sample. These matrices were considered as five two-dimensional image slices, representing the front and back surface curvatures, the front and back surface elevations and the pachymetry of the eye. 854 samples were used as dataset. KerNet employed a specialised architecture with five branches to handle the matrices individually as input to identify features, which are subsequently combined for prediction. The model achieved an accuracy of 94.74%, with a sensitivity of 93.71%, PPV of 94.10% and an F1 score of 93.89%.

Schatteburg et al. [7] introduced a plan for using CNNs for keratoconus diagnosis based on the ESI from data of the SS-1000 Casia OCT Imaging System. The dataset sourced from over 1900 patients and included three-dimensional OCT images of both the anterior and posterior cornea, together with parameters calculated by the Casia software. However, the study did not include evaluation metrics.

Fassbind et al. [8] focused on identifying abnormalities such as keratoconus by employing CorNeXt as a CNN model. In this study, cornea topography maps from the Casia2 anterior OCT instrument were used. The used CorNeXt model is based on the ConvNeXt [9] CNN architecture. To employ ConvNeXt for corneal disease classification, modifications to the architecture were implemented. Measurements of axial refractive power, as well as the elevation of the cornea's front and back surfaces and its thickness were taken from the scan for every individual cornea and five related maps were created and displayed as grayscale images. ConvNeXt was adapted to include all cornea data by stacking these maps into a five-channel pseudo-image. The dataset included a total of 2182 scans (1552 scans for training, 388 scans for validation and 242 scans for test). The model achieved a sensitivity of 98.46% and a specificity of 91.96% in distinguishing healthy from pathological corneas. For the labeled class of keratoconus, it reached 92.56% accuracy, 84.07% sensitivity, 100% specificity and a 91.34% F1 score.

Materials and methods

Convolutional neural network

Artificial Neural Networks (ANNs) mimic the brain's processing through nodes and weighted connections, learning via adjustable weights during training [10]. CNNs, a specialised form

of ANN, are designed for image data, using convolutional layers with convolution kernels, referred to as filters, to detect features and generate feature maps [11,12]. For this study, three CNN models were selected.

Quality criteria

In this study, Mean Squared Error (MSE) is used as a loss function for the regression task. MSE is a derivable criterion and having a derivable criterion is essential for gradient descent algorithms, which are used universally to adjust weights in neural networks during training. MSE is defined as Eq (1), where N signifies the number of actual values, which is equivalent to the number of predicted values; y_i represents the actual value at position i and \hat{y}_i represents the predicted value at the same position [13].

$$\text{MSE} = \frac{1}{N} \sum_{i=1}^N |y_i - \hat{y}_i|^2 \quad (1)$$

To compare the performance of different prediction models, Mean Absolute Error (MAE) is used, as this measures the average absolute difference between the actual values and the predicted values by the model [11]. Eq (2) illustrates the MAE computation, where N , y_i and \hat{y}_i retain the same meanings as in Eq (1) [13].

$$\text{MAE} = \frac{1}{N} \sum_{i=1}^N |y_i - \hat{y}_i| \quad (2)$$

Key metrics for evaluating a binary classifier are derived from the four entries in the confusion matrix. They are crucial for assessing the classifier's performance. True Positive (TP) signifies the count of correctly classified positive samples, such as images with keratoconus correctly identified as having keratoconus. True Negative (TN) represents the count of correctly classified negative samples, like images without keratoconus correctly identified as not having keratoconus. False Positive (FP) refers to the count of samples that have been incorrectly classified as positive; that is, in our case, images without keratoconus mistakenly identified as having keratoconus. False Negative (FN) indicates the count of samples that have been incorrectly classified as negative, such as images with keratoconus incorrectly identified as not having keratoconus. Fig 1 shows the confusion matrix.

In this study, the metrics below are used to assess how effectively the architectures classify the data into two different categories [14].

Accuracy measures the proportion of correctly classified samples out of the total number of samples in the test dataset. Accuracy is calculated as [14]

$$\text{Accuracy} = \frac{TP + TN}{TP + FP + TN + FN} \quad (3)$$

Sensitivity is the proportion of correctly identified positive samples out of all actual positive samples, calculated as [14]:

$$\text{Sensitivity} = \frac{TP}{TP + FN} \quad (4)$$

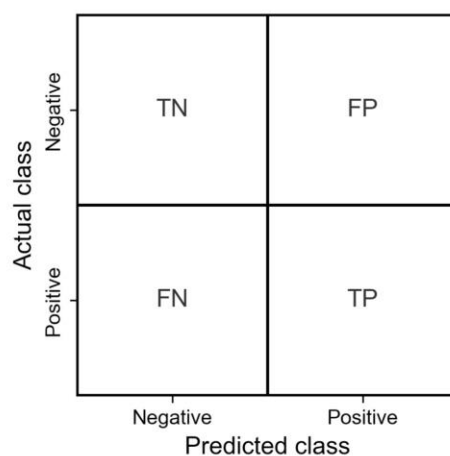


Fig 1. Confusion matrix. Abbreviations: TN = True Negative, FP = False Positive, FN = False Negative, TP = True Positive.

<https://doi.org/10.1371/journal.pone.0311036.g001>

Specificity measures the proportion of correctly classified negative samples out of all samples classified as negative [14]:

$$\text{Specificity} = \frac{TN}{TN + FP} \quad (5)$$

PPV is defined as the proportion of correctly classified samples relative to all samples predicted to belong to the positive class [14]:

$$\text{PPV} = \frac{TP}{TP + FP} \quad (6)$$

As we are using a threshold on the estimated ESI, a high sensitivity or specificity can be trivially achieved at the cost of a useless low value of the respective other metric. The F1-score finds a balance between these two metrics. The F1 score is defined as [14]:

$$\text{F1} = 2 \times \frac{\text{PPV} \times \text{Sensitivity}}{\text{PPV} + \text{Sensitivity}} \quad (7)$$

Furthermore, the F1 score has an advantage when dealing with imbalanced datasets, where one class significantly outnumbers the other. In such cases, metrics like accuracy, sensitivity and specificity may not effectively measure how well the model distinguishes between classes. Therefore, the F1 score can be used because it provides a more balanced evaluation of the model's performance.

The Receiver Operating Characteristic (ROC) curve was analysed to find the best trade-off between sensitivity and specificity for predictions by identifying the optimal threshold, which is the point that maximises the difference between the true positive rate (sensitivity) and the false positive rate (1-specificity). Following this, the predicted ESI values were classified into positive and negative classes based on the optimal threshold to compute the confusion

matrix values. The predicted ESI values that are equal to or exceed the threshold are considered as *Keratoconus* which indicate the presence of ectasia and those below the threshold are categorised as *Not Keratoconus* which indicate suspicion of ectasia or no ectasia pattern.

Data

In this study, the data were obtained from patients examined at the eye clinic of the Homburg University Hospital, between February 01, 2021 and September 01, 2023. The data were anonymised at the source and were transferred to us for further processing on October 02, 2023. We were freed from the requirement for ethics approval for the data by the ethics committee of the Saarland medical council (registration number 157/21). Age and sex were not considered important. The instrument, Cornea/Anterior Segment OCT Casia2 from Tomey Corporation, made in Japan, was used for data acquisition from patients. This instrument uses optical coherence tomography with a 1310 nm wavelength laser to measure different parameters, such as corneal thickness, the depth from the anterior surface of the cornea to the anterior surface of the crystalline lens and the depth from the posterior surface of the cornea to the anterior surface of the crystalline lens. The scan range is 13 mm in depth and 16 mm in diameter. The Casia2 instrument has two modes available: 'Anterior Segment mode' and 'Lens mode'. In Anterior Segment mode, high-sensitivity measurements of the cornea, angle and intraocular lens can be performed, but it does not allow visualisation of the posterior lens. Lens mode provides a simultaneous view of the entire area from the cornea to the posterior lens. Since in this study the visualisation of the posterior lens is not important for the detection of keratoconus, the Anterior Segment mode was selected. The Casia2 instrument produces raw data after measurement, which is in the format of 3dv. Each 3dv file related to the corneal map is 36.6 MB in size. For each 3dv file there is an xpf file that contains meta-data about the measurement, including the examined eye (left or right), date and time of the examination and the exam protocol name. For each measurement, the ESI is stored in a csv file, which can be exported from the Casia2 instrument's software. Ectasia screening identifies keratoconus by independently analysing the shapes of the anterior and posterior cornea. The final diagnosis is based on the results from both assessments. For the anterior cornea, the evaluation focuses on spherical, asymmetry and regular astigmatism components of Fourier analysis. For the posterior cornea, the evaluation focuses on the steepest point of instantaneous power, as well as the asymmetry, regular and higher-order irregular astigmatism components of Fourier analysis. If the analysis area is insufficient for either cornea, the result for that cornea will be marked as 'N/A'. The final diagnosis is determined by the higher score from either assessment; if both are 'N/A', the final result will also be 'N/A'. If the ESI result ranges from 0 to 4, no ectasia pattern is detected. If the ESI result is between 5 and 29 suggests a suspicion of ectasia and a result between 30 and 95 indicates clinical ectasia.

We used a Python [15] script to extract 16 images from raw data (3dv file) which originally were stored in a 16-bit unsigned integer format. Each image, with a resolution of 800 pixels in width and 1464 pixels in height, was then saved as a grayscale PNG file. Fig 2 shows a series of 16 resized images of a left eye with an ESI of 0, where the height has been reduced to one-third of the original dimension by using a Python script to better represent the realistic shape of the eye. The image preprocessing involved cropping 25% from the left side of the images and 25% from the right side of the images to exclude unnecessary eyelid areas and 60% from the bottom of the images to remove regions that did not cover the cornea. After that, the images were resized to a dimension of 224×224 pixels.

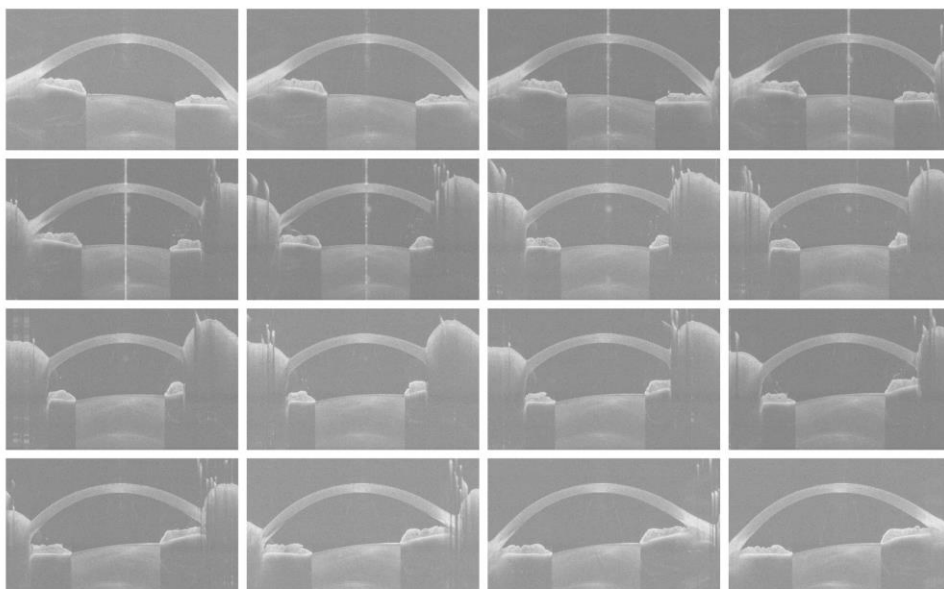


Fig 2. Resized images of a left eye with an ESI of 0. Abbreviation: ESI = Ectasia Screening Index.

<https://doi.org/10.1371/journal.pone.0311036.g002>

Experimental design and implementation

Since CNNs are suited for detecting objects within images [12], three models (ResNet18, DenseNet121 and EfficientNetB0) were selected based on their performance in the field. ResNet was examined on ImageNet and CIFAR-10 [16], DenseNet was tested on CIFAR-10, CIFAR-100, SVHN and ImageNet [17] and EfficientNet was evaluated on ImageNet and transfer learning datasets, including CIFAR-10, CIFAR-100, Birdsnap, Stanford Cars, Flowers, FGVC Aircraft, Oxford-IIIT Pets and Food-101 [18].

ResNet18 is a variant of the residual network architecture. In residual networks, short-cut connections are used to bypass one or more layers and implement identity mapping which allow their outputs to be summed with the outputs of the intermediate layers [16]. DenseNet121 belongs to the dense convolutional network series. In this type of neural networks, all layers are connected directly with each other which allow them to receive additional inputs from preceding layers and propagate their feature maps to subsequent layers. Unlike residual networks, features are concatenated rather than summed before being forwarded to the subsequent layer [17]. EfficientNetB0 is part of the EfficientNet series. In EfficientNet, the depth, width and resolution of the network are uniformly scaled by a specific set of scaling coefficients [18].

All CNN models were trained from scratch using Python and the PyTorch library [19] on a system equipped with an 11th Gen Intel(R) Core(TM) i7-11700@2.5 GHz processor, 32 GB of RAM and a 64-bit operating system with an x64-based processor. The input images were 16-channel, whereas standard pretrained models are designed for 3-channel

Red-Green-Blue input. Although it is technically possible to adapt pretrained networks to accept multi-channel inputs, for example by averaging pretrained weights across channels, such modifications introduce complexity and may reduce the benefit of transfer learning, especially when the additional channels contain modality-specific information not represented in natural images. Therefore, all architectures were trained from scratch. The training proceeded for 100 epochs, during which the validation MSE became stable. The data were divided into disjoint training, validation and test datasets to ensure that the architectures were trained on one subset, evaluated on another to detect overfitting (where the architecture fails to apply its learned patterns from training data to unseen data [20]) and finally tested on a separate unseen subset to assess their ability to perform on new data. The batch sizes for the training, validation and test sets were set to 64. From a total of 15457 3dv files, 5817 were selected for training, validation and testing. The files not chosen were excluded due to defects on the cornea, such as keratoplasty. During the training phase, 3689 scans (stored as 3dv file) were used. This represents approximately 63.42% of the total dataset. Similarly, the validation phase involved 1050 scans (accounting for around 18.05% of the total) and the testing phase consisted of 1078 scans (accounting for around 18.53% of the total).

Table 1 presents the distribution of 3dv files which were used for training, validation and testing. The dataset is categorised based on the ESI, with a threshold of 30, as determined by the Casia2 instrument. An ESI of 30 or greater indicates the *Keratoconus* class, which signifies clinical ectasia.

An ESI below 30 classifies the files as *Not Keratoconus* class, indicating either a suspicion of ectasia or no ectasia pattern detected.

Every set of 16 images from a single 3dv file was stacked together. These stacked images were fed into the architectures, with the first convolutional layer modified to accept a 16-channel input. The fully connected layer for the output was also modified to produce a single output. Additionally, an extra fully connected layer was included to process the combined features which integrates one feature from the architecture and two features representing the eye parameters (right eye and left eye). This formed a combined feature vector of dimension three, which was passed through a final linear layer to yield the predicted ESI. Each ESI value was used as the label for a set of 16 stacked images in the adapted CNN models. For the training process, MSE was used as the loss function to minimise prediction errors. Adam is a favoured optimiser for training deep neural networks due to its quicker convergence compared to stochastic gradient descent [21]. Based on [21], AdamW converges faster and generalises better than Adam. In the experiments, the model parameters were optimised using the AdamW optimiser with a learning rate of 0.01 and a weight decay of 0.05. Moreover, a scheduler was implemented to adjust the learning rate on a plateau, with a reduction factor of 0.1 and a patience of 10 epochs.

Fig 3 illustrates the workflow for predicting the ESI by using the adapted CNN models.

Table 1. Dataset distribution of 3dv files and classes.

Dataset	Total	<i>Keratoconus</i> class	<i>Not Keratoconus</i> class
Train	3689	1486 (40%)	2203 (60%)
Validation	1050	405 (39%)	645 (61%)
Test	1078	429 (40%)	649 (60%)

<https://doi.org/10.1371/journal.pone.0311036.t001>

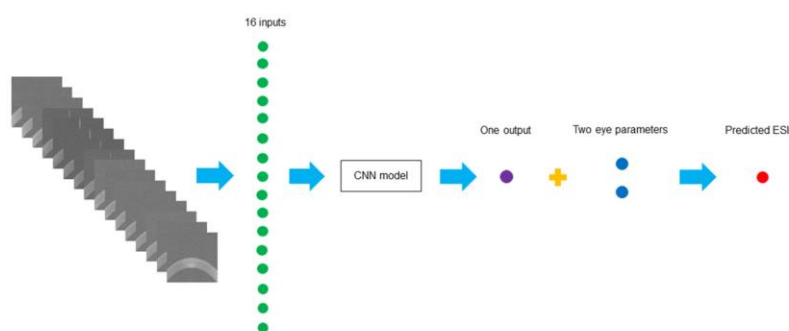


Fig 3. Workflow diagram for predicting the ESI. Abbreviations: ESI = Ectasia Screening Index, CNN = Convolutional Neural Network.

<https://doi.org/10.1371/journal.pone.0311036.g003>

Results and discussion

Table 2 presents the MAE and MSE values, rounded to two decimal places, derived from the evaluation of the adapted ResNet18, the adapted DenseNet121 and the adapted EfficientNetB0 on the test dataset.

Fig 4 shows Kernel Density Estimates (KDEs) of errors between the predicted ESIs and the actual ESIs for the adapted ResNet18, the adapted DenseNet121 and the adapted EfficientNetB0. These KDE plots represent the distribution of errors, where the error is determined by subtracting the actual ESI from the predicted ESI.

Table 3 provides a summary of the frequency of errors within specified error ranges for the adapted CNN models.

Fig 5 illustrates the correlation between the actual ESIs and the architecture predictions for the adapted ResNet18, the adapted DenseNet121 and the adapted EfficientNetB0, respectively.

Fig 6 shows the confusion matrices for each of the CNN architectures tested.

Fig 7 illustrates the ROC curves for the three adapted CNN models. The ROC curve analysis is based on the predicted ESI values. The optimal classification thresholds, determined using Youden's Index and rounded to two decimal places, were 33.23 for the adapted ResNet18, 30.61 for the adapted DenseNet121 and 32.12 for the adapted EfficientNetB0. These values correspond to the points on each curve that maximise the trade-off between sensitivity and specificity.

Table 4 presents a comparison of classification performance metrics for the adapted ResNet18, the adapted DenseNet121 and the adapted EfficientNetB0 (rounded to four decimal places) with three models of CorNet [5], KerNet [6] and CorNeXt [8] on the test set.

Table 2. Test set MAE and MSE performance of the adapted CNN models. Abbreviations: MAE = Mean Absolute Error, MSE = Mean Squared Error, CNN = Convolutional Neural Network.

CNN architecture	MAE	MSE
adapted ResNet18	7.15	122.04
adapted DenseNet121	6.64	110.33
adapted EfficientNetB0	5.86	101.05

<https://doi.org/10.1371/journal.pone.0311036.t002>

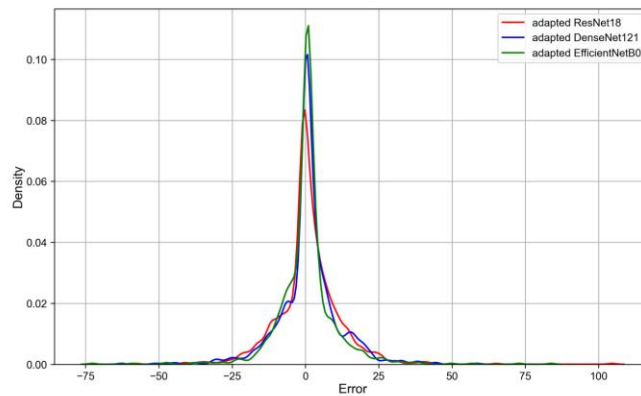


Fig 4. KDEs of errors between the predicted ESIs and the actual ESIs for the different CNN architectures.
Abbreviations: KDE = Kernel Density Estimate, ESI = Ectasia Screening Index, CNN = Convolutional Neural Network.

<https://doi.org/10.1371/journal.pone.0311036.g004>

Table 3. Frequency of errors for CNN architectures within specified ranges. *Abbreviation:* CNN = Convolutional Neural Network.

CNN architecture	Error range							
	below -10	-10 to -5	-5 to -2	-2 to 0	0 to 2	2 to 5	5 to 10	above 10
adapted ResNet18	124	87	74	232	133	134	134	160
adapted DenseNet121	107	100	62	142	267	138	121	141
adapted EfficientNetB0	86	113	89	147	298	149	86	110

<https://doi.org/10.1371/journal.pone.0311036.t003>

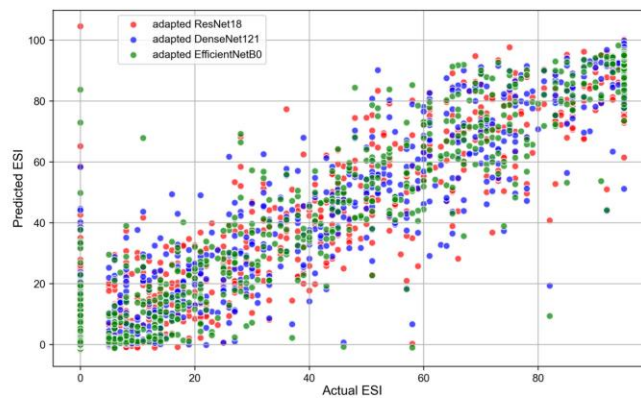


Fig 5. Correlation between the actual ESIs and the architecture predictions for the different CNN architectures.
Abbreviations: ESI = Ectasia Screening Index, CNN = Convolutional Neural Network.

<https://doi.org/10.1371/journal.pone.0311036.g005>

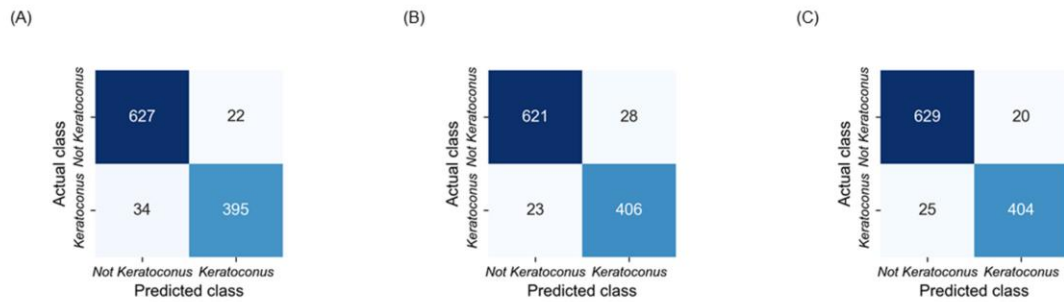


Fig 6. Confusion matrices of CNN architectures. (A) adapted ResNet18. (B) adapted DenseNet121. (C) adapted EfficientNetB0. Abbreviation: CNN = Convolutional Neural Network.

<https://doi.org/10.1371/journal.pone.0311036.g006>

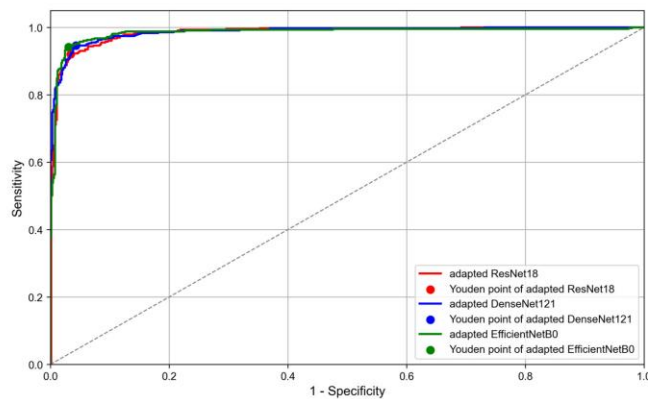


Fig 7. ROC curves for the three CNN architectures. Abbreviations: ROC = Receiver Operating Characteristic, CNN = Convolutional Neural Network.

<https://doi.org/10.1371/journal.pone.0311036.g007>

Table 4. Evaluation metrics for CNN architectures. Abbreviations: CNN = Convolutional Neural Network, PPV = Positive Predictive Value.

CNN architecture	Metrics				
	Accuracy	Sensitivity	Specificity	PPV	F1 Score
adapted ResNet18	0.9480	0.9207	0.9661	0.9472	0.9338
adapted DenseNet121	0.9527	0.9464	0.9569	0.9355	0.9409
adapted EfficientNetB0	0.9583	0.9417	0.9692	0.9528	0.9472
CorNet [5]	0.9213	0.9249	0.9154	0.9477	0.9362
KerNet [6]	0.9474	0.9371	None	0.9410	0.9389
CorNeXt [8]	0.9256	0.8407	1	None	0.9134

<https://doi.org/10.1371/journal.pone.0311036.t004>

This study explored the use of three CNN architectures (adapted ResNet18, adapted DenseNet121 and adapted EfficientNetB0) for predicting the ESI by using raw data from the Casia2 instrument.

Based on the performance metrics presented in the [Table 2](#), the adapted EfficientNetB0 showed the best performance in predicting the ESIs on the test dataset. According to [Fig 4](#), the peak around 0 indicates that most predictions from all three architectures (the adapted ResNet18, the adapted DenseNet121, and the adapted EfficientNetB0) are very close to the actual ESI values. Also, the plots are centered around zero, which indicates that the errors are symmetrically distributed on either side of the zero error line. Moreover, the adapted EfficientNetB0 model has the highest peak, which indicates that it has the highest proportion of predictions with smaller errors compared to the other two architectures. Additionally, all architectures show very low densities of extreme errors (far from zero) which is consistent with [Fig 5](#). According to [Table 4](#), the adapted EfficientNetB0 achieved higher accuracy and F1 score in distinguishing between *Keratoconus* and *Not Keratoconus* classes compared to the two other adapted CNN models and the CorNet, KerNet and CorNeXt models. The higher accuracy and F1 score rates observed for the adapted EfficientNetB0 emphasises the potential of this CNN architecture in distinguishing between *Keratoconus* and *Not Keratoconus* classes based on the raw data from the Casia2 instrument.

Future research could explore the applicability of other CNN models beyond the ones evaluated in this study to further enhance performance metrics.

Conclusions

To the best of our knowledge, this study is the first to use raw OCT data from the Casia2 instrument to predict the ESI. In conclusion, the adapted EfficientNetB0 outperformed the adapted ResNet18, the adapted DenseNet121 and the models in state-of-the-art studies in distinguishing between *Keratoconus* and *Not Keratoconus* classes. This highlights the effectiveness of this CNN architecture in improving diagnostic accuracy and F1 score based on raw data from the Casia2 instrument and suggests its significant potential for enhancing ophthalmological evaluations.

Author contributions

Conceptualization: Maziar Mirsalehi.

Data curation: Maziar Mirsalehi, Benjamin Fassbind.

Formal analysis: Maziar Mirsalehi.

Funding acquisition: Achim Langenbacher.

Investigation: Maziar Mirsalehi.

Methodology: Maziar Mirsalehi.

Project administration: Achim Langenbacher.

Software: Maziar Mirsalehi, Benjamin Fassbind.

Supervision: Andreas Streich, Achim Langenbacher.

Validation: Maziar Mirsalehi.

Visualization: Maziar Mirsalehi.

Writing – original draft: Maziar Mirsalehi.

Writing – review & editing: Benjamin Fassbind, Andreas Streich, Achim Langenbacher.

References

1. Santodomingo-Rubido J, Carracedo G, Suzuki A, Villa-Collar C, Vincent SJ, Wolffsohn JS. Keratoconus: An updated review. *Cont Lens Anterior Eye*. 2022;45(3):101559. <https://doi.org/10.1016/j.clae.2021.101559> PMID: 34991971
2. Rabinowitz YS. Keratoconus. *Surv Ophthalmol*. 1998;42(4):297–319. [https://doi.org/10.1016/s0039-6257\(97\)00119-7](https://doi.org/10.1016/s0039-6257(97)00119-7) PMID: 9493273
3. Fan R, Chan TC, Prakash G, Jhanji V. Applications of corneal topography and tomography: A review. *Clin Exp Ophthalmol*. 2018;46(2):133–46. <https://doi.org/10.1111/ceo.13136> PMID: 29266624
4. Almodin E, Nassaralla BA, Sandes J. Keratoconus: A comprehensive guide to diagnosis and treatment. Springer Nature; 2022.
5. Zhang P, Yang L, Mao Y, Zhang X, Cheng J, Miao Y, et al. CorNet: Autonomous feature learning in raw Corvis ST data for keratoconus diagnosis via residual CNN approach. *Comput Biol Med*. 2024;172:108286. <https://doi.org/10.1016/j.compbiomed.2024.108286> PMID: 38493602
6. Feng R, Xu Z, Zheng X, Hu H, Jin X, Chen DZ, et al. KerNet: A novel deep learning approach for keratoconus and sub-clinical keratoconus detection based on raw data of the pentacam HR system. *IEEE J Biomed Health Inform*. 2021;25(10):3898–910. <https://doi.org/10.1109/JBHI.2021.3079430> PMID: 33979295
7. Schatteburg J, Langenbucher A. Protocol for the diagnosis of keratoconus using convolutional neural networks. *PLoS One*. 2022;17(2):e0264219. <https://doi.org/10.1371/journal.pone.0264219> PMID: 35180279
8. Fassbind B, Langenbucher A, Streich A. Automated cornea diagnosis using deep convolutional neural networks based on cornea topography maps. *Sci Rep*. 2023;13(1):6566. <https://doi.org/10.1038/s41598-023-33793-w> PMID: 37085580
9. Liu Z, Mao H, Wu CY, Feichtenhofer C, Darrell T, Xie S. A ConvNet for the 2020s. In *Proceedings of the IEEE/CVF conference on computer vision and pattern recognition*; 2022. p. 11976–86.
10. Grossi E, Buscema M. Introduction to artificial neural networks. *Eur J Gastroenterol Hepatol*. 2007;19(12):1046–54. <https://doi.org/10.1097/MEG.0b013e3282f198a0> PMID: 17998827
11. Li Z, Liu F, Yang W, Peng S, Zhou J. A survey of convolutional neural networks: Analysis, applications, and prospects. *IEEE Trans Neural Netw Learning Syst*. 2022;33(12):6999–7019. <https://doi.org/10.1109/tnnls.2021.3084827>
12. Taye MM. Theoretical understanding of convolutional neural network: Concepts, architectures, applications, future directions. *Computation*. 2023;11(3):52. <https://doi.org/10.3390/computation11030052>
13. Qi J, Du J, Siniscalchi SM, Ma X, Lee C-H. On mean absolute error for deep neural network based vector-to-vector regression. *IEEE Signal Process Lett*. 2020;27:1485–9. <https://doi.org/10.1109/lsp.2020.3016837>
14. Hicks SA, Strümke I, Thambawita V, Hammou M, Riegler MA, Halvorsen P, et al. On evaluation metrics for medical applications of artificial intelligence. *Sci Rep*. 2022;12(1):5979. <https://doi.org/10.1038/s41598-022-09954-8> PMID: 35395867
15. Python W. Python releases for windows; 2021. p. 24.
16. He K, Zhang X, Ren S, Sun J. Deep residual learning for image recognition. In: 2016 IEEE conference on computer vision and pattern recognition (CVPR); 2016. p. 770–8. <https://doi.org/10.1109/cvpr.2016.90>
17. Huang G, Liu Z, Van Der Maaten L, Weinberger KQ. Densely connected convolutional networks. In: *Proceedings of the IEEE conference on computer vision and pattern recognition*; 2017. p. 4700–8.
18. Tan M, Le Q. Efficientnet: Rethinking model scaling for convolutional neural networks. In: *International conference on machine learning*; 2019. p. 6105–14.
19. Paszke A, Gross S, Massa F, Lerer A, Bradbury J, Chanan G, Killeen T, Lin Z, Gimelshein N, Antiga L, Desmaison A. Pytorch: An imperative style, high-performance deep learning library. *Advances in neural information processing systems*; 2019. p. 32.
20. Ying X. An overview of overfitting and its solutions. *J Phys: Conf Ser*. 2019;1168:022022. <https://doi.org/10.1088/1742-6596/1168/2/022022>
21. Zhou P, Xie X, Lin Z, Yan S. Towards understanding convergence and generalization of AdamW. *IEEE Trans Pattern Anal Mach Intell*. 2024;46(9):6486–93. <https://doi.org/10.1109/TPAMI.2024.3382294> PMID: 38536692

CORRECTION

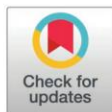
Correction: Prediction of the ectasia screening index from raw Casia2 volume data for keratoconus identification by using convolutional neural networks

Maziar Mirsalehi, Benjamin Fassbind, Andreas Streich, Achim Langenbucher

The Data Availability statement for this article is incorrect. The correct statement is: The dataset and codes have been uploaded to a repository. The DOI is: <https://doi.org/10.5281/zenodo.16884052>.

Reference

1. Mirsalehi M, Fassbind B, Streich A, Langenbucher A. Prediction of the ectasia screening index from raw Casia2 volume data for keratoconus identification by using convolutional neural networks. PLoS One. 2025;20(9):e0311036. <https://doi.org/10.1371/journal.pone.0311036> PMID: 40892937



OPEN ACCESS

Citation: Mirsalehi M, Fassbind B, Streich A, Langenbucher A (2025) Correction: Prediction of the ectasia screening index from raw Casia2 volume data for keratoconus identification by using convolutional neural networks. PLoS One 20(12): e0338609. <https://doi.org/10.1371/journal.pone.0338609>

Published: December 9, 2025

Copyright: © 2025 Mirsalehi et al. This is an open access article distributed under the terms of the [Creative Commons Attribution License](https://creativecommons.org/licenses/by/4.0/), which permits unrestricted use, distribution, and reproduction in any medium, provided the original author and source are credited.

4.2 Article 2

This article focuses on predicting the corneal condition from raw OCT data obtained from the cornea/anterior segment OCT Casia2 by using modified DenseNet121, EfficientNet-B0, MobileNetV3-Large, and ResNet18 as CNN models. Three experienced ophthalmologists (PD Dr. Alaa Din Abdin, PD Dr. Elias Flockerzi, and Univ.-Prof. Dr. Nora Szentmary) assigned 2737 eye examination to one of three classes: ‘normal’, representing a normal eye; ‘ectasia’, representing corneal ectasia; or ‘other disease’, including eyes with corneal dystrophies, penetrating keratoplasty, pterygium, Salzmann’s nodules, or subepithelial or stromal scarring [76].

Article

Deep Learning-Based Diagnosis of Corneal Condition by Using Raw Optical Coherence Tomography Data

Maziar Mirsalehi ^{1,*}, Michael Schwemm ¹, Elias Flockerzi ², Nóra Szentmáry ¹, Alaa Din Abdin ², Berthold Seitz ² and Achim Langenbucher ¹

¹ Department of Experimental Ophthalmology, Saarland University, Kirrberger Street 100, 66424 Homburg, Saarland, Germany

² Department of Ophthalmology, Saarland University Medical Centre UKS, Kirrberger Street 100, 66424 Homburg, Saarland, Germany

* Correspondence: maziar.mirsalehi@uni-saarland.de

Abstract

Background/Objectives: Keratoconus (KC) is the most common corneal ectasia. This condition affects quality of vision, especially when it is progressive, and a timely and stage-related treatment is mandatory. Therefore, early diagnosis is crucial to preserve visual acuity. Medical data may be used either in their raw state or in a preprocessed form. Software modifications introduced through updates may potentially affect outcomes. Unlike preprocessed data, raw data preserve their original format across software versions and provide a more consistent basis for clinical analysis. The objective of this study was to distinguish between healthy and KC corneas from raw optical coherence tomography data by using a convolutional neural network. **Methods:** In total, 2737 eye examinations acquired with the Casia2 anterior-segment optical coherence tomography (Tomey, Nagoya, Japan) were decided by three experienced ophthalmologists to belong to one of three classes: ‘normal’, ‘ectasia’, or ‘other disease’. Each eye examination consisted of sixteen meridional slice images. The dataset included 744 examinations. DenseNet121, EfficientNet-B0, MobileNetV3-Large and ResNet18 were modified for use as convolutional neural networks for prediction. All reported metric values were rounded to four decimal places. **Results:** The overall accuracy for the modified DenseNet121, modified EfficientNet-B0, modified MobileNetV3-Large and modified ResNet18 is 91.27%, 91.27%, 92.86% and 89.68%, respectively. The macro-averaged sensitivity, macro-averaged specificity, macro-averaged Positive Predictive Value and macro-averaged F1 score for the modified DenseNet121, modified EfficientNet-B0, modified MobileNetV3-Large and modified ResNet18 are reported as 91.27%, 91.27%, 92.86% and 89.68%; 95.63%, 95.63%, 96.43% and 94.84%; 91.58% 91.65%, 92.91% and 90.24%; and 91.35%, 91.29%, 92.85% and 89.81%, respectively. **Conclusions:** The successful use of a convolutional neural network with raw optical coherence tomography data demonstrates the potential of raw data to be used instead of preprocessed data for diagnosing KC in ophthalmology.

Keywords: CNN; cornea; deep learning; ectasia; eye; GUI; keratoconus; OCT; raw data; vision

1. Introduction

Sight is an important ability for human beings, and quality of life can be affected by eye problems. Human eyes contain tissues and structures such as the cornea, lens, retina



Academic Editor: Jae-Ho Han

Received: 25 October 2025

Revised: 1 December 2025

Accepted: 3 December 2025

Published: 8 December 2025

Citation: Mirsalehi, M.; Schwemm, M.; Flockerzi, E.; Szentmáry, N.; Abdin, A.D.; Seitz, B.; Langenbucher, A. Deep Learning-Based Diagnosis of Corneal Condition by Using Raw Optical Coherence Tomography Data. *Diagnostics* **2025**, *15*, 3115. <https://doi.org/10.3390/diagnostics15243115>

Correction Statement: This article has been republished with a minor change. The change does not affect the scientific content of the article and further details are available within the backmatter of the website version of this article.

Copyright: © 2025 by the authors. Licensee MDPI, Basel, Switzerland. This article is an open access article distributed under the terms and conditions of the Creative Commons Attribution (CC BY) license (<https://creativecommons.org/licenses/by/4.0/>).

and optic nerve. The cornea covers the outer surface of the eyeball. Corneal conditions commonly include refractive errors such as myopia, hyperopia and astigmatism, as well as keratoconus (KC) and inflammation [1].

KC, as a quasi-inflammatory disease, is a bilateral condition that causes progressive thinning and steepening of the cornea and affects between 50 and 230 individuals per 100,000 [2,3]. Diagnosis of this disease typically occurs in the second or third decade of life. Eye rubbing is regarded as a major risk factor in the KC development [4]. Early KC can be detected using various diagnostic methods [5], including handheld keratoscopes (Placido disks) [6], slit-lamp biomicroscopy [7] and ultrasonic pachymetry [8], as well as corneal topography [9] and tomography techniques [10] such as Scheimpflug imaging [6] and anterior-segment Optical Coherence Tomography (OCT) [11]. OCT employs low-coherence interferometry with near-infrared light to generate high-resolution images of tissue morphology, including corneal layer-thickness maps [12].

Artificial intelligence (AI) has become increasingly valuable in ophthalmology, particularly for image analysis. Since the 1970s, its application in diagnosing eye diseases has grown substantially. Applications of artificial intelligence are being explored in the diagnosis and management of glaucoma, KC, cataracts and other anterior segment diseases [13]. There has been a growing volume of research assessing the implementation of AI-based methods for diagnosing anterior segment diseases, with particular emphasis on KC detection through anterior-segment OCT imaging [14]. Using AI to detect KC dates back to the earliest study by Maeda et al. [15] in 1994. Several deep learning approaches have been proposed in recent years for KC detection and the classification of the cornea through various corneal imaging techniques [16–21].

In this study, raw OCT data obtained from the Casia2 (Tomey, Nagoya, Japan) were used to diagnose the condition of the cornea. Data can generally be used in their original format or in a preprocessed form, which bears the risk of changes with software updates. In contrast to preprocessed data, raw data grabbed by the instrument typically remain unchanged with new software tools and updates, and potentially offer a more reliable foundation for analysis. The objective of this study is to use raw OCT data to diagnose corneal conditions and to develop a method for automatically distinguishing healthy corneas from KC and other conditions, using data labelled by three experienced ophthalmologists (PD Dr. Alaa Din Abdin, PD Dr. Elias Flockerzi and Univ.-Prof. Dr. Nóra Szentmáry).

2. Materials and Methods

2.1. Data

Patient data were collected at the Department of Ophthalmology, Saarland University Medical Centre, Homburg, Germany, using the cornea/anterior-segment optical coherence tomography device Casia2 (Tomey, Nagoya, Japan) [22], a swept-source OCT-based device that captures anterior segment images of the eye. The Casia2 generates raw data in 3dv format, with each file linked to a corneal map. Each 3dv file contains information for sixteen equi-angular meridional images. The images were stored in sixteen-bit unsigned integer format, with pixel values ranging from 0 to 65,535. Figure 1 shows information from a raw data file of the Casia2.

[[21921 21192 22633 ... 20013 22933 22006]]	[[18940 21607 20113 ... 21528 21788 18504]]	[[20552 24271 22668 ... 18336 21444 22130]]	[[22159 22541 19216 ... 22992 20004 20141]]
[22572 20962 21910 ... 21382 17792 20625]	[21955 21603 12128 ... 23074 22440 18976]	[21421 23992 22109 ... 16914 22879 22859]	[21349 20258 21148 ... 22912 17940 22246]
[21118 20652 20811 ... 21996 19096 20088]	[20873 21968 20391 ... 24197 21972 19191]	[21214 22238 22113 ... 18490 21163 20956]	[20618 20194 23429 ... 17843 18921 22802]
...
[18834 17166 19530 ... 21903 20096 19138]	[17301 20973 16561 ... 18738 21055 16377]	[20265 21758 20918 ... 20595 20274 19718]	[21091 21742 19963 ... 21366 22090 22139]
[17910 17389 18664 ... 21219 19509 18244]	[20323 22383 19523 ... 16434 19913 21335]	[15296 23392 20598 ... 18750 19295 20958]	[14121 19561 16450 ... 20313 20411 21525]
[19031 19773 20264 ... 16458 20707 21481]]	[19234 19713 17978 ... 18471 15376 21338]]	[14901 21571 20483 ... 18601 14649 21167]]	[20131 20120 20405 ... 12038 21453 21815]]
...
[[22726 20896 17598 ... 20444 22712 22851]]	[[22105 20014 21047 ... 18607 22655 20969]]	[[20872 20576 21691 ... 20104 23566 21136]]	[[21657 24626 23315 ... 20970 20773 21881]]
[20804 20521 20263 ... 21002 20707 21120]	[22039 20433 22933 ... 21347 17573 19108]	[20580 18873 21834 ... 21460 23953 17863]	[21822 23395 20727 ... 19330 22665 23545]
[20401 22026 22391 ... 21251 22427 21029]	[21749 19770 23928 ... 21014 18763 20393]	[19695 20971 22883 ... 20274 22984 17875]	[22429 20335 18138 ... 17926 21890 22844]
...
[19645 22655 17436 ... 17196 21861 18429]	[21161 16498 20163 ... 15846 19719 17549]	[18486 14397 18028 ... 21948 21726 18307]	[23754 24240 19932 ... 22461 15284 19877]
[22397 18713 18049 ... 19618 20239 20362]	[21738 17887 20999 ... 19382 20359 21287]	[18026 19685 22318 ... 19563 20649 17968]	[21128 22779 18695 ... 20147 21749 21264]
[22020 19972 19553 ... 19569 17315 21472]]	[16521 17306 18495 ... 15489 19909 19830]]	[11393 13115 19673 ... 19406 18823 21081]]	[24063 24490 21229 ... 20110 20676 23532]]
...
[[23104 20847 21830 ... 21884 19955 22610]]	[[19987 21831 22445 ... 22301 16345 21888]]	[[20409 19143 22157 ... 20446 24083 19433]]	[[20835 22145 23403 ... 22135 22815 21211]]
[22762 23300 24425 ... 15954 22232 22961]	[13453 19992 18449 ... 22547 21897 21540]	[20718 23197 20985 ... 19199 23393 19913]	[19886 19552 21835 ... 23463 20550 19176]
[19831 22981 23539 ... 19227 20033 21835]	[21711 21700 21240 ... 22086 23707 23850]	[20045 23857 16483 ... 19899 18558 17976]	[19610 20999 19567 ... 23730 19855 18558]
...
[18039 17801 22688 ... 20827 18991 15708]	[19730 19217 21133 ... 13105 20804 20573]	[19104 18427 19069 ... 17071 22094 19496]	[19866 20336 17638 ... 19987 20520 19278]
[21646 17696 21510 ... 16451 12535 19175]	[19726 17338 20509 ... 17629 21744 19995]	[13203 21024 19813 ... 20580 22384 20312]	[19659 21373 16881 ... 18079 19715 21871]
[17888 18480 17936 ... 20738 18971 20167]]	[22015 19586 19094 ... 8386 20970 21615]]	[14938 21156 17455 ... 18535 20741 16244]]	[21734 22588 19514 ... 15169 21147 21597]]
...
[[23556 17761 18973 ... 16580 22224 15423]]	[[22284 19708 21404 ... 21412 22021 14419]]	[[19101 22405 21029 ... 14991 18741 22507]]	[[22533 24898 19669 ... 19753 21331 16022]]
[19966 16883 21224 ... 21727 22596 19918]	[23323 18896 21300 ... 21371 20418 20662]	[16285 22049 18592 ... 18984 15091 20432]	[22805 23330 23149 ... 21594 23892 19124]
[19871 22345 21794 ... 23484 22943 21717]	[23210 22889 22490 ... 8695 20637 21205]	[19710 22771 18491 ... 20778 21687 22524]	[21562 18215 21635 ... 20764 24497 20840]
...
[19743 19695 22890 ... 21097 20690 18563]	[19207 20193 20706 ... 21675 17128 19704]	[16140 17221 18499 ... 22165 18819 17146]	[19367 19450 22377 ... 18098 19761 16552]
[17945 16701 19817 ... 16875 22464 18036]	[20184 18618 13772 ... 21631 21145 23383]	[21292 20355 17546 ... 22293 18520 19480]	[16859 20756 20356 ... 22290 20387 17875]
[20300 18451 19873 ... 20276 20607 21677]]	[18317 19153 17882 ... 22877 19537 21502]]	[21118 17865 19763 ... 17652 19213 22178]]	[18741 21531 18664 ... 19492 19040 20594]]

Figure 1. Information from a raw data file.

A Python script was developed to extract sixteen images from each 3dv file. Each image, originally sized at 800 pixels wide and 1464 pixels tall, was stored as a greyscale Portable Network Graphics (PNG) file. Figure 2 shows sixteen images extracted from the same raw data file as presented in Figure 1.

A total of 2737 eye examinations, each containing sixteen equi-angular meridional images with the aspect ratio adjusted to 1.629 (width divided by height) to better represent the realistic shape of the eye, were decided by three experienced ophthalmologists (PD Dr. Alaa Din Abdin, PD Dr. Elias Flockerzi and Univ.-Prof. Dr. Nóra Szentmáry) to belong to one of three classes: ‘normal’, which indicates a normal eye; ‘ectasia’, which indicates corneal ectasia; or ‘other disease’, which included eyes with penetrating keratoplasty, subepithelial or stromal scarring, corneal dystrophies, Salzmann’s nodules or pterygium. All three experienced ophthalmologists were in agreement in labelling 1325 eye examinations as ‘normal’, 212 eye examinations as ‘ectasia’ and 266 eye examinations as ‘other disease’. The split was performed at the eye examination level,

based on the sixteen equi-angular meridional images, rather than at the patient level. Since the labelled eye examinations were not balanced, it was decided to reduce the number of 'normal' eye examinations to make the dataset more balanced. All 212 eye examinations categorised as 'ectasia' and all 266 examinations classified as 'other disease' were used, while 266 'normal' eye examinations were randomly selected to achieve a more balanced dataset. It was decided to create a balanced dataset for both the validation and test datasets. To allocate approximately 60% of the dataset for training, 20% for validation and 20% for testing, it was decided to use 42 of the 212 'ectasia'-labelled eye examinations (approximately 20%), for the test dataset and another 42 (approximately 20%) for the validation dataset and the remaining 128 for the training dataset. To create balanced validation and test datasets, it was decided to use 42 'normal'-labelled eye examinations and 42 'other disease'-labelled eye examinations for the validation dataset, another 42 'normal'-labelled and 42 'other disease'-labelled eye examinations for the test dataset, and the remaining 182 'normal'-labelled and 182 'other disease'-labelled eye examinations for training. After randomly shuffling the rows corresponding to the 'normal' class in a CSV file containing the image file names and labels of 212 eye examinations categorised as 'ectasia', 266 eye examinations categorised as 'other disease' and 266 eye examinations categorised as 'normal', the first 182 eye examinations were selected for the training dataset, the next 42 for the validation dataset and the following 42 for the test dataset. The 'ectasia' class was split in a similar manner. After randomly shuffling the rows corresponding to this class in the same CSV file, the first 128 eye examinations were selected for the training dataset, the next 42 for the validation dataset and the following 42 for the test dataset. The 'other disease' class was also split in the same way. After randomly shuffling the rows corresponding to this class in the same CSV file, the first 182 eye examinations were selected for the training dataset, the next 42 for the validation dataset and the following 42 for the test dataset.

Eye examinations for which the labels did not match were excluded from the analysis. The training dataset included 182 eye examinations for the 'normal' class, 128 eye examinations for the 'ectasia' class and 182 eye examinations for the 'other disease' class (approximately 66.13% of the total dataset). The validation dataset included 42 eye examinations for each class (approximately 16.93% of the total dataset), and the test dataset also included 42 eye examinations for each class (approximately 16.93% of the total dataset) to ensure a balanced distribution. Table 1 summarises the label distribution across the training, validation and test datasets.

Table 1. Label distribution across training, validation and test datasets.

Dataset	Normal	Ectasia	Other Disease	Total
Training	182	128	182	492
Validation	42	42	42	126
Test	42	42	42	126

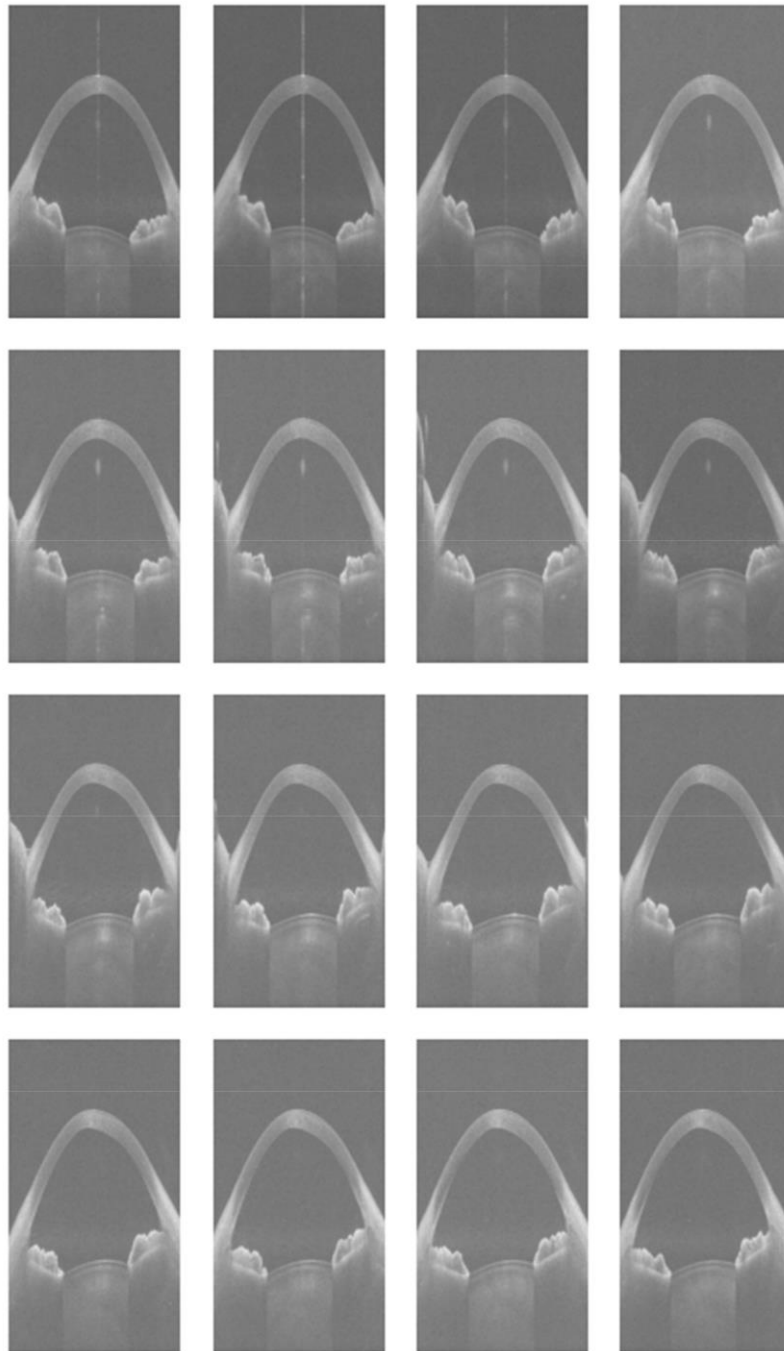


Figure 2. Sixteen equi-angular meridional images extracted from a raw data file.

2.2. Training Architectures

A Convolutional Neural Network (CNN) is a specialised form of artificial neural network structured for image data. It operates by means of convolutional layers that apply kernels, or filters, to detect features and form feature maps [23,24]. In this study, four CNN models from well-established deep learning architectures were selected. DenseNets offer advantages, such as easing the vanishing-gradient problem, strengthening feature propagation and reducing the number of parameters, and they were evaluated on the CIFAR-10, CIFAR-100, ImageNet and SVHN datasets [25]. EfficientNets use a compound scaling method, which can improve accuracy better than other single-dimension scaling methods, and they were evaluated on the Birdsnap, CIFAR-10, CIFAR-100, FGVC Aircraft, Flowers, Food-101, ImageNet, Oxford-IIIT Pets and Stanford Cars datasets [26]. MobileNets can be applied to mobile and embedded vision applications, and they were evaluated on ImageNet dataset [27]. ResNets have residual networks that are easier to optimise, and they were evaluated on the CIFAR-10 and ImageNet datasets [28]. In this study, DenseNet121, EfficientNet-B0, MobileNetV3-Large and ResNet18 were used as the CNN models. The images were resized to 224×224 pixels to match the input dimensions required by the models. The resized images were normalised between -1 and 1 . The models were trained from scratch using Python (version 3.13.5) and the PyTorch library (version 2.7.1) [29]. Training was performed on a system with an Intel(R) Xeon(R) Central Processing Unit (CPU) E5-1650 v2 @ 3.50 GHz 3.50 GHz processor and 32 GB of Random-Access Memory (RAM). The training process consisted of 200 full passes through the dataset. The Python scripts were designed to test the CNN models corresponding to the epoch that achieved the highest validation accuracy among the 200 epochs on the test dataset; if more than one epoch achieved the same highest validation accuracy, the model from the epoch with the highest training accuracy among them was used for evaluation on the test dataset. A batch size of 8 was applied consistently across the training, validation and test sets to ensure stable learning dynamics. To optimise the classification performance, the cross-entropy loss function [30] was selected as the loss metric. The models were optimised using the AdamW optimiser [31]. The initial learning rate was set to 0.01. To adjust the learning rate dynamically during training, a scheduler was employed to reduce the rate by a factor of 0.1 when no improvement occurred over 10 consecutive epochs. Additionally, a weight decay [32] value of 0.05 was applied to regularise the models and reduce the risk of overfitting [33] by constraining the magnitude of the learned parameters.

To accommodate the specific nature of the input data, each group of sixteen resized images was treated as a single volumetric instance and combined into a sixteen-channel input. This stack was then fed into the modified models. To enable the models to process this multi-channel input, the architectures were altered by modifying the first convolutional layer to accept sixteen input channels instead of the standard 3-channel Red–Green–Blue (RGB) format. Furthermore, the classification head of the networks, originally designed for a 1000-class output in ImageNet tasks, was adapted to output three predictions, corresponding to one of the three target classes: ‘normal’, ‘ectasia’ or ‘other disease’. Table 2 shows the differences between the original DenseNet121, EfficientNet-B0, MobileNetV3-Large and ResNet18 models and their modified versions used in this study.

Figure 3 shows the process, from obtaining data from the Casia2 to predicting one of the three classes.

Table 2. Comparison of the original CNN models with their modified versions. Abbreviation: CNN = Convolutional Neural Network.

CNN Model	Number of Input Channels	Number of Output Features
DenseNet121	3	1000
Modified DenseNet121	16	3
EfficientNet-B0	3	1000
Modified EfficientNet-B0	16	3
MobileNetV3-Large	3	1000
Modified MobileNetV3-Large	16	3
ResNet18	3	1000
Modified ResNet18	16	3

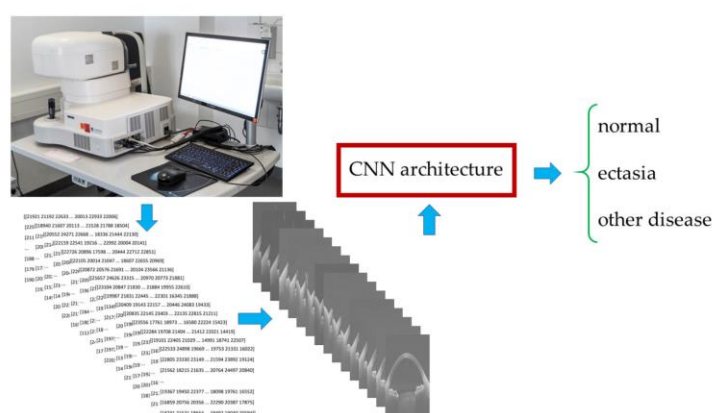


Figure 3. Data acquisition to three-class classification workflow. Abbreviation: CNN = Convolutional Neural Network.

2.3. Evaluation Metrics

For each class, the numbers of True Positives (TPs), False Positives (FPs), True Negatives (TNs) and False Negatives (FNs) were computed using a one-vs.-rest approach. These values were used to derive standard evaluation metrics adapted for multi-class classification, including accuracy, sensitivity, specificity, Positive Predictive Value (PPV) and F1 score. The metrics were calculated according to the definitions provided in [34], with macro-averaging strategies applied where appropriate to ensure fair assessment across all classes. All reported metric values were rounded to four decimal places.

2.4. Gradient-Weighted Class Activation Mapping

Gradient-Weighted Class Activation Mapping (Grad-CAM) [35] was used to visualise the regions of the CNN architectures that are most influential in distinguishing between the three classes: ‘normal’, ‘ectasia’ and ‘other disease’ on the test dataset. The Grad-CAMs for each predicted class were averaged to produce a representative Grad-CAM pattern for that class. The Python scripts were designed to use the model corresponding to the epoch that achieved the highest validation accuracy among the 200 epochs to generate Grad-CAM on the test dataset; if more than one epoch achieved the same highest validation accuracy, the model from the epoch with the highest training accuracy among them was used for

generating Grad-CAM on the test dataset. For each modified CNN model, Grad-CAM was applied to the last convolutional layer.

2.5. Graphical User Interface

A Graphical User Interface (GUI) can help users visualize the prediction results. The GUI was created by using Tkinter (version 8.6), OpenCV (cv2, version 4.12.0), Matplotlib (version 3.10.3), NumPy (version 2.2.6) and Pathlib (Python version 3.13.5). The selected CNN architecture, based on its performance on the test dataset, was implemented by using PyTorch (version 2.7.1). The GUI was developed on the system running Python (version 3.13.5).

3. Results

The training and validation accuracies of the modified CNN models over 200 epochs are shown in Figure 4.

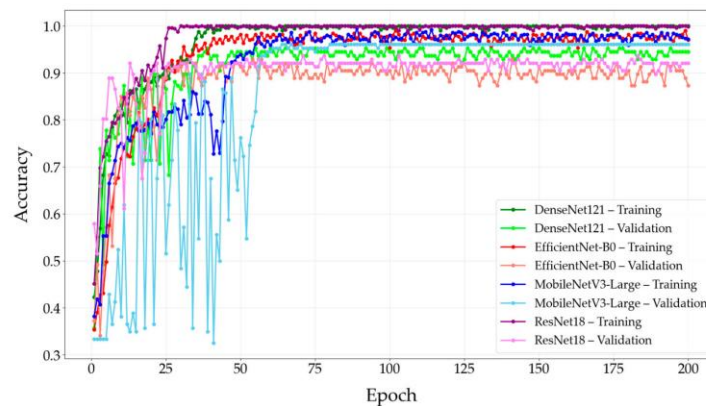


Figure 4. Training and validation accuracies of the modified CNN models over epochs. Abbreviation: CNN = Convolutional Neural Network.

The training and validation losses of the modified CNN models over 200 epochs are shown in Figure 5.

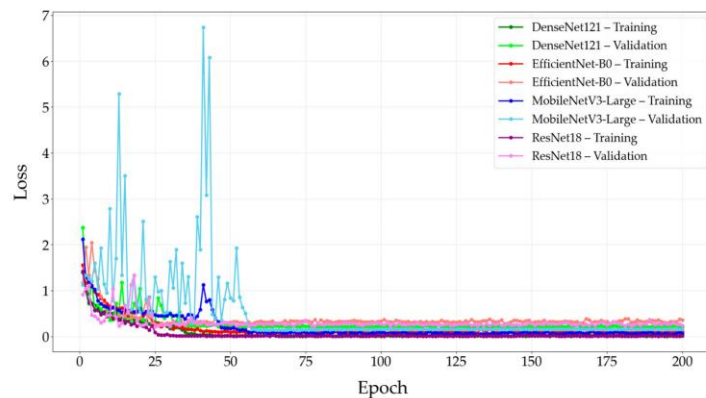


Figure 5. Training and validation losses of the modified CNN models over epochs. Abbreviation: CNN = Convolutional Neural Network.

The distribution of predictions among the classes for the modified CNN models is shown in the confusion matrix in Figure 6.

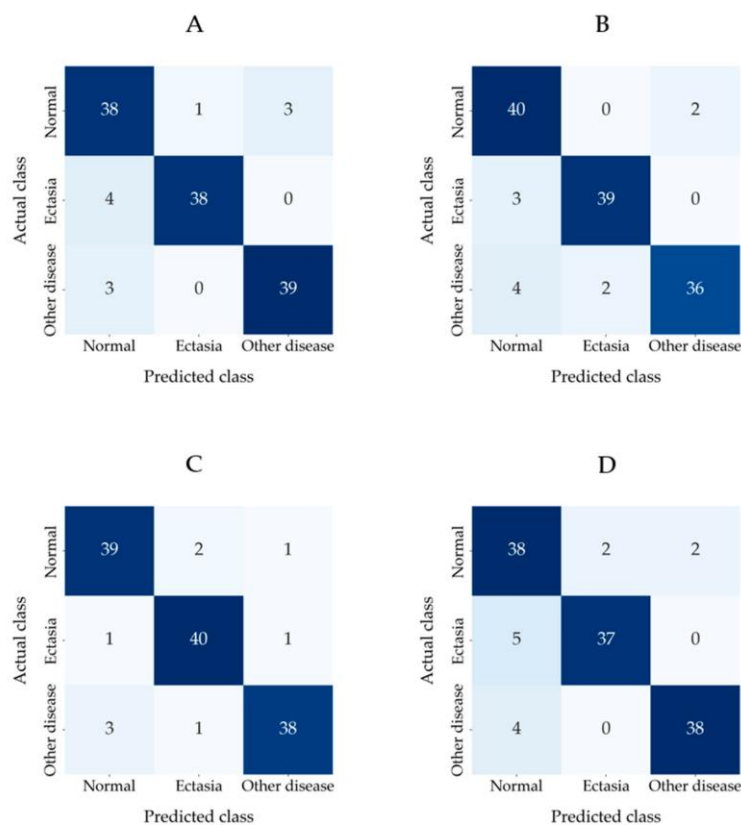


Figure 6. Confusion matrices of the modified CNN models: (A) modified DenseNet121, (B) modified EfficientNet-B0, (C) modified MobileNetV3-Large and (D) modified ResNet18.

Figure 7 shows the averaged Grad-CAM for each predicted class of the modified CNN models in the test dataset. The CNNs' decision importance was colour-coded from blue, for little or no influence, to red, for strong influence on the prediction. Each Grad-CAM for each prediction was overlaid on the average of all sixteen resized extracted images. The averaged Grad-CAM for each class was overlaid on the average of all those averaged images, where the lighter areas represent the averaged background images.

Table 3 shows the performance metrics of the modified DenseNet121, modified EfficientNet-B0, modified MobileNetV3-Large and modified ResNet18 evaluated on the test dataset by using seed number one.

Figure 8 shows the GUI for corneal condition prediction. The GUI has three buttons: 'File', 'Images' and 'Prediction'. The user can select a raw data file in .3dv format by clicking the 'File' button. By clicking the 'Images' button, the user can view the extracted images, which are automatically scaled, as shown in Figure 9. The user can obtain a prediction of the corneal condition and the probabilities of each class, which are rounded to two decimal places, by clicking the 'Prediction' button. Figure 10 shows the prediction output for a raw data file.

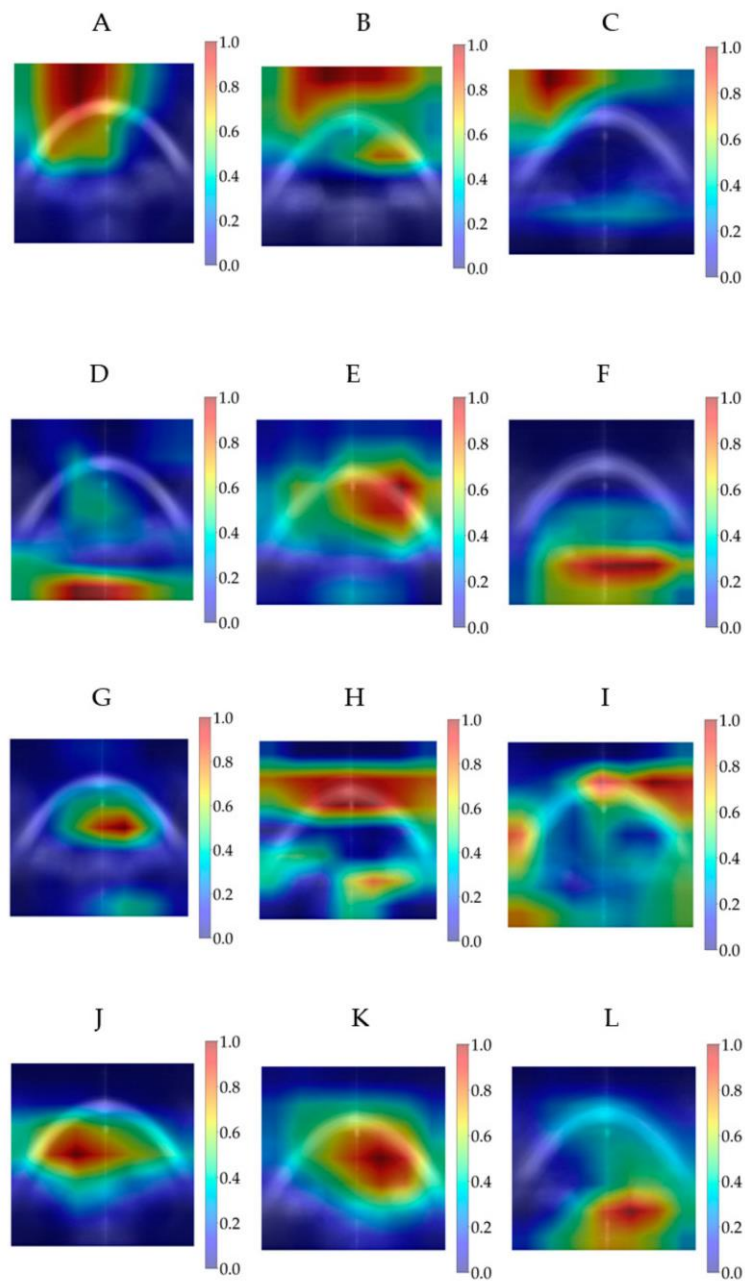
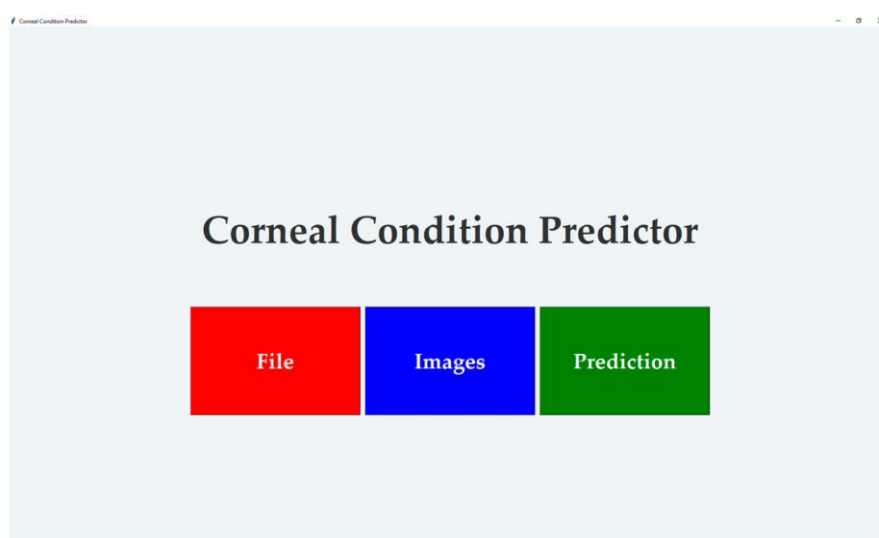


Figure 7. Averaged Grad-CAM for each predicted class in the test dataset for modified DenseNet121, (A) ‘normal’, (B) ‘ectasia’ and (C) ‘other disease’; for modified EfficientNet-B0, (D) ‘normal’, (E) ‘ectasia’ and (F) ‘other disease’; for modified MobileNetV3-Large, (G) ‘normal’, (H) ‘ectasia’ and (I) ‘other disease’; and for modified ResNet18, (J) ‘normal’, (K) ‘ectasia’ and (L) ‘other disease’. Abbreviation: Grad-CAM = Gradient-Weighted Class Activation Mapping.

Table 3. Performance metrics of the modified CNN models evaluated on the test dataset. Abbreviation: PPV = Positive Predictive Value.

Model	Group	Sensitivity	Specificity	PPV	F1 Score	Overall Accuracy
Modified DenseNet121	Normal	0.9048	0.9167	0.8444	0.8736	0.9127
	Ectasia	0.9048	0.9881	0.9744	0.9383	
	Other disease	0.9286	0.9643	0.9286	0.9286	
	Macro-average	0.9127	0.9563	0.9158	0.9135	
Modified EfficientNet-B0	Normal	0.9524	0.9167	0.8511	0.8989	0.9127
	Ectasia	0.9286	0.9762	0.9512	0.9398	
	Other disease	0.8571	0.9762	0.9474	0.9	
	Macro-average	0.9127	0.9563	0.9165	0.9129	
Modified MobileNetV3-Large	Normal	0.9286	0.9524	0.9070	0.9176	0.9286
	Ectasia	0.9524	0.9643	0.9302	0.9412	
	Other disease	0.9048	0.9762	0.95	0.9268	
	Macro-average	0.9286	0.9643	0.9291	0.9285	
Modified ResNet18	Normal	0.9048	0.8929	0.8085	0.8539	0.8968
	Ectasia	0.8809	0.9762	0.9487	0.9136	
	Other disease	0.9048	0.9762	0.95	0.9268	
	Macro-average	0.8968	0.9484	0.9024	0.8981	

**Figure 8.** GUI for corneal condition prediction. Abbreviation: GUI = Graphical User Interface.

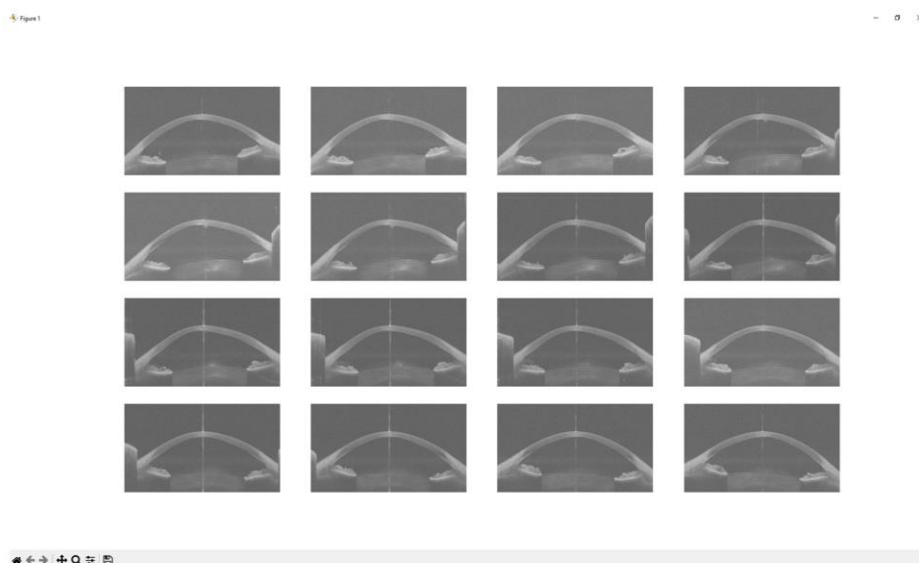


Figure 9. Images extracted and scaled from the selected raw data file.

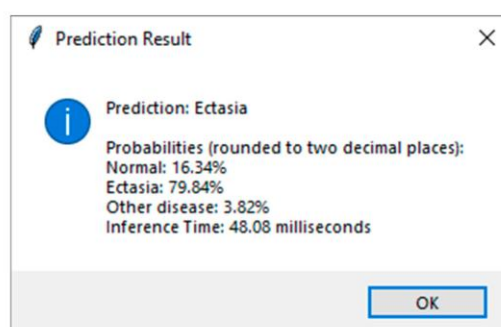


Figure 10. Prediction result of the selected raw data file.

4. Discussion

In this study, four deep learning models were modified to diagnose corneal conditions using the raw data from the Casia2. The raw data exported from the Casia2 consist of sixteen meridional images. Accordingly, sixteen channels were introduced to the modified models to receive the sixteen images.

Among four modified CNN models, the modified MobileNetV3-Large achieved the highest overall accuracy of 92.86%. For the modified MobileNetV3-Large, among the 200 epochs, epoch 89 achieved the highest accuracy on the validation dataset. The model from epoch 89 was used for evaluation on the test dataset and for generating Grad-CAM. According to the results, the modified MobileNetV3-Large correctly predicted 117 out of 126 examinations. The 'ectasia' class had the highest number of correct predictions, with 40 out of 42, followed by 'normal', with 39 out of 42, and 'other disease', with 38 out of 42. Since the modified MobileNetV3-Large had higher overall accuracy than the other modified CNN models, it was run four additional times with seed numbers from two to five

to validate the robustness and reliability of the results. Table 4 shows the mean \pm standard deviation for each performance metric across five runs of the modified MobileNetV3-Large by using seed numbers from one to five.

Table 4. Performance metrics (mean \pm standard deviation) of the modified MobileNetV3-Large evaluated on the test dataset across five runs with different seed numbers. Abbreviation: PPV = Positive Predictive Value.

Model	Group	Sensitivity	Specificity	PPV	F1 Score	Overall Accuracy
Modified MobileNetV3-Large	Normal	0.9095 \pm 0.0391	0.9048 \pm 0.0895	0.8424 \pm 0.1125	0.8703 \pm 0.0631	0.8937 \pm 0.0519
	Ectasia	0.9191 \pm 0.1019	0.9643 \pm 0.0266	0.9332 \pm 0.0475	0.9214 \pm 0.0418	
	Other disease	0.8524 \pm 0.0865	0.9714 \pm 0.0065	0.9366 \pm 0.0165	0.8910 \pm 0.0528	
	Macro-average	0.8937 \pm 0.0519	0.9468 \pm 0.0260	0.9041 \pm 0.0357	0.8942 \pm 0.0502	

There were four eye examinations that were predicted as ‘normal’ by the modified MobileNetV3-Large but were diagnosed as ‘ectasia’ or ‘other disease’ by all three experienced ophthalmologists. For each of these four eye examinations, the first of sixteen equi-angular meridional images, with the aspect ratio adjusted to 1.629 (width divided by height) to better represent the realistic shape of the eye, is shown in Figure 11.

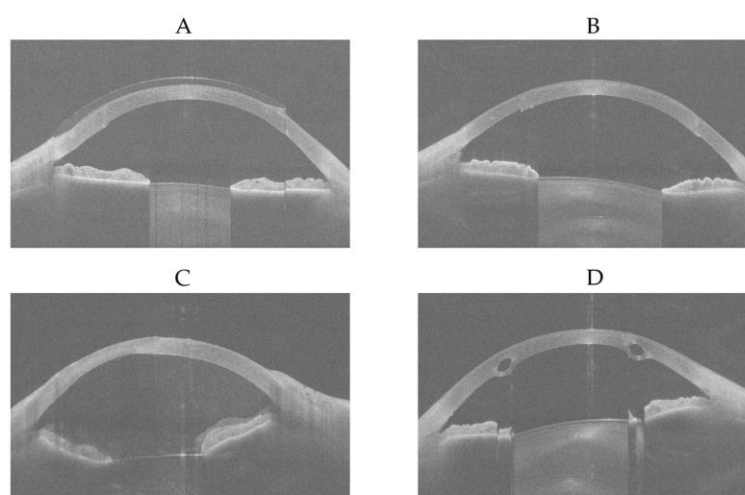


Figure 11. First of sixteen equi-angular meridional images, with the aspect ratio adjusted to 1.629 (width divided by height). (A) ‘other disease’-labelled but predicted as ‘normal’. (B) ‘other disease’-labelled but predicted as ‘normal’. (C) ‘other disease’-labelled but predicted as ‘normal’. (D) ‘ectasia’-labelled but predicted as ‘normal’.

It was determined that Figure 11A shows an eye examined while wearing a contact lens after penetrating keratoplasty; as the contact lens regularised the corneal surface, it was predicted as ‘normal’ by the modified MobileNetV3-Large. Figure 11B shows an eye that has undergone penetrating keratoplasty, which likely resulted in regularisation of the corneal surface, and therefore it was also predicted as ‘normal’ by the modified MobileNetV3-Large. Since the ‘other disease’ class contained eyes with penetrating keratoplasty, subepithelial or stromal scarring, corneal dystrophies, Salzmann’s nodules, or pterygium, the wide variety

of conditions within the 266 eye examinations may have limited the modified MobileNetV3-Large's ability to learn the differences among these diseases effectively. However, with a larger number of keratoplasty samples, it is possible that the model would recognise this condition better. Figure 11C was diagnosed as showing stromal corneal scarring and Descemet's folds indicative of endothelial dysfunction, along with vitreous prolapse into the anterior chamber. No explanation could be provided as to why this case was predicted as 'normal' by the modified MobileNetV3-Large. Figure 11D shows intrastromal corneal ring segments implanted surgically due to ectasia; the resulting regularisation of the corneal surface likely led to it being predicted as 'normal' by the modified MobileNetV3-Large. Figure 12 shows the Grad-CAMs of these four eye examinations generated by the modified MobileNetV3-Large.

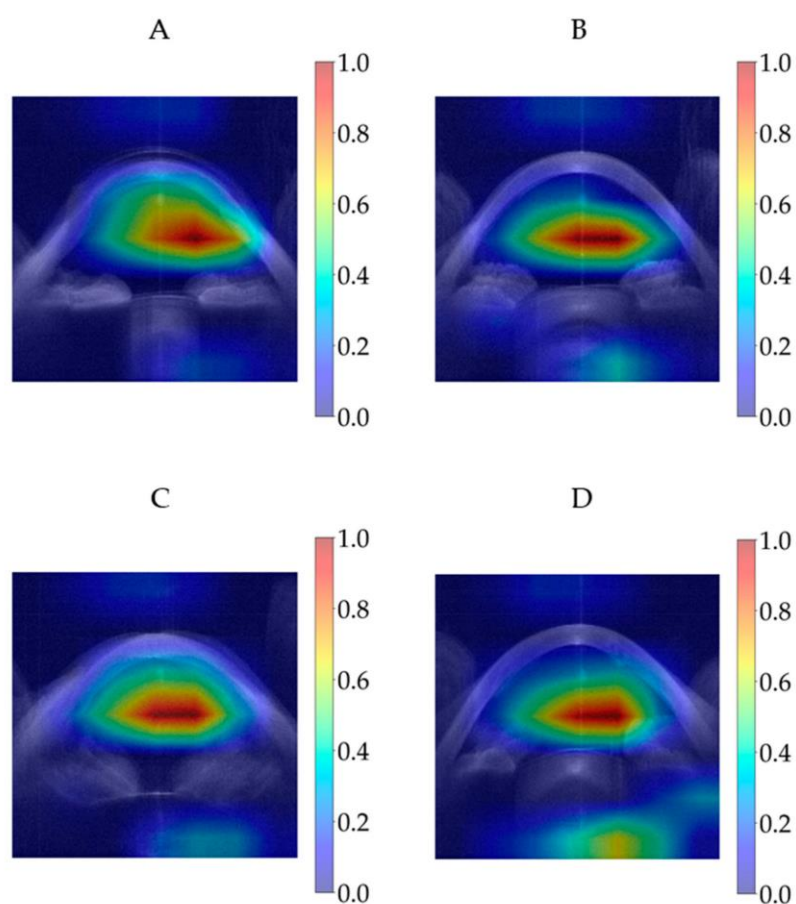


Figure 12. Grad-CAMs of eye examinations generated by the modified MobileNetV3-Large. (A) 'other disease'-labelled but predicted as 'normal'. (B) 'other disease'-labelled but predicted as 'normal'. (C) 'other disease'-labelled but predicted as 'normal'. (D) 'ectasia'-labelled but predicted as 'normal'. Abbreviation: Grad-CAM = Gradient-Weighted Class Activation Mapping.

Quanchareonsap et al. [16] tested three AI models based on EfficientNet-B7 to differentiate between normal cornea, subclinical keratoconus and keratoconus using tomographic

maps from the Pentacam and corneal biomechanics from the Corvis ST. AI model 1, which used refractive maps from the Pentacam, achieved a macro-average accuracy of 93.6%, a macro-average sensitivity of 86%, a macro-average specificity of 95.7% and a macro-average PPV of 81.1%. For AI model 2, the dynamic corneal response and the Vinciguerra screening report from the Corvis ST were added to AI model 1. AI model 2 achieved a macro-average accuracy of 95.7%, a macro-average sensitivity of 73.7%, a macro-average specificity of 96.1% and a macro-average PPV of 95.3%. For AI model 3, the corneal biomechanical index was incorporated into AI model 2. AI model 3 achieved a macro-average accuracy of 95.7%, a macro-average sensitivity of 73.7%, a macro-average specificity of 96.1% and a macro-average PPV of 95.3%. Zhang et al. [17] used the CorNet model for the diagnosis of keratoconus using Corvis ST raw data. The dataset consisted of 1786 Corvis ST raw data samples, with 70% allocated to the training set and 30% to the validation set. The CorNet model achieved an accuracy of 92.13%, a sensitivity of 92.49%, a specificity of 91.54%, a PPV of 94.77% and a F1 score of 93.62%. Abdelmotaal et al. [18] developed a DenseNet121-based CNN model to distinguish between normal eyes and eyes with keratoconus using 734 Corvis ST videos from 734 eyes. The model achieved an accuracy of 89% on the test set, which comprised 30% of a dataset of 502 subjects, with the remaining 70% used for training and an accuracy of 88% on a separate dataset of 232 subjects. Fassbind et al. [19] employed preprocessed OCT data from a Casia2 device to diagnose corneal conditions, including healthy, keratoconus, post-laser, keratoglobus, pellucid marginal corneal degeneration, other and not appreciable, using the CorNeXt CNN model, which builds on the ConvNeXt architecture [36]. The model achieved a weighted-average accuracy of 93.52%, a weighted-average sensitivity of 84.30%, a weighted-average specificity of 99% and a weighted-average F1 score of 88.17%. For keratoconus detection specifically, it achieved an accuracy of 92.56%, a sensitivity of 84.07%, a specificity of 100% and an F1 score of 91.34%.

In comparison with [19], the macro-average F1 score of the modified MobileNetV3-Large achieved in this study (92.85%) exceeded the weighted-average F1 score of 88.17%, derived from the value reported in [19]. Moreover, the F1 score of the modified MobileNetV3-Large in this study for the 'ectasia' class (94.12%) is higher than the F1 score of 91.34% for the Keratoconus class, derived from the value reported in [19]. These findings indicate that using raw OCT data can outperform approaches based on preprocessed data in diagnosing corneal conditions.

Since the modified MobileNetV3-Large had higher overall accuracy than the other modified CNN models, it was selected for application in the GUI. The modified MobileNetV3-Large with a seed number of four achieved higher overall accuracy (94.44%) than the model with seed number one reported in Table 3 (92.86%); therefore, this model was used in the GUI. The GUI provides a classification of the corneal condition and the probability for each class. The user can select a raw data file in .3dv format and has the option to view the sixteen automatically scaled extracted images from the selected file, with the ability to zoom in on each image. This feature allows the user to compare the diagnosis provided by the GUI with what they observe in the images. The GUI helps ophthalmologists obtain a prediction from an eye examination taken with the Casia2 anterior-segment OCT and allows them to determine the corneal condition regardless of changes to the Casia2 software version.

However, this study has four limitations that must be considered. Firstly, only four CNN models were modified and tested, and it is possible that other models could achieve better results. Secondly, although 2737 eye examinations were decided to belong to one of the three classes, 1325 of these were decided to be 'normal' by all three experienced ophthalmologists. This represents approximately 73.49% (rounded to two decimal places) of the 1803 eye examinations for which all the three experienced ophthalmologists decided

on the same labels. To create a balanced test dataset, 42 eye examinations were selected for each class, and this corresponded to approximately 16.93% (rounded to two decimal places) of the total dataset. If the ‘ectasia’ and ‘other disease’ classes had more samples, it would have been possible to train the architecture and test a larger number of samples from these classes. Thirdly, mismatched cases between three experienced ophthalmologists were disregarded, which may have affected the generalisability of the findings to all patient populations. Fourthly, the dataset was monocentric. These limitations indicate areas for further research and refinement, which may affect overall accuracy.

5. Conclusions

In this study, raw OCT data were used to diagnose corneal conditions, including ‘normal’, ‘ectasia’ and ‘other disease’. Using raw data has advantages over preprocessed data, such as remaining unchanged with new software tools and updates and providing a more reliable foundation for analysis. The successful application of four CNN architectures with raw OCT data validates the use of raw OCT data for the diagnosis of corneal conditions in ophthalmology. Moreover, the GUI helps ophthalmologists obtain a prediction from an eye examination performed with the Casia2 anterior-segment OCT.

Author Contributions: Conceptualization, A.L. and M.M.; data labelling, A.D.A., E.F. and N.S.; methodology, M.M.; software, M.M. and M.S.; validation, A.L.; formal analysis, M.M.; investigation, M.M.; resources, A.L.; data curation, M.M.; writing—original draft preparation, M.M.; writing—review and editing, A.D.A., B.S., A.L., E.F. and N.S.; visualization, M.M.; supervision, A.L.; project administration, A.L.; funding acquisition, A.L. All authors have read and agreed to the published version of the manuscript.

Funding: M.M. was supported in part by the Dr. Rolf M. Schwiete Stiftung under project no. 2020-024.

Institutional Review Board Statement: This study is a retrospective data analysis and has been exempted by the local institutional review board (Ärztammer des Saarlandes, registration number 157/21) on 31 May 2021.

Informed Consent Statement: All data processed in this study were already anonymised at the source before being transferred to us for processing. This precludes any back-tracing of the identity, and therefore, informed consent of the patients was not necessary.

Data Availability Statement: The Python scripts and some data files are openly available from Zenodo at <https://doi.org/10.5281/zenodo.17711223>.

Acknowledgments: During the preparation of this manuscript, the corresponding author used ChatGPT (version 5-mini) for the purpose of text correction in British English. The authors have reviewed and edited the output and take full responsibility for the content of this publication.

Conflicts of Interest: The authors declare no conflicts of interest. The funders had no role in the design of the study; in the collection, analyses, or interpretation of data; in the writing of the manuscript; or in the decision to publish the results.

Abbreviations

The following abbreviations are used in this manuscript:

AI	Artificial Intelligence
CNN	Convolutional Neural Network
CPU	Central Processing Unit
CSV	Comma-Separated Values
FP	False Positive
FN	False Negative
Grad-CAM	Gradient-Weighted Class Activation Mapping

GUI	Graphical User Interface
KC	Keratoconus
OCT	Optical Coherence Tomography
PNG	Portable Network Graphics
PPV	Positive Predictive Value
RAM	Random-Access Memory
RGB	Red–Green–Blue
TP	True Positive
TN	True Negative

References

- Pang, G.; Wang, C.; Wang, X.; Li, X.; Meng, Q. A review of human cornea finite element modeling: Geometry modeling, constitutive modeling, and outlooks. *Front. Bioeng. Biotechnol.* **2024**, *12*, 1455027. [\[CrossRef\]](#) [\[PubMed\]](#)
- Santodomingo-Rubido, J.; Carracedo, G.; Suzuki, A.; Villa-Collar, C.; Vincent, S.J.; Wolffsohn, J.S. Keratoconus: An updated review. *Contact Lens Anterior Eye* **2022**, *45*, 101559. [\[CrossRef\]](#)
- Espandar, L.; Meyer, J. Keratoconus: Overview and update on treatment. *Middle East Afr. J. Ophthalmol.* **2010**, *17*, 15–20. [\[CrossRef\]](#)
- Singh, R.B.; Koh, S.; Sharma, N.; Woreta, F.A.; Hafezi, F.; Dua, H.S.; Jhanji, V. Keratoconus. *Nat. Rev. Dis. Primers* **2024**, *10*, 81. [\[CrossRef\]](#)
- Rabinowitz, Y.S. Keratoconus. *Surv. Ophthalmol.* **1998**, *42*, 297–319. [\[CrossRef\]](#)
- Martin, R. Cornea and anterior eye assessment with placido-disc keratometry, slit scanning evaluation topography and scheinplufug imaging tomography. *Indian J. Ophthalmol.* **2018**, *66*, 360–366. [\[CrossRef\]](#) [\[PubMed\]](#)
- Martin, R. Cornea and anterior eye assessment with slit lamp biomicroscopy, specular microscopy, confocal microscopy, and ultrasound biomicroscopy. *Indian J. Ophthalmol.* **2018**, *66*, 195–201. [\[CrossRef\]](#)
- Mohan, S.; Aggarwal, A.; Dada, T.; Vanathi, M.; Panda, A. Pachymetry: A review. *DOS Times* **2007**, *12*, 19–28.
- Seitz, B.; Behrens, A.; Langenbucher, A. Corneal topography. *Curr. Opin. Ophthalmol.* **1997**, *8*, 8–24. [\[CrossRef\]](#)
- Fan, R.; Chan, T.C.; Prakash, G.; Jhanji, V. Applications of corneal topography and tomography: A review. *Clin. Exp. Ophthalmol.* **2018**, *46*, 133–146. [\[CrossRef\]](#)
- Schmitt, J.M. Optical coherence tomography (oct): A review. *IEEE J. Sel. Top. Quantum Electron.* **2002**, *5*, 1205–1215. [\[CrossRef\]](#)
- Zhang, X.; Munir, S.Z.; Sami Karim, S.A.; Munir, W.M. A review of imaging modalities for detecting early keratoconus. *Eye* **2021**, *35*, 173–187. [\[CrossRef\]](#) [\[PubMed\]](#)
- Anton, N.; Doroftei, B.; Curteanu, S.; Catalin, L.; Ilie, O.D.; Tărcoveanu, F.; Bogdănici, C.M. Comprehensive review on the use of artificial intelligence in ophthalmology and future research directions. *Diagnostics* **2022**, *13*, 100. [\[CrossRef\]](#)
- Goodman, D.; Zhu, A.Y. Utility of artificial intelligence in the diagnosis and management of keratoconus: A systematic review. *Front. Ophthalmol.* **2024**, *4*, 1380701. [\[CrossRef\]](#) [\[PubMed\]](#)
- Maeda, N.; Klyce, S.D.; Smolek, M.K.; Thompson, H.W. Automated keratoconus screening with corneal topography analysis. *Investig. Ophthalmol. Vis. Sci.* **1994**, *35*, 2749–2757.
- Quanchareonsap, W.; Kasetuwan, N.; Reinprayoon, U.; Piyacomn, Y.; Wungcharoen, T.; Jermjutitham, M. Deep Learning Algorithm for Keratoconus Detection from Tomographic Maps and Corneal Biomechanics: A Diagnostic Study. *J. Curr. Ophthalmol.* **2024**, *36*, 46–53. [\[CrossRef\]](#)
- Zhang, P.; Yang, L.; Mao, Y.; Zhang, X.; Cheng, J.; Miao, Y.; Bao, F.; Chen, S.; Zheng, Q.; Wang, J. CorNet: Autonomous feature learning in raw Corvis ST data for keratoconus diagnosis via residual CNN approach. *Comput. Biol. Med.* **2024**, *172*, 108286. [\[CrossRef\]](#)
- Abdelmotaal, H.; Hazarbassanov, R.M.; Salouti, R.; Nowroozzadeh, M.H.; Taneri, S.; Al-Timemy, A.H.; Lavric, A.; Yousefi, S. Keratoconus Detection-based on Dynamic Corneal Deformation Videos Using Deep Learning. *Ophthalmol. Sci.* **2023**, *4*, 100380. [\[CrossRef\]](#)
- Fassbind, B.; Langenbucher, A.; Streich, A. Automated cornea diagnosis using deep convolutional neural networks based on cornea topography maps. *Sci. Rep.* **2023**, *13*, 6566. [\[CrossRef\]](#)
- Feng, R.; Xu, Z.; Zheng, X.; Hu, H.; Jin, X.; Chen, D.Z.; Yao, K.; Wu, J. Kernet: A novel deep learning approach for keratoconus and sub-clinical keratoconus detection based on raw data of the pentacam hr system. *IEEE J. Biomed. Health Inform.* **2021**, *25*, 3898–3910. [\[CrossRef\]](#) [\[PubMed\]](#)
- Al-Timemy, A.H.; Mosa, Z.M.; Alyasseri, Z.; Lavric, A.; Lui, M.M.; Hazarbassanov, R.M.; Yousefi, S. A Hybrid Deep Learning Construct for Detecting Keratoconus From Corneal Maps. *Transl. Vis. Sci. Technol.* **2021**, *10*, 16. [\[CrossRef\]](#) [\[PubMed\]](#)
- Hara, N.; Benedikt, K.; Owaki, H. CASIA2: Anterior Segment 3D Swept-Source OCT. In *Intraocular Lens Calculations*; Aramberri, J., Hoffer, K.J., Olsen, T., Savini, G., Shammas, H.J., Eds.; Essentials in Ophthalmology; Springer: Cham, Switzerland, 2024.

23. Li, Z.; Liu, F.; Yang, W.; Peng, S.; Zhou, J. A survey of convolutional neural networks: Analysis, applications, and prospects. *IEEE Trans. Neural Netw. Learn. Syst.* **2022**, *33*, 6999–7019. [[CrossRef](#)]
24. Taye, M.M. Theoretical understanding of convolutional neural network: Concepts, architectures, applications, future directions. *Computation* **2023**, *11*, 52. [[CrossRef](#)]
25. Huang, G.; Liu, Z.; Van Der Maaten, L.; Weinberger, K.Q. Densely connected convolutional networks. In Proceedings of the IEEE Conference on Computer Vision and Pattern Recognition, Honolulu, HI, USA, 21–26 July 2017; pp. 4700–4708.
26. Tan, M.; Le, Q. Efficientnet: Rethinking model scaling for convolutional neural networks. In Proceedings of the International Conference on Machine Learning, Long Beach, CA, USA, 9–15 June 2019; pp. 6105–6114.
27. Howard, A.G.; Zhu, M.; Chen, B.; Kalenichenko, D.; Wang, W.; Weyand, T.; Andreetto, M.; Adam, H. Mobilenets: Efficient convolutional neural networks for mobile vision applications. *arXiv* **2017**, arXiv:1704.04861. [[CrossRef](#)]
28. He, K.; Zhang, X.; Ren, S.; Sun, J. Deep residual learning for image recognition. In Proceedings of the IEEE Conference on Computer Vision and Pattern Recognition, Las Vegas, NV, USA, 27–30 June 2016; pp. 770–778.
29. Paszke, A.; Gross, S.; Massa, F.; Lerer, A.; Bradbury, J.; Chanan, G.; Killeen, T.; Lin, Z.; Gimelshein, N.; Antiga, L.; et al. Pytorch: An imperative style, high-performance deep learning library. *Adv. Neural Inf. Process. Syst.* **2019**, *32*, 1–12.
30. Wang, Q.; Ma, Y.; Zhao, K.; Tian, Y. A comprehensive survey of loss functions in machine learning. *Ann. Data Sci.* **2022**, *9*, 187–212. [[CrossRef](#)]
31. Zhou, P.; Xie, X.; Lin, Z.; Yan, S. Towards understanding convergence and generalization of adamw. *IEEE Trans. Pattern Anal. Mach. Intell.* **2024**, *46*, 6486–6493. [[CrossRef](#)]
32. Krogh, A.; Hertz, J. A simple weight decay can improve generalization. *Adv. Neural Inf. Process. Syst.* **1991**, *4*, 950–957.
33. Ying, X. An overview of overfitting and its solutions. *J. Phys. Conf. Ser.* **2019**, *1168*, 022022. [[CrossRef](#)]
34. Hicks, S.A.; Strümke, I.; Thambawita, V.; Hammou, M.; Riegler, M.A.; Halvorsen, P.; Parasa, S. On evaluation metrics for medical applications of artificial intelligence. *Sci. Rep.* **2022**, *12*, 5979. [[CrossRef](#)]
35. Selvaraju, R.R.; Cogswell, M.; Das, A.; Vedantam, R.; Parikh, D.; Batra, D. Grad-cam: Visual explanations from deep networks via gradient-based localization. In Proceedings of the IEEE International Conference on Computer Vision, Venice, Italy, 22–29 October 2017; pp. 618–626.
36. Liu, Z.; Mao, H.; Wu, C.Y.; Feichtenhofer, C.; Darrell, T.; Xie, S. A convnet for the 2020s. In Proceedings of the IEEE/CVF Conference on Computer Vision and Pattern Recognition, New Orleans, LA, USA, 18–24 June 2022; pp. 11976–11986.

Disclaimer/Publisher’s Note: The statements, opinions and data contained in all publications are solely those of the individual author(s) and contributor(s) and not of MDPI and/or the editor(s). MDPI and/or the editor(s) disclaim responsibility for any injury to people or property resulting from any ideas, methods, instructions or products referred to in the content.

4.3 Article 3

This article introduces a Graphical User Interface (GUI) based on a modified EfficientNet-B0, as a CNN model, which predicts the corneal ectasia score and classifies eyes into one of three categories: ‘No detectable ectasia pattern’, ‘Suspected ectasia’, or ‘Clinical ectasia’, by selecting a raw data file in 3dv format from the cornea/anterior segment OCT Casia2. Moreover, the performance of the modified EfficientNet-B0 was evaluated for a two-class classification, with the dataset classified according to an ESI of 5, as defined by the device. ESI values of 5 and above denoted the E (Ectasia) class, reflecting either suspected ectasia or clinical ectasia, whereas ESI values below 5 were classified as NE (No Ectasia), reflecting the absence of any ectatic pattern [77].

Article

A Deep Learning-Based Graphical User Interface for Predicting Corneal Ectasia Scores from Raw Optical Coherence Tomography Data

Maziar Mirsalehi *  and Achim Langenbucher 

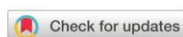
Department of Experimental Ophthalmology, Saarland University, Kirrberger Street 100,
66424 Homburg, Germany

* Correspondence: maziar.mirsalehi@uni-saarland.de

Abstract

Background/Objectives: Keratoconus, a condition in which the cornea becomes thinner and steeper, can cause visual problems, particularly when it is progressive. Early diagnosis is important for preserving visual acuity. Raw data, unlike preprocessed data, are unaffected by software modifications. They retain their native structure across versions, providing consistency for analytical purposes. The objective of this study was to design a deep learning-based graphical user interface for predicting the corneal ectasia score using raw optical coherence tomography data. **Methods:** The graphical user interface was developed using Tkinter, a Python library for building graphical user interfaces. The user is allowed to select raw data from the cornea/anterior segment optical coherence tomography Casia2, which is generated in the 3dv format, from the local system. To view the predicted corneal ectasia score, the user must determine whether the selected 3dv file corresponds to the left or right eye. Extracted optical coherence tomography images are cropped, resized to 224×224 pixels and processed by the modified EfficientNet-B0 convolutional neural network to predict the corneal ectasia score. The predicted corneal ectasia score value is displayed along with a diagnosis: ‘No detectable ectasia pattern’ or ‘Suspected ectasia’ or ‘Clinical ectasia’. Performance metric values were rounded to four decimal places, and the mean absolute error value was rounded to two decimal places. **Results:** The modified EfficientNet-B0 obtained a mean absolute error of 6.65 when evaluated on the test dataset. For the two-class classification, it achieved an accuracy of 87.96%, a sensitivity of 82.41%, a specificity of 96.69%, a positive predictive value of 97.52% and an F1 score of 89.33%. For the three-class classification, it attained a weighted-average F1 score of 84.95% and an overall accuracy of 84.75%. **Conclusions:** The graphical user interface outputs numerical ectasia scores, which improves other categorical labels. The graphical user interface enables consistent diagnostics, regardless of software updates, by using raw data from the Casia2. The successful use of raw optical coherence tomography data indicates the potential for raw optical coherence tomography data to be used, rather than preprocessed optical coherence tomography data, for diagnosing keratoconus.

Keywords: CNN; cornea; deep learning; ectasia; eye; keratoconus; OCT; raw data; vision



Academic Editors: Cristina Nicula
and Alina Popa-Cherecheanu

Received: 26 November 2025

Revised: 8 January 2026

Accepted: 14 January 2026

Published: 18 January 2026

Copyright: © 2026 by the authors.

Licensee MDPI, Basel, Switzerland.

This article is an open access article distributed under the terms and conditions of the [Creative Commons Attribution \(CC BY\)](https://creativecommons.org/licenses/by/4.0/) license.

1. Introduction

The eye is an important part of the human body. It contains tissues such as the cornea, sclera, lens, iris, vitreous, aqueous humour, retina and optic nerve. The cornea has two-thirds of the refractive power of the eye, which makes it important for vision. The cornea

has five layers, including the epithelium, stroma and endothelium as cellular layers and Bowman's layer and Descemet's membrane as acellular layers [1,2].

Keratoconus is a condition in which the cornea becomes thinner and steeper. It commonly impacts both eyes, although the severity can vary. This condition can lead to vision problems and can be found in both males and females, with approximately 1 in 2000 people experiencing it. However, it is predominant in males, starting mostly in the second or, at the latest, the third decade of life. Eye rubbing is considered a major risk factor for keratoconus. Early keratoconus can be identified using various diagnostic tools, including handheld keratoscopes (Placido discs), slit-lamp biomicroscopy, ultrasonic pachymetry and techniques such as corneal topography and tomography, like Scheimpflug imaging and Optical Coherence Tomography (OCT). Scheimpflug imaging uses a rotating camera to generate images, while OCT measures the time delay of reflected light from the cornea's anterior surface by relating it to a reference. Corneal topography illustrates the form of the cornea's anterior surface, whereas corneal tomography provides a three-dimensional representation of the entire cornea. Placido-based topography primarily assesses the central anterior corneal surface and may fail to detect posterior elevation abnormalities, which are indicative of early keratoconus. Disadvantages of slit-lamp biomicroscopy include a dependence on trained professionals and difficulty in detecting subtle early signs of keratoconus. A disadvantage of ultrasonic pachymetry is the possibility of corneal damage due to repeated contact with the probe. Corneal topographers have limitations, such as a sensitivity to non-optimal conditions, like dry eye syndrome and long eyelashes; poor repeatability in children; high costs; and limited portability. Corneal tomography is costly, not portable, requires clinical expertise and depends on patient cooperation, which limits its use in large-scale screening and makes it impractical in many regions. OCT involves an expensive, non-portable tool that requires technician training. Its limited effectiveness when used alone for detecting early keratoconus emphasises the need for complementary imaging techniques or Artificial Intelligence (AI)-based methods to improve accuracy [3–9].

High-resolution anterior segment tomographers are excellent tools to image the cornea and the entire anterior eye segment, and most of them have proprietary (undisclosed) software tools that assist in screening or diagnosing ectatic diseases such as keratoconus. The data can typically be used in its raw form or preprocessed form. Preprocessed data is modified by software, and the changes made may not be completely clear. Additionally, software updates may introduce variations in data processing that cause inconsistencies in the results. Unlike processed data, raw data is not modified by software. Consequently, it maintains its original structure across various software versions, providing a more consistent basis for analysis. According to our knowledge, this is the first study to apply raw OCT data in a Graphical User Interface (GUI) for the prediction of corneal ectasia scores. The GUI outputs numerical ectasia scores, improving over categorical labels, and ensures consistent results from three-dimensional optical coherence tomography data, unaffected by software changes.

2. Materials and Methods

2.1. Data

Data were collected from patients examined at the Department of Ophthalmology, Saarland University Medical Centre, Homburg, Germany, between 1 February 2021 and 1 September 2023 using the cornea/anterior segment OCT Casia2 (Tomey, Nagoya, Japan) for data acquisition. Casia2 is an OCT-based diagnostic instrument. Raw data generated by the Casia2 system are stored in 3dv format, with individual files corresponding to corneal maps. Every 3dv file consists of data from 16 equiangular meridional images. These images were stored as 16-bit unsigned integers. The 16 equiangular meridional images from each

<https://doi.org/10.3390/diagnostics16020310>

3dv file—each with a resolution of 800 pixels in width and 1464 pixels in height, with a horizontal measurement range of 16 mm and a depth of 11 mm in anterior segment mode—were first extracted and then saved as greyscale Portable Network Graphic (PNG) files. The Ectasia Screening Index (ESI) is a value provided by the Casia2 for screening corneal ectasia. If the ESI result is within the range of 0 to 4, no ectasia pattern is detectable. A value ranging from 5 to 29 indicates suspected ectasia, whereas a value ranging from 30 to 95 indicates clinical ectasia. The ESI is recorded for each measurement in a CSV (Comma-Separated Value) file; 6141 files from 15,457 were chosen for training, validation and testing. The remaining files were disregarded due to corneal defects like keratoplasty. The data were split into three separate sets, including 4898 files for training, 620 files for validation and 623 files for testing.

Two classification approaches were evaluated: a two-class classification separating the no detectable ectasia pattern from suspected ectasia and clinical ectasia combined into a single class and a three-class classification distinguishing the no detectable ectasia pattern, suspected ectasia and clinical ectasia. For the two-class classification, files were categorised according to an ESI threshold of 5, as defined by the Casia2. Files with an ESI below 5 are categorised as NE (No Ectasia), indicating no detectable ectasia pattern, whereas files with an ESI of 5 or higher are categorised as E (Ectasia), indicating either suspected ectasia or clinical ectasia. In the training set, 2065 files belonged to the NE class, and 2833 files belonged to the E class. In the validation set, 242 files were classified as NE, and 378 files were classified as E. For the test set, 242 files belonged to the NE class, and 381 files belonged to the E class. Table 1 summarises the distribution of data for the two-class classification across the training, validation and test sets.

Table 1. The distribution of the dataset for the two-class classification across training, validation and test sets. Abbreviations: NE = No Ectasia and E = Ectasia.

Dataset	NE	E	Total
Training	2065	2833	4898
Validation	242	378	620
Test	242	381	623

For the three-class classification, files with an ESI below 5, according to the Casia2 criteria, are categorised as NE (No Ectasia), which indicates no detectable ectasia pattern. Files with an ESI ranging from 5 to 29, according to the Casia2 criteria, are categorised as SE (Suspected Ectasia), indicating suspected ectasia, while files with an ESI ranging from 30 to 95, according to the Casia2 criteria, are categorised as CE (Clinical Ectasia), which indicates clinical ectasia. In the training set, 2065 files belong to the NE class, 907 files belong to the SE class and 1926 files belong to the CE class. In the validation set, 242 files are classified as NE, 117 files belong to the SE class and 261 files belong to the CE class. For the test set, 242 files belong to the NE class, 103 files belong to the SE class and 278 files belong to the CE class. Table 2 summarises the distribution of data for the three-class classification across the training, validation and test sets.

Table 2. The distribution of the dataset for the three-class classification across training, validation and test sets. Abbreviations: NE = No Ectasia, SE = Suspected Ectasia and CE = Clinical Ectasia.

Dataset	NE	SE	CE	Total
Training	2065	907	1926	4898
Validation	242	117	261	620
Test	242	103	278	623

<https://doi.org/10.3390/diagnostics16020310>

In this study, age and sex were not regarded as critical factors.

Figure 1 shows 16 equiangular meridional images extracted from a 3dv file, which corresponds to a right eye examination with an ESI of 47.

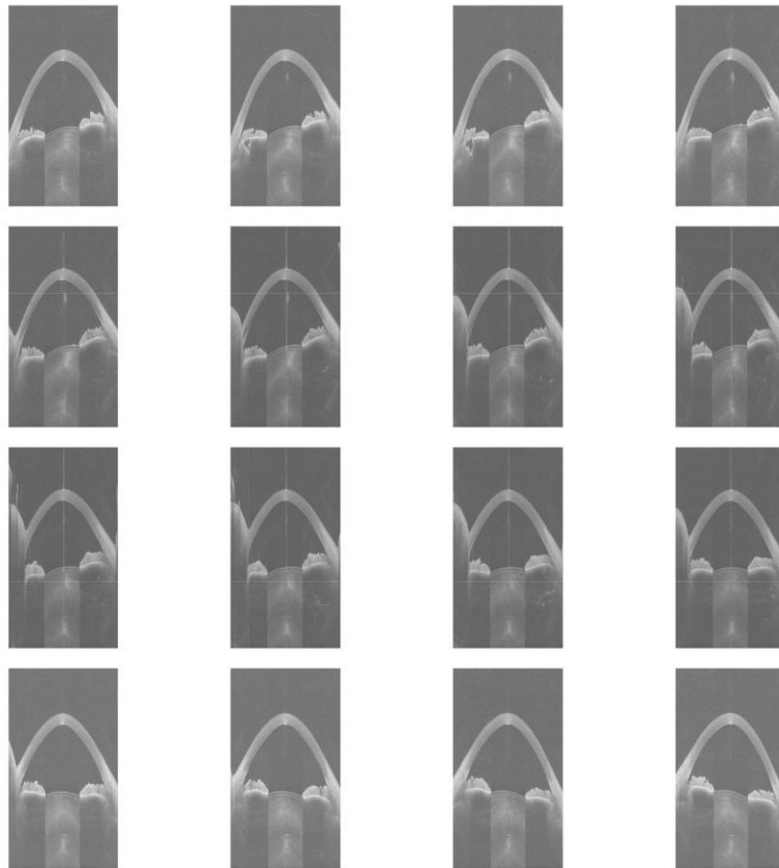


Figure 1. Sixteen equiangular meridional images extracted from a 3dv file.

The image preprocessing consisted of trimming 25% from the left edge and 25% from the right edge of the images to remove irrelevant eyelid portions, as well as cropping 60% from the bottom to exclude areas outside the cornea. Following this, the images were resized to 224×224 pixels, which matches the initial resolution chosen for the EfficientNet-B0 model [10]. Figure 2 illustrates the cropped and resized versions of the images extracted from the same 3dv file shown in Figure 1.

<https://doi.org/10.3390/diagnostics16020310>

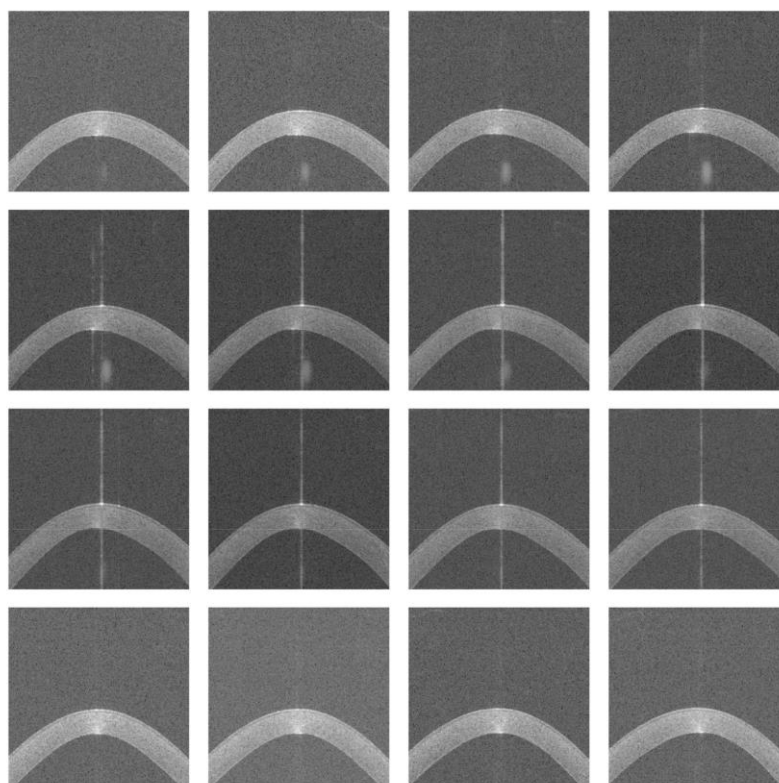


Figure 2. Cropped and resized images.

2.2. Training Architecture

EfficientNet-B0 [10] was employed as the CNN architecture in the GUI. Python (version 3.12.3) [11] and the PyTorch library (version 2.3.0) [12] were used to train the architecture from scratch. Training was conducted on a system with an 11th Gen Intel® Core™ i7-11700 processor running at 2.5 GHz, supported by 32 GB of RAM and equipped with a 64-bit operating system and an x64-based processor.

Each set of 16 cropped and resized images was combined into a single stacked input and provided to the EfficientNet-B0 model. The initial convolutional layer of EfficientNet-B0 was modified to accept a 16-channel input. The classifier head was adapted for a single-output task and consists of two fully connected layers with dimensions of 1280 to 1000 and 1000 to 1, with a dropout layer applied to the output of the first fully connected layer, with a dropout probability of 0.2 to reduce overfitting. An additional fully connected fusion layer was incorporated to combine the single output from the classifier with two eye parameter features corresponding to the left and right eyes. This fusion layer has three input features and one output feature and employs a linear (identity) activation function. The additional fully connected layer produces a single numerical value as the CNN architecture's final output. The total number of trainable parameters in the proposed model is 5,293,297.

Table 3 shows the differences between the original EfficientNet-B0 and the modified version used in this study.

<https://doi.org/10.3390/diagnostics16020310>

Table 3. A comparison of the original CNN models with their modified versions. Abbreviation: CNN = Convolutional Neural Network.

CNN Model	Number of Input Channels	Number of Output Features
EfficientNet-B0	3	1000
Modified EfficientNet-B0	16	1

The architecture was trained for 80 epochs to ensure sufficient learning. The batch size for the training, validation and test sets was 128. The loss function chosen to minimise prediction errors was the Mean Squared Error (MSE). To optimise the architecture parameters, the AdamW optimiser was used with a learning rate of 0.01, as [13] found that AdamW results in faster convergence and better generalisation compared to Adam. A learning rate of 0.01 is considered effective because it offers a balance between being large enough for faster convergence and small enough to avoid instability or overshooting the optimal solution, ensuring efficient training. A learning rate scheduler was also applied to change the learning rate when a plateau was reached, with a reduction factor of 0.1 and a patience of 5 epochs. Specifically, the scheduler monitors the validation loss and reduces the learning rate by a factor of 0.1 if no improvement is observed for 5 consecutive epochs. Additionally, a weight decay of 0.04 was applied to help prevent overfitting by regularising the architecture's parameters. Figure 3 illustrates the workflow for predicting the corneal ectasia score by using the modified EfficientNet-B0.

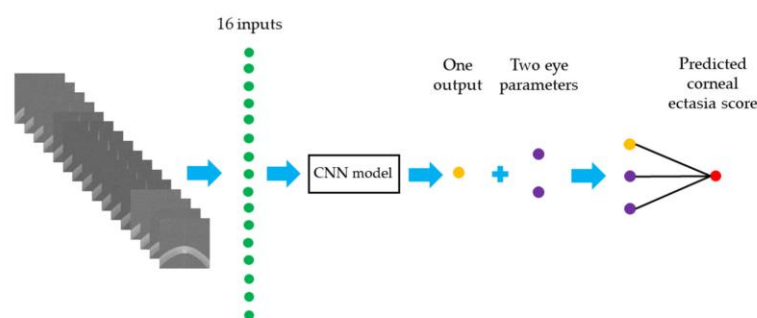


Figure 3. A workflow diagram for predicting the corneal ectasia score. Abbreviation: CNN = Convolutional Neural Network.

2.3. Evaluation Metrics

The Receiver Operating Characteristic (ROC) curve was examined to determine the ideal balance between sensitivity and specificity for the predictions by identifying the optimal threshold, which is the point that maximises the difference between sensitivity and (1 - specificity). Corneal ectasia scores below the threshold were classified as NE, indicating no detectable ectasia pattern, while scores at or above the threshold were categorised as E, indicating either suspected ectasia or clinical ectasia. Based on the True Positive (TP), False Positive (FP), True Negative (TN) and False Negative (FN) values for both categories, commonly used performance metrics were applied to assess the classification effectiveness of the modified EfficientNet-B0 architecture. These metrics, including accuracy, sensitivity, specificity, the Positive Predictive Value (PPV) and the F1 score, were computed following the definitions provided in [14]. Performance metric values and the area under the curve were rounded to four decimal places. The Youden index was rounded to two decimal places.

The Mean Absolute Error (MAE) was also used as a performance metric to assess how much, on average, the predicted corneal ectasia score values deviate from the actual

ESI values. The MAE is defined as the average absolute difference between predicted and actual values, as described in [15]. The MAE value was rounded to two decimal places.

2.4. Gradient-Weighted Class Activation Mapping

Gradient-Weighted Class Activation Mapping (Grad-CAM) [16] was used to visualise the areas within the CNN architecture that most strongly influenced the prediction of the corneal ectasia score in the test dataset. A Python script was developed to run the model and generate Grad-CAM outputs for the test data. For the CNN architecture, Grad-CAM was applied to the final convolutional layer.

2.5. The Implementation of the Graphical User Interface

The GUI was created using Tkinter (version 8.6), a Python library for constructing GUIs. For image processing tasks, such as reading, cropping and resizing, OpenCV (cv2) (version 4.12.0) was used. The modified EfficientNet-B0 architecture was implemented by using PyTorch (version 2.7.1). The trained architecture was saved for subsequent use in the GUI. Matplotlib (version 3.10.3) was used for the visualisation and saving of images, and NumPy (version 2.2.6) was used for numerical operations on image data. Pathlib was employed for managing file paths. The GUI was developed on a system running Python (version 3.13.5). The predicted corneal ectasia score value was rounded to two decimal places.

3. Results

Figure 4 shows the progression of the training and validation MSE over the epochs for the modified EfficientNet-B0 architecture.

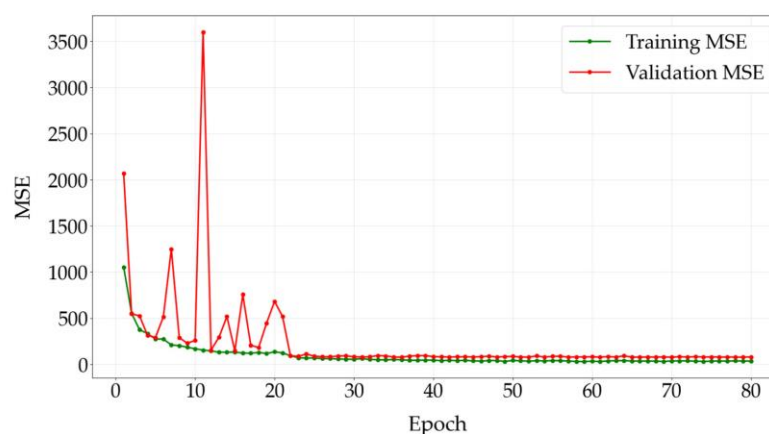


Figure 4. Training and validation Mean Squared Error across epochs. Abbreviation: MSE = Mean Squared Error.

Figure 5 shows the correlation between the actual ESIs and the corneal ectasia scores predicted by the modified EfficientNet-B0.

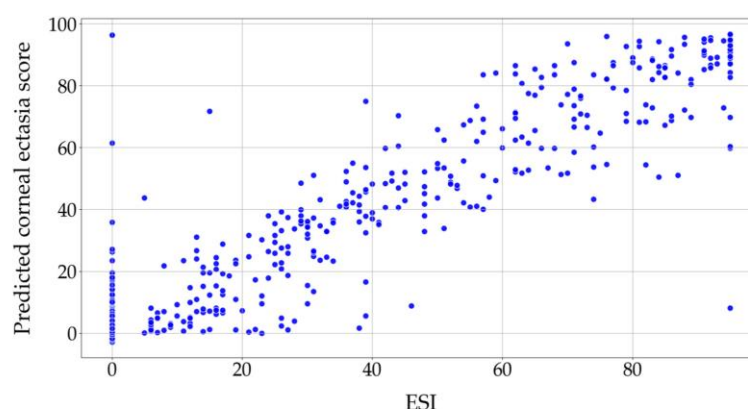


Figure 5. The correlation between the actual ESIs and the modified EfficientNet-B0 predictions. Abbreviation: ESI= Ectasia Screening Index.

Figure 6 shows the Kernel Density Estimate (KDE) of the errors between the actual ESIs and the corneal ectasia scores predicted by the modified EfficientNet-B0. This KDE plot represents the distribution of errors, where the error is determined by subtracting the actual ESI from the predicted corneal ectasia score.

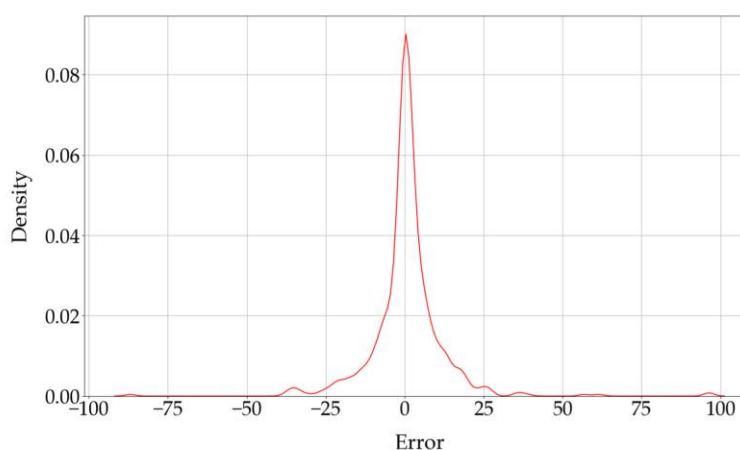


Figure 6. The KDE of the errors between the actual ESIs and the corneal ectasia scores predicted by the modified EfficientNet-B0. Abbreviation: KDE = Kernel Density Estimate.

The Bland–Altman plot illustrates the agreement between the ESI values and the predicted corneal ectasia scores. The mean difference was 0.7831, which shows a small positive bias in the predictions. The 95% confidence interval for the mean difference ranged from -0.1463 to 1.7125 . The standard deviation of the differences was 11.8353, which describes the variability between the predicted corneal ectasia scores and the ESI values. The lower and upper limits of agreement were -22.4140 and 23.9802 , respectively, with corresponding 95% confidence intervals of -45.6298 to 0.8017 for the lower limit and 0.7645 to 47.1960 for the upper limit. Figure 7 shows the Bland–Altman plot of ESI values versus predicted corneal ectasia scores for the test dataset.

<https://doi.org/10.3390/diagnostics16020310>

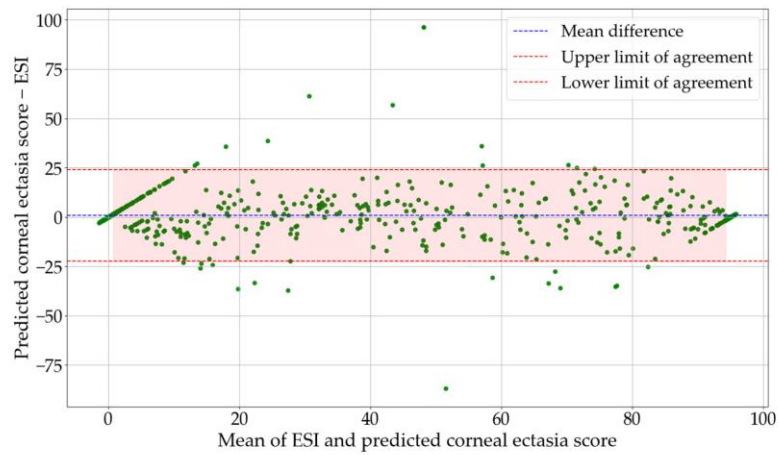


Figure 7. Bland—Altman plot of ESI values and predicted corneal ectasia scores for the test dataset. Abbreviation: ESI = Ectasia Screening Index.

Figure 8 shows the ROC curve for the architecture. The area under the curve is 0.9496, and the optimal threshold, determined using the Youden index, is 18.53. The optimal threshold was determined by computing the Youden index for each threshold in the ROC curve and selecting the threshold that maximised the index (Youden index = sensitivity – (1 – specificity)).

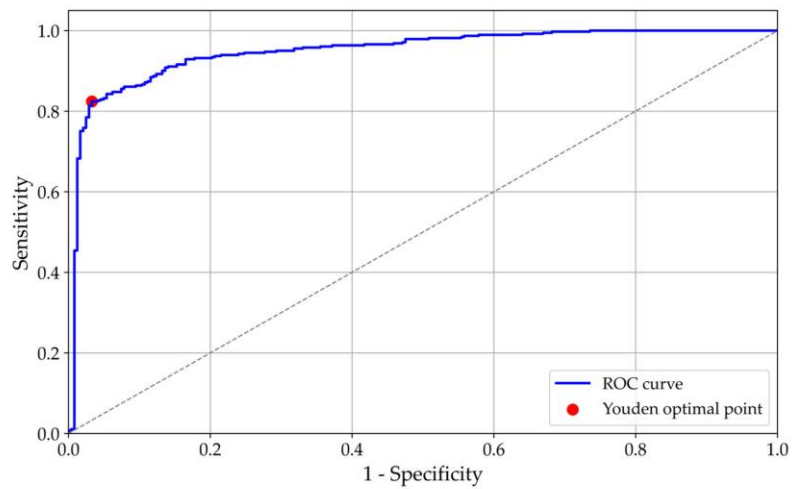


Figure 8. ROC curve. Abbreviation: ROC = Receiver Operating Characteristic.

Figure 9 shows the confusion matrix for the two-class classification.

<https://doi.org/10.3390/diagnostics16020310>

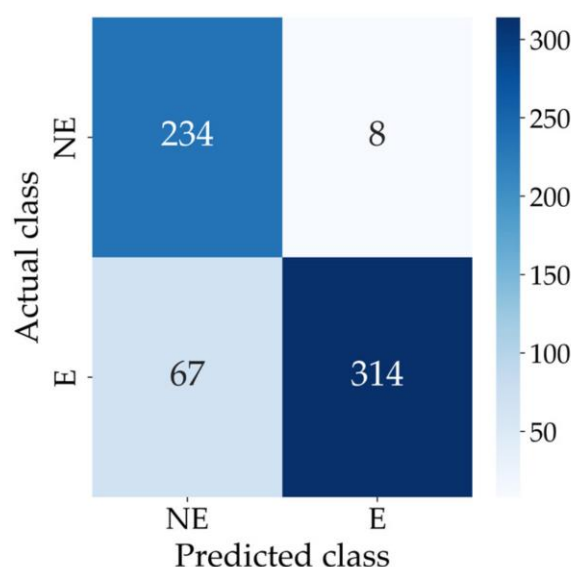


Figure 9. Confusion matrix for the two-class classification. Abbreviations: E = Ectasia and NE = No Ectasia.

For the two-class classification, the modified EfficientNet-B0 achieved an accuracy of 0.8796, a sensitivity of 0.8241, a specificity of 0.9669, a PPV of 0.9752 and an F1 score of 0.8933. Also, the architecture achieved an MAE of 6.65 when evaluated on the test dataset. Table 4 summarises the performance of the modified EfficientNet-B0 for the two-class classification on the test dataset.

Table 4. Performance metrics of the modified EfficientNet-B0 for the two-class classification, tested on the test dataset. Abbreviation: PPV = Positive Predictive Value.

Sensitivity	Specificity	PPV	F1 Score	Accuracy
0.8241	0.9669	0.9752	0.8933	0.8796

The optimal thresholds for classifying corneal ectasia were approximately 4.51 and 31.85, both rounded to two decimal places. These thresholds were obtained by performing a grid search of 500 steps across the range of predicted corneal ectasia scores. For each candidate pair of thresholds (t_1 , t_2) with $t_1 < t_2$, predictions were generated by assigning classes according to the thresholds, and the resulting weighted F1 score was calculated against the ground truth labels, which were derived from the ESI values. The thresholds that maximised the weighted F1 score were selected as optimal, ensuring the best balance between the PPV and sensitivity for the NE, SE and E classes.

Table 5 summarises the performance metrics of the modified EfficientNet-B0 for the three-class classification on the test dataset. The sensitivity, specificity, PPV, F1 score and overall accuracy are reported for each class (NE, SE and E), along with the macro- and weighted averages across all classes. The model achieved a weighted-average F1 score of 0.8495 and an overall accuracy of 0.8475. Figure 10 shows the confusion matrix for the three-class classification.

<https://doi.org/10.3390/diagnostics16020310>

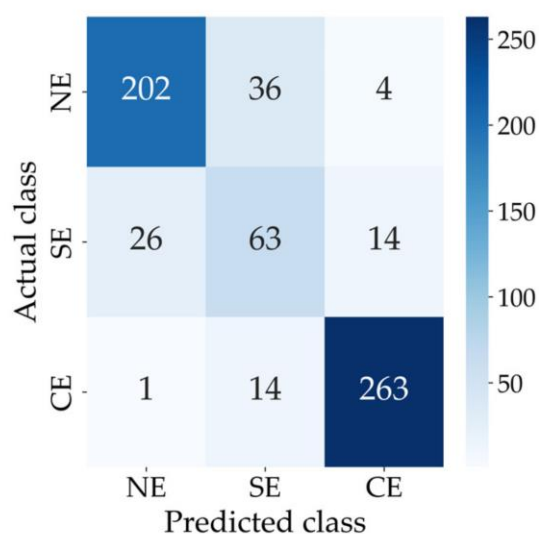


Figure 10. Confusion matrix for the three-class classification. Abbreviations: CE = Clinical Ectasia, NE = No Ectasia and SE = Suspected Ectasia.

Table 5. Performance metrics of the modified EfficientNet-B0 for the three-class classification, tested on the test dataset. Abbreviations: CE = Clinical Ectasia, NE = No Ectasia, PPV = Positive Predictive Value and SE = Suspected Ectasia.

Group	Sensitivity	Specificity	PPV	F1 Score	Overall Accuracy
NE	0.8347	0.9291	0.8821	0.8577	0.8475
SE	0.6117	0.9038	0.5575	0.5833	
CE	0.9460	0.9478	0.9359	0.9410	
Macro average	0.7975	0.9269	0.7919	0.7940	
Weighted average	0.8475	0.9333	0.8525	0.8495	

Figure 11 shows the Grad-CAM visualisations for two eye examinations produced by the modified EfficientNet-B0 architecture on the test dataset: (A) the predicted corneal ectasia score was 3.11 (rounded to two decimal places) for an ESI value of 0, and (B) the predicted corneal ectasia score was 95.04 (rounded to two decimal places) for an ESI value of 95. The relative importance of the CNN's decisions is shown with colour coding, which ranges from blue, to indicate little or no influence, to red, to indicate a strong influence on the prediction. The Grad-CAM corresponding to each prediction was overlaid onto the average of all sixteen resized and extracted images.

As shown in Figure S1, the GUI features a light background and three buttons, labelled 'File,' 'Images' and 'Prediction,' arranged horizontally in the centre of the screen.

When the user clicks the 'File' button, a window appears, allowing the selection of a 3dv file from the local system, as shown in Figure S2.

The application then checks the file to confirm it is the correct type (3dv) and has the required size of 36,600 KB. If the file is valid, a window appears displaying the message 'The selected file is valid'. If the file is not in 3dv format or does not meet the size requirement, the user receives an error message stating 'The selected file is not valid. The file must

<https://doi.org/10.3390/diagnostics16020310>

be a 3dv file and have a size of 36,600 KB'. Once a valid 3dv file is selected, the 'Images' button allows the user to view the extracted OCT images. When the button is clicked, the system processes the data from the selected file, reshapes it into 16 separate OCT images and arranges them in a 4×4 grid. The user can save the figure and zoom in on any of the 16 individual images within the grid.

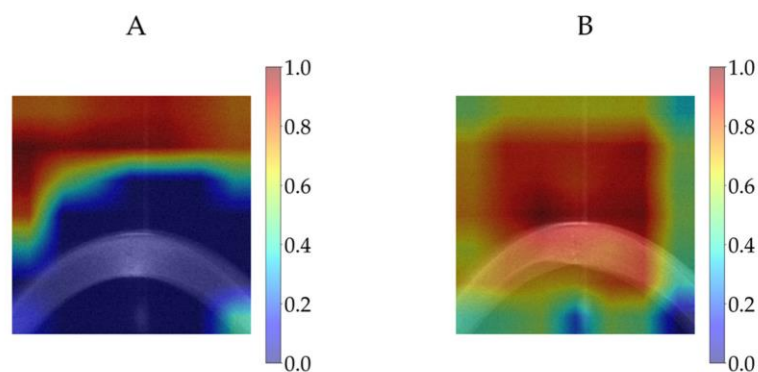


Figure 11. Grad-CAM visualisations for two eye examinations using the modified EfficientNet-B0 on the test dataset: (A) a predicted corneal ectasia score of 3.11 for an ESI value of 0 and (B) a predicted corneal ectasia score of 95.04 for an ESI value of 95 (both predicted corneal ectasia scores are rounded to two decimal places). Abbreviations: ESI = Ectasia Screening Index and Grad-CAM = Gradient-Weighted Class Activation Mapping.

Figure S3 shows the display of 16 OCT images from the selected file, 614711-19086-1.3dv, which belongs to the left eye. The user can click the 'Prediction' button to begin the corneal ectasia score prediction process.

Once this button is clicked, a window appears with the message 'Enter r for right eye or l for left eye,' as shown in Figure S4. The user is required to specify whether the selected 3dv file corresponds to the left or right eye by entering 'l' for the left eye or 'r' for the right eye. The eye side is a critical input, as it affects the accuracy of the analysis.

Once the input is provided, the application requests the user to select a directory in which to save the images extracted from the selected file. The user must choose a location to store the extracted images from the selected 3dv file. After saving the images, the application processes the OCT images by cropping and resizing them. These processed images are subsequently input into the modified EfficientNet-B0 architecture to predict the corneal ectasia score. The predicted corneal ectasia score is displayed to the user, along with a classification indicating whether the class is labelled as NE or SE or CE. If the class is NE, the application displays 'Diagnosis: No detectable ectasia pattern'. If the class is SE, it shows 'Diagnosis: Suspected ectasia'. If the class is CE, it displays 'Diagnosis: Clinical ectasia'. As shown in Figure S5, the predicted corneal ectasia score for the selected 3dv file is 54.42, which indicates ectasia, while the actual ESI is 51, which also suggests clinical ectasia based on the Casia2 threshold, where an ESI value of 30 to 95 indicates clinical ectasia.

4. Discussion

This method, which uses a user-friendly GUI, predicts corneal ectasia as a numerical score. On average, the predictions differ from the ESI values by 6.65, as measured by the MAE. With the numerical corneal ectasia prediction provided by the GUI, users can track and compare differences in corneal ectasia scores across multiple measurements, which allows them to observe trends in the condition's progression relative to the established

<https://doi.org/10.3390/diagnostics16020310>

threshold for a sensitive and dynamic assessment. The F1 score is particularly valuable when working with imbalanced datasets, where one class greatly outweighs the other. It serves as a more dependable metric for evaluating the architecture performance in such cases. Traditional measures like accuracy, sensitivity and specificity may not fully capture how effectively the architecture differentiates between classes. In contrast, the F1 score offers a more comprehensive assessment by factoring in both the sensitivity and PPV. Although the validation MSE fluctuated in the early epochs, its overall trend was downward, and it converged by epoch 80, which indicates that the architecture successfully learned the data without overfitting.

Ruiwei Feng et al. [17] developed KerNet, a deep learning model for detecting keratoconus and subclinical keratoconus based on a dataset that included 854 raw data samples from the Pentacam HR system. The model achieved a 94.74% accuracy, 93.71% sensitivity, 94.10% PPV and 93.89% F1 score. Jan Schatteburg et al. [18] developed a method for diagnosing keratoconus using Convolutional Neural Networks (CNNs) based on the ESI, with data collected using the SS-1000 Casia OCT Imaging System. However, the study lacked evaluation metrics. Benjamin Fassbind et al. [19] investigated keratoconus detection by using the CorNeXt CNN model, which builds on the ConvNeXt architecture [20], with topography maps generated from the Casia2 anterior OCT. The model achieved a 92.56% accuracy, 84.07% sensitivity, 100% specificity and a 91.34% F1 score for keratoconus detection. PeiPei Zhang et al. [21] applied the CorNet model to diagnose keratoconus by using raw data samples from the Corvis ST, a non-contact device that assesses corneal biomechanics through air-puff-induced deformation. The model achieved a 92.13% accuracy, 92.49% sensitivity, 91.54% specificity, a 94.77% PPV and a 93.62% F1 score. Hazem Abdelmotaal et al. [22] developed a DenseNet121-based CNN model to distinguish between normal eyes and those with keratoconus. The study utilised 734 video clips from the ST Corvis machines, each representing a different eye. Two datasets were employed. One comprised 502 subjects, including 259 normal eyes and 243 with keratoconus, and was randomly divided into 70% for training and validation and 30% for testing. The model achieved an accuracy of 89% on the test set of this dataset. Another dataset consisted of 232 subjects, including 131 normal eyes and 101 with keratoconus, which was used as the external validation set. The model reached an accuracy of 88% on this dataset. Wiyada Quanchareonsap et al. [23] tested three AI models based on EfficientNet-B7 to distinguish between normal corneas, subclinical keratoconus and keratoconus by using Pentacam tomographic maps and Corvis ST corneal biomechanics data. AI model 1, which used only Pentacam data, achieved an accuracy of 94.7%, a sensitivity of 90.8%, a specificity of 96.9% and a PPV of 92.4%. AI model 2 attained an accuracy of 95.6%, sensitivity of 93.0%, specificity of 94.3% and PPV of 92.9% by combining Corvis ST data with AI model 1. AI model 3 obtained an accuracy of 95.6%, sensitivity of 93.0%, specificity of 94.3% and PPV of 92.9% by incorporating the corneal biomechanical index into AI model 2. I. Kallel Fourati et al. [24] proposed a Matlab-based GUI for the monitoring and early detection of keratoconus. The study achieved accuracies of 96% and 92% for binary and three-class classifications, respectively. The binary classification separated normal corneas and keratoconus by using ten parameters from ORBSCAN images. The three-class system included normal eyes, suspected keratoconus and keratoconus, based on ORBSCAN clinical features. Additionally, combining ORBSCAN features with OCT-derived corneal pachymetry measures and clinical judgement improved the accuracy to 99% for two classes and 94% for three classes. The dataset comprised 98 patient records, each including ORBSCAN and OCT images. An artificial neural network with 10 input neurons, a hidden layer of 11 neurons and an output layer was used. Despite a high reported accuracy, metrics such as sensitivity, specificity, PPVs and F1 scores were not reported. The small size of

<https://doi.org/10.3390/diagnostics16020310>

the dataset affects the extent to which the results can be generalised. Alexandru Lavric et al. [25] applied 25 machine learning algorithms in Matlab to detect keratoconus using real-world data from 3151 corneal images of 3146 eyes, collected with SS-1000 CASIA OCT systems across several clinics in Japan. Each sample included 443 corneal parameters, and the ESI was used as the ground truth, classifying eyes as normal (ESI between 0 and 4), suspect or forme fruste keratoconus (ESI between 5 and 29) or keratoconus (ESI equal to or greater than 30). The dataset comprised 1970 normal eyes, 791 eyes with forme fruste keratoconus and 390 eyes with keratoconus. Two classification schemes were evaluated: a binary scheme separating normal from suspect or keratoconus eyes and a three-class scheme identifying normal eyes, suspect keratoconus and keratoconus eyes. The models achieved an accuracy range of 62% to 94%, with 3003 samples used for training and testing and 148 samples used for final validation.

Based on the results of this study, the GUI's optimal thresholds of 4.51 and 31.85, both rounded to two decimal places, correspond closely to the Casia2 thresholds of 5 and 30, respectively. This suggests that the GUI's predicted thresholds align closely with the Casia2 system in discriminating between no detectable ectasia pattern, suspected ectasia and clinical ectasia cases, while using raw OCT data that are independent of Casia2 software updates. This makes it more reliable for comparing corneal ectasia scores across different OCT-based devices, regardless of software updates or processing variations such as noise removal. The user has the option to view the 16 extracted images from the raw 3dv file and zoom in on each image. This feature allows the user to compare the diagnosis provided by the GUI with what they observe in the images.

However, this study has six limitations, which should be taken into consideration. First, of the 15,457 files, 9316 were excluded, which resulted in 6141 images being used for model development. Exclusions were primarily due to movement artefacts, post-Penetrating Keratoplasty (PK) cases and narrow lid openings. Although exact counts for each criterion were not recorded individually, these exclusions may have influenced the dataset's distribution by under-representing certain anatomical variations and post-surgical cases. Consequently, the model's performance may be less generalisable to images with movement artefacts, post-PK eyes or cases with incomplete eyelid exposure. Future work should include these under-represented cases to evaluate and potentially improve external validity. Second, only one CNN model was modified and tested, and it is possible that other more advanced models could yield more accurate or robust predictions. Third, the eye side is a critical input, as it affects the accuracy of the analysis, and further research could remove its significance in the analysis. Fourth, this study did not independently validate the Casia2-generated ESI scores against a gold standard. Consequently, potential discrepancies between the ESI and clinical diagnosis may exist. Fifth, the architecture was trained to mimic the ESI rather than a clinical ground truth. Consequently, the proposed score should be interpreted as a proxy for the ESI, and its direct clinical relevance requires validation against an expert clinical diagnosis in future studies. Sixth, the proposed score was evaluated only on Casia2 OCT data from a single institution, which limits the assessment of its generalisability across different devices or clinical settings. While the model reproduces the Casia2-generated ESI accurately within our dataset, its performance on data from other devices or institutions remains to be established. Future studies should evaluate the score on independent datasets to confirm its robustness and broader applicability. These limitations highlight areas for further investigation and improvement, which could enhance the overall accuracy and applicability of the GUI.

<https://doi.org/10.3390/diagnostics16020310>

5. Conclusions

The GUI uses raw 3dv files from the Casia2 device as input for predicting the corneal ectasia score and for classifying the condition of the cornea into three classes of no detectable ectasia pattern, suspected ectasia and clinical ectasia. Using raw data guarantees reliable diagnostics that remain unaffected by software modifications. This strategy has the advantage that, unlike using preprocessed data for predicting the condition of the cornea, it eliminates the influence of factors such as noise removal and filtering. By using raw data, one can be certain that such processes do not affect the prediction results. Therefore, if different devices use different software but follow the same method for capturing images (in this case, OCT), this approach provides a fair strategy for comparing prediction results across different models. Moreover, saving the extracted images through the GUI enables the user to compare their own assessment of the corneal condition (no detectable ectasia pattern, suspected ectasia and clinical ectasia) with the GUI's prediction. This gives the user another opportunity to independently determine the condition of the cornea and make a more reliable decision in case the GUI misclassifies it. This GUI also produces a numerical corneal ectasia score prediction, which enables the user to compare the degree of ectasia across multiple measurements.

Supplementary Materials: The following are available online at <https://www.mdpi.com/article/10.3390/diagnostics16020310/s1>, Figure S1: GUI for corneal ectasia score prediction. Abbreviation: GUI = Graphical User Interface; Figure S2: File selection window for choosing a 3dv file; Figure S3: Extracted and scaled images from the selected 3dv file; Figure S4: Eye selection window; Figure S5: Predicted corneal ectasia score and diagnosis.

Author Contributions: Conceptualization, M.M.; methodology, M.M.; software, M.M.; validation, A.L.; formal analysis, M.M.; investigation, M.M.; resources, A.L.; data curation, M.M.; writing—original draft preparation, M.M.; writing—review and editing, A.L.; visualisation, M.M.; supervision, A.L.; project administration, A.L.; funding acquisition, A.L. All authors have read and agreed to the published version of the manuscript.

Funding: M.M. was supported in part by the Rolf M. Schwiete Stiftung under project nr. 2020-024 (<https://schwiete-stiftung.com/>).

Institutional Review Board Statement: This study is a retrospective data analysis and has been exempted by the local institutional review board (Ärztammer des Saarlandes, registration number 157/21) on 31 May 2021.

Informed Consent Statement: All data processed in this study were already anonymised at the source before being transferred to us for processing. This precludes any back-tracing of the identity, and therefore informed consent of the patients was not necessary.

Data Availability Statement: The Python scripts and some data files are openly available in Zenodo at <https://doi.org/10.5281/zenodo.18067784>.

Conflicts of Interest: The authors declare no conflicts of interest. The funders had no role in the design of this study; in the collection, analyses, or interpretation of data; in the writing of the manuscript; or in the decision to publish the results.

Abbreviations

The following abbreviations are used in this manuscript:

AI	Artificial Intelligence
CNN	Convolutional Neural Network
CSV	Comma-Separated Value
FP	False Positive
FN	False Negative

<https://doi.org/10.3390/diagnostics16020310>

Grad-CAM	Gradient-Weighted Class Activation Mapping
GUI	Graphical User Interface
MAE	Mean Absolute Error
MSE	Mean Squared Error
OCT	Optical Coherence Tomography
PNG	Portable Network Graphic
PPV	Positive Predictive Value
RAM	Random-Access Memory
ROC	Receiver Operating Characteristic
TP	True Positive
TN	True Negative

References

- Pang, G.; Wang, C.; Wang, X.; Li, X.; Meng, Q. A review of human cornea finite element modeling: Geometry modeling, constitutive modeling, and outlooks. *Front. Bioeng. Biotechnol.* **2024**, *12*, 1455027. [\[CrossRef\]](#)
- Bastola, P.; Song, L.; Gilger, B.C.; Hirsch, M.L. Adeno-associated virus mediated gene therapy for corneal diseases. *Pharmaceutics* **2020**, *12*, 767. [\[CrossRef\]](#)
- Santodomingo-Rubido, J.; Carracedo, G.; Suzaki, A.; Villa-Collar, C.; Vincent, S.J.; Wolffsohn, J.S. Keratoconus: An updated review. *Contact Lens Anterior Eye* **2022**, *45*, 101559. [\[CrossRef\]](#)
- Rabinowitz, Y.S. Keratoconus. *Surv. Ophthalmol.* **1998**, *42*, 297–319. [\[CrossRef\]](#)
- Singh, R.B.; Koh, S.; Sharma, N.; Woreta, F.A.; Hafezi, F.; Dua, H.S.; Jhanji, V. Keratoconus. *Nat. Rev. Dis. Primers* **2024**, *10*, 81. [\[CrossRef\]](#)
- Jiao, H.; Hill, L.J.; Downie, L.E.; Chinnery, H.R. Anterior segment optical coherence tomography: Its application in clinical practice and experimental models of disease. *Clin. Exp. Optom.* **2019**, *102*, 208–217. [\[CrossRef\]](#) [\[PubMed\]](#)
- Fan, R.; Chan, T.C.; Prakash, G.; Jhanji, V. Applications of corneal topography and tomography: A review. *Clin. Exp. Ophthalmol.* **2018**, *46*, 133–146. [\[CrossRef\]](#) [\[PubMed\]](#)
- Gunvant, P.; Broadway, D.C.; Watkins, R.J. Repeatability and reproducibility of the BVI ultrasonic pachymeter. *Eye* **2003**, *17*, 825–828. [\[CrossRef\]](#) [\[PubMed\]](#)
- Gideon Abou Said, A.; Gispets, J.; Shneor, E. Strategies for early keratoconus diagnosis: A narrative review of evaluating affordable and effective detection techniques. *J. Clin. Med.* **2025**, *14*, 460. [\[CrossRef\]](#)
- Tan, M.; Le, Q. Efficientnet: Rethinking model scaling for convolutional neural networks. In *International Conference on Machine Learning*; PMLR: Cambridge, MA, USA, 2019; pp. 6105–6114.
- Dhruv, A.J.; Patel, R.; Doshi, N. Python: The most advanced programming language for computer science applications. *Sci. Technol. Publ.* **2021**, *Lda*, 292–299.
- Paszke, A.; Gross, S.; Massa, F.; Lerer, A.; Bradbury, J.; Chanan, G.; Killeen, T.; Lin, Z.; Gimelshein, N.; Antiga, L.; et al. Pytorch: An imperative style, high-performance deep learning library. *Adv. Neural Inf. Process. Syst.* **2019**, *32*, 5.
- Zhou, P.; Xie, X.; Lin, Z.; Yan, S. Towards understanding convergence and generalization of AdamW. *IEEE Trans. Pattern Anal. Mach. Intell.* **2024**, *46*, 6486–6493. [\[CrossRef\]](#)
- Hicks, S.A.; Strümke, I.; Thambawita, V.; Hammou, M.; Riegler, M.A.; Halvorsen, P.; Parasa, S. On evaluation metrics for medical applications of artificial intelligence. *Sci. Rep.* **2022**, *12*, 5979. [\[CrossRef\]](#)
- Qi, J.; Du, J.; Siniscalchi, S.M.; Ma, X.; Lee, C.H. On mean absolute error for deep neural network based vector-to-vector regression. *IEEE Signal Process. Lett.* **2020**, *27*, 1485–1489. [\[CrossRef\]](#)
- Selvaraju, R.R.; Cogswell, M.; Das, A.; Vedantam, R.; Parikh, D.; Batra, D. Grad-cam: Visual explanations from deep networks via gradient-based localization. In *Proceedings of the IEEE International Conference on Computer Vision, Venice, Italy, 22–29 October 2017*; pp. 618–626.
- Feng, R.; Xu, Z.; Zheng, X.; Hu, H.; Jin, X.; Chen, D.Z.; Yao, K.; Wu, J. KerNet: A novel deep learning approach for keratoconus and sub-clinical keratoconus detection based on raw data of the Pentacam HR system. *IEEE J. Biomed. Health Inform.* **2021**, *25*, 3898–3910. [\[CrossRef\]](#)
- Schatteburg, J.; Langenbucher, A. Protocol for the diagnosis of keratoconus using convolutional neural networks. *PLoS ONE* **2022**, *17*, e0264219. [\[CrossRef\]](#) [\[PubMed\]](#)
- Fassbind, B.; Langenbucher, A.; Streich, A. Automated cornea diagnosis using deep convolutional neural networks based on cornea topography maps. *Sci. Rep.* **2023**, *13*, 6566. [\[CrossRef\]](#)
- Liu, Z.; Mao, H.; Wu, C.Y.; Feichtenhofer, C.; Darrell, T.; Xie, S. A convnet for the 2020s. In *Proceedings of the IEEE/CVF Conference on Computer Vision and Pattern Recognition, New Orleans, LA, USA, 18–22 June 2022*; pp. 11976–11986.

<https://doi.org/10.3390/diagnostics16020310>

21. Zhang, P.; Yang, L.; Mao, Y.; Zhang, X.; Cheng, J.; Miao, Y.; Bao, F.; Chen, S.; Zheng, Q.; Wang, J. CorNet: Autonomous feature learning in raw Corvis ST data for keratoconus diagnosis via residual CNN approach. *Comput. Biol. Med.* **2024**, *172*, 108286. [[CrossRef](#)] [[PubMed](#)]
22. Abdelmotaal, H.; Hazarbassanov, R.M.; Salouti, R.; Nowroozzadeh, M.H.; Taneri, S.; Al-Timemy, A.H.; Lavric, A.; Yousefi, S. Keratoconus detection-based on dynamic corneal deformation videos using deep learning. *Ophthalmol. Sci.* **2024**, *4*, 100380. [[CrossRef](#)] [[PubMed](#)]
23. Quanchareonsap, W.; Kasetsuwan, N.; Reinprayoon, U.; Piyacomn, Y.; Wungcharoen, T.; Jermjutham, M. Deep Learning Algorithm for Keratoconus Detection from Tomographic Maps and Corneal Biomechanics: A Diagnostic Study. *J. Curr. Ophthalmol.* **2024**, *36*, 46–53. [[CrossRef](#)]
24. Kallel Fourati, I.; Kammoun, S. A matlab based graphical user interface for the monitoring and early detection of keratoconus. *J. Appl. Res. Technol.* **2024**, *22*, 22–31. [[CrossRef](#)]
25. Lavric, A.; Popa, V.; Takahashi, H.; Yousefi, S. Detecting keratoconus from corneal imaging data using machine learning. *IEEE Access* **2020**, *8*, 149113–149121. [[CrossRef](#)]

Disclaimer/Publisher’s Note: The statements, opinions and data contained in all publications are solely those of the individual author(s) and contributor(s) and not of MDPI and/or the editor(s). MDPI and/or the editor(s) disclaim responsibility for any injury to people or property resulting from any ideas, methods, instructions or products referred to in the content.

5. Discussion

In this study, raw OCT data from the cornea/anterior segment OCT Casia2 were used to mimic the ESI and to predict the corneal condition. The cornea/anterior segment OCT Casia2 generates raw data files in 3dv format, with each file containing data of sixteen equiangular meridional images. Three CNN architectures Densenet121, EfficientNet-B0, and ResNet18 were used to predict the ESI. DenseNets provide benefits, including a reduction in the number of parameters and the ease of the vanishing-gradient problem, and have been tested on CIFAR-10, CIFAR-100, ImageNet, and SVHN datasets [69]. EfficientNets employ a compound scaling approach, which achieves higher accuracy than single-dimension scaling approaches [70]. EfficientNets have been tested on ImageNet as well as transfer learning datasets, including Birdsnap, CIFAR-10, CIFAR-100, FGVC Aircraft, Flowers, Food-101, Oxford-IIIT Pets, and Stanford Cars [70]. ResNets feature residual networks, which make them easier to optimise, and have been tested on the CIFAR-10 and ImageNet datasets [72]. All the models were adapted to accept a sixteen-channel input instead of the three Red-Green-Blue channels. The outputs of the models were adapted to produce a single output. The adapted EfficientNet-B0 showed the lowest MAE, with a value of 5.86 on the test dataset. Additionally, the adapted EfficientNet-B0 achieved higher accuracy of 95.83% than the accuracy of 95.27% achieved by the adapted Densenet121 and the accuracy of 94.80% achieved by the adapted ResNet18 in predicting the ESIs on the test dataset. The accuracies achieved by all three CNN architectures are higher than the weighted average accuracy of 93.52% reported in [47], which used Casia2's preprocessed OCT data to identify corneal conditions, comprising healthy, keratoconus, keratoglobus, post laser, pellucid marginal corneal degeneration, not appreciable due to faults, invalidity, or lack of identifiability by the device, and other. Post laser eyes were considered abnormal because previous laser treatment must be identified before laser or cataract surgery, and because laser-induced corneal shape changes are often mistaken for other corneal pathologies. The dataset used in [47] comprised 2,182 scans in total, with 1,552 scans for training, 388 for validation, and 242 for testing. However, this comparison must be interpreted with caution, as the datasets across the studies are not the same. Moreover, all three CNN architectures achieved higher accuracies than the accuracy of 94.74% reported in [50], where raw data from the Pentacam HR system (Oculus GmbH, Wetzlar, Germany) were used for the detection of keratoconus and subclinical keratoconus. The dataset in [50] consisted of 854 samples. Furthermore, all three CNN architectures obtained higher accuracies than the accuracy of 92.13% reported in [55], which used raw data from the Corvis ST (Oculus, Wetzlar, Germany) for keratoconus diagnosis. The dataset used in [55] contained 1,786 raw data samples obtained from the Corvis ST. However, these comparisons must also be interpreted carefully, as different devices were used in the studies. The F1 scores achieved by all three CNN architectures are higher than the F1 scores reported in [47]. These results demonstrate that raw OCT data can provide superior diagnostic performance compared with preprocessed data-based methods for detecting ectatic corneal

diseases. Moreover, the F1 scores achieved by the adapted DenseNet121 and the adapted EfficientNet-B0 are higher than the F1 scores reported in [50,55].

Two points could be investigated in future research regarding the study reported in [74]. First, the dataset used for training, validation, and testing of the adapted ResNet18, the adapted DenseNet121, and the adapted EfficientNet-B0 contained 2,320 files for the *Keratoconus* class and 3,497 files for the *Not Keratoconus* class, with each file containing 16 equiangular meridional images. Future research could employ a balanced dataset, which may improve the accuracy of predictions for the *Keratoconus* class. Second, the images were preprocessed by removing 25% from the left and 25% from the right edges to eliminate eyelid regions, and 60% from the bottom to exclude areas outside the cornea. Future research could investigate the performance of CNN architectures on uncropped images.

The CNN models DenseNet121, EfficientNet-B0, MobileNetV3-Large, and ResNet18 were modified to classify corneal conditions into one of three groups: ‘normal’, indicating a normal eye; ‘ectasia’, indicating corneal ectasia; or ‘other disease’, including eyes with corneal dystrophies, penetrating keratoplasty, subepithelial or stromal scarring, Salzmann's nodules, or pterygium, using raw data from the Casia2 instrument. MobileNets are suitable for mobile and embedded vision applications and have been tested on the ImageNet dataset [71]. To accommodate the multi-channel input, the network architectures were revised by altering the first convolutional layer so that it accepted sixteen channels, replacing the typical three-channel Red–Green–Blue (RGB) input. The classification head was also modified, as rather than producing the 1000 outputs used in ImageNet models, it was redesigned to generate three outputs corresponding to the categories ‘normal’, ‘ectasia’, and ‘other disease’. All other parts of the CNN architectures remained unchanged. The modified MobileNetV3-Large achieved the highest overall accuracy, with a value of 0.9286, compared with the other three modified CNN models. Moreover, a GUI was provided for the classification of the corneal condition. Users can choose a raw data file in 3dv format and access the 16 automatically scaled images extracted from the file, with the option to magnify each image. This capability allows users to compare the diagnosis generated by the GUI with the observations they make in the images. In addition, the probability for each class is presented. The GUI assists ophthalmologists in diagnosing corneal conditions by providing a prediction based on the modified MobileNetV3-Large architecture from an eye examination conducted with the cornea/anterior segment OCT Casia2, without being affected by any revisions to the Casia2 software.

The macro-average F1 score obtained by the modified MobileNetV3-Large (0.9285) is higher than the weighted-average F1 score of 0.8817, derived from the value reported in [47]. Moreover, the F1 score achieved by the modified MobileNetV3-Large for the ‘Ectasia’ class (0.9412) is higher than the F1 score of 0.9134 for the *Keratoconus* class, derived from the value reported in [47]. While this comparison again suggests that using raw OCT data may offer improved performance over methods based on preprocessed data, it should be interpreted with caution, as the datasets in the referenced study differ from those used here.

One point could be explored in future research regarding the study reported in [76]. Mismatched assessments among the three experienced ophthalmologists were not considered, which may have influenced the generalisability of the results to the entire patient population. Future studies could consider including mismatched cases in order to improve the generalisability of the findings to the whole patient population.

Furthermore, EfficientNet-B0 was modified to mimic the ESI using a dataset that included 4,898 files for training, 620 files for validation, and 623 files for testing, with each file consisting of 16 equiangular meridional images. Two distinct categorisation methods were examined: a two-class model separating cases with no detectable ectasia from those with suspected or clinical ectasia grouped together, and a three-class model that independently classified no detectable ectasia, suspected ectasia, and clinical ectasia. When applied to the two-class classification task, the modified EfficientNet-B0 reached an accuracy of 0.8796. The model yielded an F1 score of 0.8933, a PPV of 0.9752, a sensitivity of 0.8241, and a specificity of 0.9669. When applied to the three-class classification, the architecture achieved an overall accuracy of 84.75%. and a weighted F1 score of 84.95%. The architecture reached an MAE of 6.65 on the test dataset.

A GUI was developed to predict the corneal ectasia score and to diagnose the corneal status in one of three categories: no detectable ectasia pattern, suspected ectasia, and clinical ectasia. Additionally, the GUI allows users to save the 16 extracted equiangular meridional images from the selected 3dv file, enabling them to compare their own assessment of the corneal status with the GUI's diagnosis. This provides an additional opportunity for independent assessment, which supports more reliable decision-making if the GUI produces an incorrect classification. The GUI generates a numerical score for corneal ectasia, which permits users to compare ectasia severity across different measurements.

Three points could be considered in future research regarding the study reported in [77]. First, future research could compare the diagnoses provided by the GUI with the same dataset labelled by a cornea specialist, who classifies the corneal condition into three categories: no detectable ectasia, suspected ectasia, and clinical ectasia. Second, specifying the eye side was essential, as the user must indicate whether the 3dv file is from a left- or right-eye examination. Future research could train the CNN architecture on the dataset without considering whether each file corresponds to a left- or right-eye examination, which would allow the GUI to function without requiring the user to specify the eye for each 3dv file. Third, for the three-class classification, the dataset contained differing numbers of eye examinations in each class: 2,549 files for 'No Ectasia', 1,127 files for 'Suspected Ectasia', and 2,465 files for 'Clinical Ectasia', with each file containing 16 equiangular meridional images. Future research could use a balanced dataset, which may improve the accuracy of predicted cases of 'Suspected Ectasia'. Using black box libraries such as Pandas, NumPy, and Matplotlib in Python can pose risks for programmers. For example, if programmers do not fully understand how these libraries operate internally, it becomes difficult to debug performance issues. Library updates may change functionality,

remove features, or introduce bugs. Relying heavily on these tools without awareness of their dependencies can also create compatibility issues in long-term projects.

Python scripts for Articles 1, 2, and 3 are provided in separate zipped files at <https://doi.org/10.5281/zenodo.18451700>.

5.1 Limitations of the study

This study has some limitations. For predicting the ESI, cases were excluded if they exhibited motion artefacts, narrow lid openings, and post-Penetrating Keratoplasty (PK) conditions. The exclusion was performed manually by visually inspecting the OCT images. This filtering may have influenced the extent to which these results can be generalised across all patient populations. Additionally, three CNN models were adapted and evaluated. Other CNN models may provide more accurate predictions. Furthermore, the eye side was used as a parameter for predicting the ESI. Future research could aim to remove its influence on the analysis.

For assessing corneal condition across three categories of normal, ectasia, and other diseases, four CNN models were adapted and evaluated. Other CNN models may attain superior performance. Moreover, of the 2,737 eye examinations labelled by three ophthalmologists, 1,325 were classified as ‘normal’ by all three ophthalmologists, representing around 73.49% of the 1,803 eye examinations that received the same labels from all three ophthalmologists. If further samples were available for the ‘ectasia’ and ‘other disease’ classes, the architecture could have been trained on a larger dataset from these classes, which could have led to higher accuracy.

The provided GUI for predicting the corneal ectasia score and diagnosing corneal condition into one of three classes of no detectable ectasia pattern, suspected ectasia, and clinical ectasia, lacked independent validation of the Casia2-derived ESI scores against a gold standard. Therefore, there may be potential inconsistencies between the ESI and the clinical diagnosis. Furthermore, cases primarily affected by movement artefacts, narrow lid openings, and post-PK were excluded from the dataset used to train, validate, and test the CNN architecture integrated into the GUI. As a result, the model may not generalise well to images with movement artefacts, narrow lid openings, and post-PK eyes. Future research should include these cases to assess and potentially enhance external validity. Moreover, for predicting the ESI, assessing corneal condition across three categories of normal, ectasia, and other diseases, and providing a GUI for predicting the corneal ectasia score, a monocentric dataset was used. This may affect generalisability when only data from a single institution are considered. Including data from multiple institutions and a greater variety of devices could improve generalisability.

5.2 Conclusions and outlook

According to the results, it can be concluded that raw OCT data can provide better performance than preprocessed data for predicting the ESI and the corneal condition. However, this should be interpreted cautiously, as comparisons with previous studies are not equivalent, given that the datasets differed

between studies. As advantages of using raw data instead of preprocessed data, it can be noted that preprocessed data can vary if the instrument's software changes, whereas raw data remain fixed. This affords a more reliable basis for analysis. Moreover, raw data are more natural, as no modifications such as noise removal are applied to them. As disadvantages of using raw data instead of preprocessed data, it can be noted that raw data may contain noise and be difficult to interpret. Moreover, each raw data file was 36.6 MB in size, whereas preprocessed data may be smaller.

Accurate determination of the corneal ectasia score is clinically important because it enables early diagnosis and treatment of keratoconus, which may slow disease development and maintain vision quality. The provided GUIs for classifying corneal conditions into one of three categories ('normal', 'ectasia', or 'other disease') and for predicting the corneal ectasia score can assist ophthalmologists in diagnosing the corneal condition. Ophthalmologists have the opportunity to compare their own assessment by examining the saved extracted equiangular meridional images from the selected 3dv file. Additionally, the GUI for predicting the corneal ectasia score outputs a numerical corneal ectasia score, which enables comparison of ectasia severity between eye examinations within the same class. Since both GUIs use raw data as input, their predictions are not affected by any changes to the software version of the cornea/anterior segment OCT Casia2.

Although DenseNet121, EfficientNet-B0, and ResNet18 were adapted for predicting the ESI, and DenseNet121, EfficientNet-B0, MobileNetV3-Large, and ResNet18 were modified for classifying corneal conditions into one of three categories ('normal', 'ectasia', or 'other disease'), other CNN models could also be considered for further research. Moreover, future research could evaluate the performance of CNN models by using datasets collected from multiple sources.

6. References

- [1] Willoughby CE, Ponzin D, Ferrari S, Lobo A, Landau K, Omidi Y (2010) Anatomy and physiology of the human eye: effects of mucopolysaccharidoses disease on structure and function—a review. *Clinical and Experimental Ophthalmology* 38: 2-11
- [2] Pang G, Wang C, Wang X, Li X, Meng Q (2024) A review of human cornea finite element modeling: geometry modeling, constitutive modeling, and outlooks. *Frontiers in Bioengineering and Biotechnology* 12: 1455027
- [3] Santodomingo-Rubido J, Carracedo G, Suzaki A, Villa-Collar C, Vincent S J, Wolffsohn JS (2022) Keratoconus: An updated review. *Contact Lens and Anterior Eye* 45: 101559
- [4] Espandar L, Meyer J (2010) Keratoconus: overview and update on treatment. *Middle East African journal of ophthalmology* 17: 15-20
- [5] Singh RB, Koh S, Sharma N, Woreta FA, Hafezi F, Dua HS, Jhanji V (2024) Keratoconus. *Nature Reviews Disease Primers* 10: 81
- [6] Rabinowitz YS (1998) Keratoconus. *Survey of ophthalmology* 42: 297-319
- [7] Martin R (2018) Cornea and anterior eye assessment with placido-disc keratometry, slit scanning evaluation topography and scheimpflug imaging tomography. *Indian journal of ophthalmology* 66: 360-366
- [8] Martin R (2018) Cornea and anterior eye assessment with slit lamp biomicroscopy, specular microscopy, confocal microscopy, and ultrasound biomicroscopy. *Indian journal of ophthalmology* 66: 195-201
- [9] Mohan S, Aggarwal A, Dada T, Vanathi M, Panda A (2007) Pachymetry: A review. *DOS times*, 12: 19-28
- [10] Seitz B, Behrens A, Langenbucher A (1997) Corneal topography. *Current opinion in ophthalmology* 8: 8-24
- [11] Fan R, Chan TC, Prakash G, Jhanji V (2018) Applications of corneal topography and tomography: a review. *Clinical and experimental ophthalmology* 46: 133-146
- [12] Schmitt JM (2002) Optical coherence tomography (OCT): a review. *IEEE Journal of selected topics in quantum electronics* 5: 1205-1215
- [13] Zhang X, Munir SZ, Sami Karim SA, Munir WM (2021) A review of imaging modalities for detecting early keratoconus. *Eye* 35: 173-187
- [14] Hamet P, Tremblay J (2017) Artificial intelligence in medicine. *metabolism* 69: S36-S40
- [15] Goodman D, Zhu AY (2024) Utility of artificial intelligence in the diagnosis and management of keratoconus: a systematic review. *Frontiers in Ophthalmology* 4: 1380701
- [16] Almodin E, Nassaralla BA, Sandes J (eds) (2022). *Keratoconus: a comprehensive guide to diagnosis and treatment*. Springer Cham

- [17] Karakitsos P, Stergiou EB, Pouliakis A, Tzivras M, Archimandritis A, Liossi AI, Kyrkou K (1996) Potential of the back propagation neural network in the discrimination of benign from malignant gastric cells. *Analytical and Quantitative Cytology and Histology* 18: 245-250
- [18] Karakitsos P, Cochand-Priollet B, Guillausseau PJ, Pouliakis A (1996) Potential of the back propagation neural network in the morphologic examination of thyroid lesions. *Analytical and Quantitative Cytology and Histology* 18: 494-500
- [19] Brickley MR, Cowpe JG, Shepherd JP (1996) Performance of a computer simulated neural network trained to categorise normal, premalignant and malignant oral smears. *Journal of oral pathology and medicine* 25: 424-428
- [20] Hurst RE, Bonner RB, Ashenayi K, Veltri RW, Hemstreet III GP (1997) Neural net - based identification of cells expressing the p300 tumor - related antigen using fluorescence image analysis. *Cytometry: The Journal of the International Society for Analytical Cytology*, 27: 36-42
- [21] Truong H, Morimoto R, Walts AE, Erler B, Marchevsky A (1995) Neural networks as an aid in the diagnosis of lymphocyte-rich effusions. *Analytical and quantitative cytology and histology* 17: 48-54
- [22] Ashizawa K, Ishida T, MacMahon H, Vyborny CJ, Katsuragawa S, Doi K (1999) Artificial neural networks in chest radiography: application to the differential diagnosis of interstitial lung disease. *Academic radiology* 6: 2-9
- [23] Matsuki Y, Nakamura K, Watanabe H, Aoki T, Nakata H, Katsuragawa S, Doi K (2002) Usefulness of an artificial neural network for differentiating benign from malignant pulmonary nodules on high-resolution CT: evaluation with receiver operating characteristic analysis. *American Journal of Roentgenology* 178: 657-663
- [24] Lucht R, Delorme S, Brix G (2002) Neural network-based segmentation of dynamic MR mammographic images. *Magnetic resonance imaging* 20: 147-154
- [25] Fisher RE, Scott JA, Palmer EL (1996) Neural networks in ventilation-perfusion imaging. *Radiology* 198: 699-706
- [26] Pereira S, Pinto A, Alves V, Silva CA (2016) Brain tumor segmentation using convolutional neural networks in MRI images. *IEEE transactions on medical imaging* 35: 1240-1251
- [27] Yang TF, Devine B, Macfarlane PW (1994) Artificial neural networks for the diagnosis of atrial fibrillation. *Medical and Biological Engineering and Computing* 32: 615-619
- [28] Dassen WR, Mulleneers RG, Smeets JL, Wellens HJ, Karthaus VL, Talmon JL (1995) Evaluation of new self - learning techniques for the generation of criteria for differentiation of wide - QRS tachycardia in supraventricular tachycardia and ventricular tachycardia. *Clinical cardiology* 18: 103-108
- [29] Walczak S, Nowack WJ (2001) An artificial neural network approach to diagnosing epilepsy using lateralized bursts of theta EEGs. *Journal of medical systems* 25: 9-20
- [30] Schaltenbrand N, Lengelle R, Toussaint M, Luthringer R, Carelli G, Jacqmin A, Lainey E, Muzet A, Macher JP (1996) Sleep stage scoring using the neural network model: comparison between visual and automatic analysis in normal subjects and patients. *Sleep* 19: 26-35

- [31] Abel EW, Zacharia PC, Forster A, Farrow TL (1996) Neural network analysis of the EMG interference pattern. *Medical engineering and physics* 18: 12-17
- [32] Smith JH, Graham J, Taylor RJ (1996) The application of an artificial neural network to Doppler ultrasound waveforms for the classification of arterial disease. *International journal of clinical monitoring and computing* 13: 85-91
- [33] Karako K, Chen Y, Tang W (2018) On medical application of neural networks trained with various types of data. *Bioscience trends* 12: 553-559
- [34] Tailor A, Jurkovic D, Bourne TH, Collins WP, Campbell S (1999) Sonographic prediction of malignancy in adnexal masses using an artificial neural network. *BJOG: An International Journal of Obstetrics and Gynaecology* 106: 21-30
- [35] Krizhevsky A, Sutskever I, Hinton GE (2012) Imagenet classification with deep convolutional neural networks. *Advances in neural information processing systems* 25
- [36] Bejnordi BE, Veta M, Van Diest PJ, Van Ginneken B, Karssemeijer N, Litjens G, Van Der Laak JA, Hermsen M, Manson QF, Balkenhol M, Geessink O (2017) Diagnostic assessment of deep learning algorithms for detection of lymph node metastases in women with breast cancer. *Jama* 318: 2199-2210
- [37] Salehinejad H, Valaee S, Dowdell T, Colak E, Barfett J (2018) Generalization of deep neural networks for chest pathology classification in x-rays using generative adversarial networks. In: 2018 IEEE international conference on acoustics, speech and signal processing (ICASSP), pp 990-994
- [38] Dong Y, Pan Y, Zhang J, Xu W (2017) Learning to read chest X-ray images from 16000+ examples using CNN. In: 2017 IEEE/ACM international conference on connected health: applications, systems and engineering technologies (CHASE), pp 51-57
- [39] Ali RB, Ejbali R, Zaied M (2016) Detection and classification of dental caries in x-ray images using deep neural networks. In: International conference on software engineering advances (ICSEA), pp 236
- [40] Defigueiredo RJ, Shankle WR, Maccato A, Dick MB, Mundkur P, Mena I, Cotman CW (1995) Neural-network-based classification of cognitively normal, demented, Alzheimer disease and vascular dementia from single photon emission with computed tomography image data from brain. *Proceedings of the National Academy of Sciences* 92: 5530-5534
- [41] Iftikhar P, Kuijpers MV, Khayyat A, Iftikhar A, De Sa MD (2020) Artificial intelligence: a new paradigm in obstetrics and gynecology research and clinical practice. *Cureus* 12
- [42] Manna C, Nanni L, Lumini A, Pappalardo S (2013) Artificial intelligence techniques for embryo and oocyte classification. *Reproductive biomedicine online* 26: 42-49
- [43] Guh RS, Wu TCJ, Weng SP (2011) Integrating genetic algorithm and decision tree learning for assistance in predicting in vitro fertilization outcomes. *Expert Systems with Applications* 38: 4437-4449
- [44] Keskinbora K, Güven F (2020) Artificial intelligence and ophthalmology. *Turkish journal of ophthalmology* 50: 37
- [45] Anton N, Doroftei B, Curteanu S, Catalin L, Ilie OD, Tărcoveanu F, Bogdănici CM (2022) Comprehensive review on the use of artificial intelligence in ophthalmology and future research

directions. *Diagnostics* 13: 100

- [46] Al-Timemy AH, Mosa ZM, Alyasseri Z, Lavric A, Lui MM, Hazarbassanov RM, Yousefi S (2021) A hybrid deep learning construct for detecting keratoconus from corneal maps. *Translational vision science and technology* 10: 16-16
- [47] Fassbind B, Langenbacher A, Streich A (2023) Automated cornea diagnosis using deep convolutional neural networks based on cornea topography maps. *Scientific Reports* 13: 6566
- [48] Abdelmotaal H, Hazarbassanov RM, Salouti R, Nowroozzadeh MH, Taneri S, Al-Timemy AH, Lavric A, Yousefi S (2024) Keratoconus detection-based on dynamic corneal deformation videos using deep learning. *Ophthalmology Science* 4: 100380
- [49] Elsayy A, Abdel-Mottaleb M, Abou Shousha M (2020) Diagnosis of corneal pathologies using deep learning. *Ophthalmic Technologies XXX SPIE* 11218: 150-160
- [50] Feng R, Xu Z, Zheng X, Hu H, Jin X, Chen DZ, Yao K, Wu J (2021) KerNet: a novel deep learning approach for keratoconus and sub-clinical keratoconus detection based on raw data of the Pentacam HR system. *IEEE Journal of Biomedical and Health Informatics* 25: 3898-3910
- [51] Hallett N, Yi K, Dick J, Hodge C, Sutton G, Wang YG, You J (2020) Deep learning based unsupervised and semi-supervised classification for keratoconus. In: 2020 international joint conference on neural networks (IJCNN), pp 1-7
- [52] Quanchareonsap W, Kasetsuwan N, Reinprayoon U, Piyacomn Y, Wungcharoen T, Jermjutitham M (2024) Deep Learning Algorithm for Keratoconus Detection from Tomographic Maps and Corneal Biomechanics: A Diagnostic Study. *Journal of Current Ophthalmology* 36: 46-53
- [53] Lucena AR, Araújo MOD, Carneiro RFL, Cavalcante TDS, Ribeiro ABN, Anselmo FJM (2021) Development of an application for providing corneal topography reports based on artificial intelligence. *Arquivos Brasileiros de Oftalmologia* 85: 351-358
- [54] Zaki WMDW, Daud MM, Saad AH, Hussain A, Mutalib HA (2021) A mobile solution for lateral segment photographed images based deep keratoconus screening method. *International Journal of Integrated Engineering* 13: 18-27
- [55] Zhang P, Yang L, Mao Y, Zhang X, Cheng J, Miao Y, Bao F, Chen S, Zheng Q, Wang J (2024) CorNet: Autonomous feature learning in raw Corvis ST data for keratoconus diagnosis via residual CNN approach. *Computers in Biology and Medicine* 172: 108286
- [56] Hara N, Benedikt K, Owaki H (2024) CASIA2: Anterior Segment 3D Swept-Source OCT. In: Aramberri J, Hoffer KJ, Olsen T, Savini G, Shammas HJ (eds) *Intraocular Lens Calculations. Essentials in Ophthalmology*. Springer, Cham, pp 417-429
- [57] Dhruv AJ, Patel R, Doshi N (2021) Python: the most advanced programming language for computer science applications. *Science and Technology Publications, Lda*: 292-299
- [58] Paszke A, Gross S, Massa F, Lerer A, Bradbury J, Chanan G, Killeen T, Lin Z, Gimelshein N, Antiga L, Desmaison A (2019) Pytorch: An imperative style, high-performance deep learning library. *Advances in neural information processing systems* 32

- [59] Taye MM (2023) Theoretical understanding of convolutional neural network: Concepts, architectures, applications, future directions. *Computation* 11: 52
- [60] Grossi E, Buscema M (2007) Introduction to artificial neural networks. *European journal of gastroenterology and hepatology* 19: 1046-1054
- [61] Krichen M (2023) Convolutional neural networks: A survey. *Computers* 12: 151
- [62] Li Z, Liu F, Yang W, Peng S, Zhou J (2021) A survey of convolutional neural networks: analysis, applications, and prospects. *IEEE transactions on neural networks and learning systems* 33: 6999-7019
- [63] Wang M, Lu S, Zhu D, Lin J, Wang Z (2018) A high-speed and low-complexity architecture for softmax function in deep learning. In: 2018 IEEE asia pacific conference on circuits and systems (APCCAS), pp 223-226
- [64] Qi J, Du J, Siniscalchi SM, Ma X, Lee CH (2020) On mean absolute error for deep neural network based vector-to-vector regression. *IEEE Signal Processing Letters* 27: 1485-1489
- [65] Li L, Doroslovački M, Loew MH (2020) Approximating the gradient of cross-entropy loss function. *IEEE access* 8: 111626-111635
- [66] Srivastava N, Hinton G, Krizhevsky A, Sutskever I, Salakhutdinov R (2014) Dropout: a simple way to prevent neural networks from overfitting. *The journal of machine learning research* 15: 1929-1958
- [67] Ying X (2019) An overview of overfitting and its solutions. In: *Journal of physics: Conference series* 1168, pp 022022
- [68] Duchi J, Hazan E, Singer Y (2011) Adaptive subgradient methods for online learning and stochastic optimization. *Journal of machine learning research* 12
- [69] Huang G, Liu Z, Van Der Maaten L, Weinberger KQ (2017) Densely connected convolutional networks. In: *Proceedings of the IEEE conference on computer vision and pattern recognition*, pp 4700-4708
- [70] Tan M, Le Q (2019) Efficientnet: Rethinking model scaling for convolutional neural networks. In: *International conference on machine learning*, pp 6105-6114
- [71] Howard AG, Zhu M, Chen B, Kalenichenko D, Wang W, Weyand T, Andreetto M, Adam H (2017) Mobilenets: Efficient convolutional neural networks for mobile vision applications. *arXiv preprint arXiv:1704.04861*
- [72] He K, Zhang X, Ren S, Sun J (2016) Deep residual learning for image recognition. In: *Proceedings of the IEEE conference on computer vision and pattern recognition*, pp 770-778
- [73] Hicks SA, Strümke I, Thambawita V, Hammou M, Riegler MA, Halvorsen P, Parasa S (2022) On evaluation metrics for medical applications of artificial intelligence. *Scientific reports* 12: 5979
- [74] Mirsalehi M, Fassbind B, Streich A, Langenbacher A (2025) Prediction of the ectasia screening index from raw Casia2 volume data for keratoconus identification by using convolutional neural networks. *PLoS One* 20: e0311036
- [75] Mirsalehi M, Fassbind B, Streich A, Langenbacher A (2025) Correction: Prediction of the ectasia screening index from raw Casia2 volume data for keratoconus identification by using convolutional

neural networks. PLoS One 20: e0338609

[76] Mirsalehi M, Schwemm M, Flockerzi E, Szentmáry N, Abdin AD, Seitz B, Langenbacher A (2025) Deep Learning-Based Diagnosis of Corneal Condition by Using Raw Optical Coherence Tomography Data. *Diagnostics* 15: 3115

[77] Mirsalehi M, Langenbacher A (2026) A Deep Learning-Based Graphical User Interface for Predicting Corneal Ectasia Scores from Raw Optical Coherence Tomography Data. *Diagnostics* 16: 310

7. Publications

- [1] Kremers J, Aher AJ, Popov Y, Mirsalehi M, Huchzermeyer C (2021) The influence of temporal frequency and stimulus size on the relative contribution of luminance and L-/M-cone opponent mechanisms in heterochromatic flicker ERGs. *Documenta Ophthalmologica* 143: 207-220
- [2] Mirsalehi M, Fassbind B, Streich A, Langenbacher A (2025) Prediction of the ectasia screening index from raw Casia2 volume data for keratoconus identification by using convolutional neural networks. *PLoS One* 20: e0311036
- [3] Mirsalehi M, Schwemm M, Flockerzi E, Szentmáry N, Abdin AD, Seitz B, Langenbacher A (2025) Deep Learning-Based Diagnosis of Corneal Condition by Using Raw Optical Coherence Tomography Data. *Diagnostics* 15: 3115
- [4] Mirsalehi M, Langenbacher A (2026) A Deep Learning-Based Graphical User Interface for Predicting Corneal Ectasia Scores from Raw Optical Coherence Tomography Data. *Diagnostics* 16: 310

8. Abbreviations

CNN	Convolutional Neural Network
ESI	Ectasia Screening Index
False Negative	FN
False Positive	FP
Graphical User Interface	GUI
Mean Squared Error	MSE
Mean Absolute Error	MAE
OCT	Optical Coherence Tomography
Penetrating Keratoplasty	PK
Positive Predictive Value	PPV
Receiver Operating Characteristic	ROC
Red–Green–Blue	RGB
SS-OCT	Swept-Source Optical Coherence Tomography
True Negative	TN
True Positive	TP

9. Acknowledgment

I express my gratitude to Prof. Dr. Dr. Achim Langenbacher for his guidance throughout this study, and to PD Dr. Alaa Din Abdin, PD Dr. Elias Flockerzi, and Univ.-Prof. Dr. Nora Szentmary for labelling the data.

10. Curriculum Vitae

The curriculum vitae was removed from the electronic version of the doctoral thesis for reasons of data protection.